Modeling of resonant optical nanostructures with semi-analytical methods based on the object eigenmodes

Anton Ovcharenko

université PARIS-SACLAY

INSTITUT d'OPTIQUE GRADUATE SCHOOL ParisTech

NNT : 2019SACL0019

Modelling of resonant optical nanostructures with semi-analytical methods based on the object eigenmodes

Thèse de doctorat de l'Université Paris-Saclay
préparée à l'Institut d'Optique Graduate School

École doctorale n°572 Ondes et Matières (EDOM)
Spécialité de doctorat: Physique

Thèse présentée et soutenue à Palaiseau, le 20 Décembre 2019, par

Anton Ovcharenko

Composition du Jury :

Riad Haïdar Directeur de Recherche, ONERA	Président
Xavier Letartre Directeur de Recherche CNRS, Institut des Nanotechnologies de Lyon	Rapporteur
Antoine Moreau Maître de Conférences, Université Clermont Auvergne	Rapporteur
Anne-Laure Fehrembach Maître de Conférences, Université d'Aix-Marseille	Examinatrice
Olivier Gauthier-Lafaye Directeur de Recherche CNRS, Laboratoire d'Analyse et d'Architecture des Systèmes	Examinateur
Christophe Sauvan Chargé de Recherche CNRS, Institut d'Optique Graduate School	Directeur de thèse

Thèse de doctorat

Résumé

Cette thèse est consacrée au développement de modèles semi-analytiques précis pour le calcul numérique de dispositifs nanophotoniques résonants. Il s'agit en particulier de membranes à cristaux photoniques, qui supportent des résonances avec des très grands facteurs de qualité, et d'ensembles composés de plusieurs nano-antennes plasmoniques, qui présentent des résonances avec des faibles facteurs de qualité. La thèse est divisée en deux parties.

La première partie présente un modèle semi-analytique pour le calcul des modes supportés par des membranes à cristaux photoniques. Les modes à fuite (leaky modes) supportés par ces membranes structurées sont modélisés comme une résonance Fabry-Perot transverse composée de quelques ondes de Bloch propagatives qui vont et viennent verticalement à l'intérieur de la structure. Ce modèle est appliqué à l'étude des états liés dans le continuum (bound states in the continuum, ou BIC). Nous montrons que le modèle Fabry-Perot multimode est parfaitement adapté pour prédire l'existence des BICs ainsi que leur position dans l'espace des paramètres. Grâce à la semi-analyticité du modèle, nous étudions la dynamique des BICs avec l'épaisseur de la membrane pour des structures symétriques et asymétriques. Dans ce dernier cas, nous étudions des objets présentant soit une symétrie horizontale brisée, soit une symétrie verticale brisée (ajout d'un substrat). Le modèle Fabry-Perot nous permet d'obtenir des informations importantes sur la nature et le comportement des BICs. Nous démontrons que lorsque la symétrie miroir horizontale est brisée, les BICs dus à la symétrie du système, qui existent dans les structures symétriques au point Gamma du diagramme de dispersion, restent des BICs malgré l'absence de symétrie mais changent de nature. Ils deviennent des BICs dus à des interférences destructives entre les ondes de Bloch.

La deuxième partie est consacrée au développement d'une théorie modale originale pour modéliser la diffusion de la lumière par des structures complexes composées d'un ensemble de plusieurs nano-antennes. L'objectif est de pouvoir modéliser la diffusion de la lumière par des métasurfaces à partir de la seule connaissance des modes de leurs constituants individuels. Pour ce faire, nous combinons un formalisme modal basé sur l'utilisation des modes quasi-normaux (QNM) avec la théorie multipolaire de la diffusion multiple basée sur le calcul de la matrice de transition (matrice T) d'un diffuseur unique. La matrice T fournit la relation entre le champ incident et le champ diffusé dans la base des harmoniques sphériques vectorielles. Elle contient toutes les propriétés de diffusion intrinsèques à l'objet. Le calcul de cette matrice représente une charge numérique lourde car elle nécessite de nombreux calculs rigoureux du champ

diffusé. L'utilisation d'une décomposition modale avec des QNMs nous permet d'une part de rendre une partie du calcul analytique et d'autre part d'apporter une meilleure compréhension physique. Nous dérivons une décomposition modale de la matrice T et testons sa précision sur le cas de référence d'une nanosphère métallique.

Enfin, la décomposition modale de la matrice T est appliquée à des cas pratiques d'intérêt en nanophotonique. A partir de la seule connaissance de quelques modes d'un nanocylindre plasmonique unique, nous calculons analytiquement la diffusion multiple de la lumière par un dimère et par une antenne Yagi-Uda composés de ces nanocylindres. La comparaison avec les résultats d'une méthode numérique rigoureuse démontre un bon accord avec le calcul modal. Par rapport à des calculs entièrement rigoureux, la décomposition modale de la matrice T permet une réduction significative du temps de calcul. Comme les calculs sont analytiques une fois que les modes ont été calculés, l'approche modale est extrêmement utile pour les problèmes d'optimisation.

Thesis summary

The presented thesis is dedicated to the development of semi-analytical accurate models for the numerical calculation of resonant nanophotonic devices. In particular, it concerns photonic crystal slabs, which can support resonances with high quality factors, and ensembles composed of several plasmonic nanoantennas, which exhibit resonances with low quality factors. The structure of the thesis is two-fold.

In the first part, a semi-analytical model for the calculation of the modes supported by photonic crystal slabs (their dispersion and quality factors) is presented. Leaky modes supported by photonic crystal slabs are modeled as a transverse Fabry-Perot resonance composed of a few propagative Bloch waves bouncing back and forth vertically inside the slab. This model is applied to the study of bound states in the continuum (BICs). We show that the multimode Fabry-Perot model is perfectly suitable to predict the existence of BICs as well as their precise positions in the parameter space. We show that, regardless of the slab thickness, BICs cannot exist below a cut-off frequency, which is related to the existence of the second-order Bloch wave in the photonic crystal. Thanks to the semi-analyticity of the model, we investigate the dynamics of BICs with the slab thickness in symmetric and asymmetric photonic crystal slab. In the latter case, we investigate structures with either a broken horizontal symmetry or a broken vertical symmetry (addition of a substrate). As a result, we obtain some important insights into the nature and behavior of BICs. We evidence that, as the horizontal mirror symmetry is broken, the symmetry-protected BICs that exist in symmetric structures at the Gamma-point of the dispersion diagram are still BICs despite the absence of symmetry but change their nature. They become resonance-trapped BICs, but only for specific values of the slab thickness.

The second part of the thesis is dedicated to the development of an original modal theory to model light scattering by complex structures composed of a small ensemble of plasmonic nanoantennas. The objective is to be able to model light scattering by metasurfaces from the sole knowledge of the eigenmodes of their individual constituents. For that purpose, we combine a quasi-normal mode (QNM) formalism with the multipole multiple-scattering theory based on the calculation of the so-called transition matrix (T-matrix) of a single scatterer. The T-matrix provides the relation between the incident and scattered fields in the vectorial spherical harmonics basis. It captures all the intrinsic scattering properties of the object that are due to its shape and refractive index distribution. Computation of the T-matrix is a heavy numerical burden since it requires numerous rigorous calculations of the scattered field – one for each harmonic in the basis. Using a modal expansion of the scattered

field with QNMs allows us to bring both analyticity and physical understanding into the calculation. We derive a modal expansion of the T-matrix and test its accuracy on the reference case of a metallic nanosphere.

Finally, we apply the modal expansion of the T-matrix to practical cases of interest in nanophotonics. From the sole knowledge of a few modes of a single plasmonic nanorod, we calculate analytically multiple light scattering by a dimer and a Yagi-Uda antenna composed of these nanorods. We apply also the modal approach to a periodic two-dimensional array of nanorods. Comparison with the results of a rigorous Maxwell's equations solver demonstrates a good agreement with the QNM-based calculation. Compared to fully rigorous calculations, the QNM expansion of the T-matrix allows for a significant reduction of the computation time. Since the calculations are analytical once the modes have been calculated, the QNM approach is extremely useful for optimisation problems.

Contents

Chapter I

Introduction

Shaping and manipulation of electromagnetic waves is a widespread technique in modern life from radio and microwaves to visible light and X-rays. Glass optical lenses were among the first devices on this path. Now, we use electromagnetic waves in one form or another in virtually every aspect of life, science, and technology, in a way that was not possible before (not to count examples from nature, like eyesight and magnetic-field sensitivity in some birds). As it often happens with a successful piece of technology, we are approaching the limits that conventional optical devices, like common lenses, hit. At the same time, novel technological endeavours and aspirations demand radically new performance of optical elements. Among them are sub-diffraction limit imaging, smaller footprint, lower energy usage, and higher degree of beam manipulation and steering. The field of nanophotonics has emerged as a result with the aim to overcome the Abbe-Rayleigh diffraction limit, developing technology able to manipulate light on a deep-subwavelength scale [1]. As we peer down into the nanoworld, shrinking the photons to atomic sizes, new fundamental physics awaits with the potential of providing monumental technological leaps.

In order to stand up to these challenges we cannot get away with an incremental progress, gradually refining old techniques – totally new approaches are required. Since the advent of micro and nanotechnologies, there have been several new concepts introduced in the optics and optoelectronics communities. A non-exhaustive list includes the keywords photonic crystals, plasmonics, nanoantennas, metamaterials, and metasurfaces.

Historically, we can probably begin the countdown with photonic crystals – structures with a periodic variation of optical refractive index, which would act on photons in a similar way a periodic potential acts on electrons in a common solid-state crystal [2–8]. Even if surface and volume plasmons were known in solid-state physics [9], plasmonics started to become a research field in its own right with the work on extraordinary optical transmission [10]. The rise of metamaterials started with the experimental demonstration of a negative index of refraction and the theoretical proposal for an appealing application, a perfect lens [11–13]. Nowadays, these are

all well-known building blocks in the nanophotonics toolbox, which are used for an increasingly large number of applications.

In this introduction, we describe a few of these nanophotonic structures and their applications (Section I.1), as well as the numerical methods that can be used to design their optical properties (Sec. I.2). We focus on resonant devices (i.e., devices whose spectral response is characterised by a resonance) for applications in free-space optics. Even if it concerns a large and active community, we do not consider in this thesis nanophotonic structures working in a guided-wave configuration. The last section of this introduction (Sec. I.3) details the outline of the thesis.

1 Resonant optical nanostructures

Resonant nanostructures are key components of modern photonics. They are used for applications as varied as the realisation of nanosources (nanolasers, non-classical light sources), the exploitation of hot spots for the detection of chemical or biological species, the control of light extraction/absorption (LEDs, photovoltaic cells, photodetectors)... Such a list can only be non-exhaustive as resonant nanostructures occupy a central place in current nanophotonic applications.

If fundamental studies can be realised with single objects, applications often require the use of large-scale arrays, whether periodic, non-periodic, or fully disordered. The large family of resonant nanostructured arrays can be separated into two main categories: the ones with either resonant or non-resonant unit cells. In the latter case, the resonance results from collective effects between several unit cells; typical examples are the phenomena of guided-mode resonance in photonic crystal slabs and light localization in disordered media. In the former case, the resonance of an array can be directly related to the intrinsic resonance of its constituents. Metamaterials and metasurfaces usually belong to this second category.

In the following Sections, we briefly introduce the concepts of photonic crystal slabs, metamaterials, and metasurfaces, as well as their main applications.

1.1 Photonic crystal slabs

Photonic crystals are structures with a periodic variation of refractive index, which would act on photons in a similar way a periodic potential acts on electrons in a common solid-state crystal. First known important endeavours were undertaken by

Lord Rayleigh around 1887 when his nascent experiments with periodic multi-layer dielectric stacks demonstrated a possibility to achieve a photonic band gap in one dimension. A modern phase of these experiments were started almost exactly 100 years later in 1987 by the works of Eli Yablonovitch [3], who coined the term "photonic crystal", which is so widespread nowadays, and Sajeev John [4].

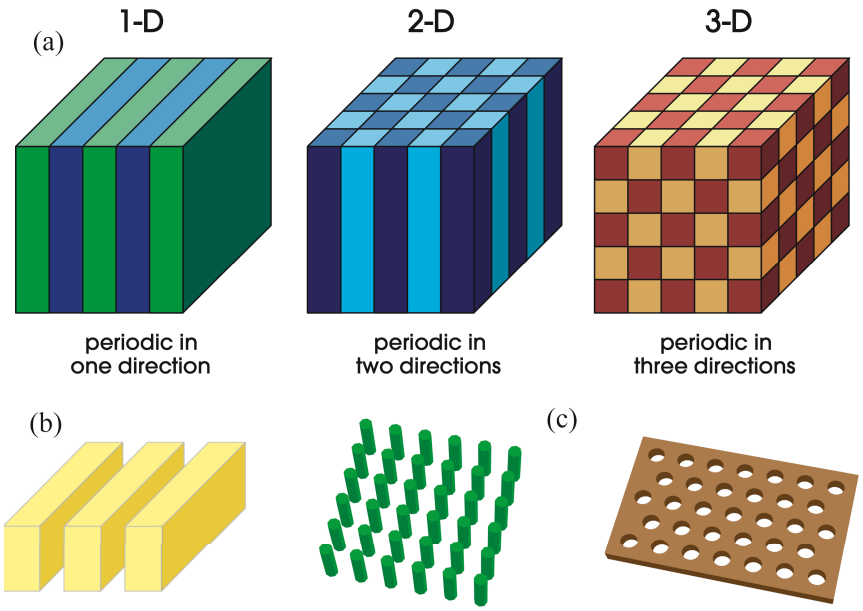

Figure I.1.: Schematic examples of (a) bulk photonic crystals (PhC) with one-, two-, and three-dimensional index modulation; (b) one-dimensional PhC slab; (c) two kinds of 2D PhC slabs – rod slab (square array of dielectric rods in air, left), hole slab (triangular array of air holes in a dielectric slab, right). Images (a) and (c) adapted from [2]

Usually, photonic crystals are made of a high-index dielectric material such as Si or III-V semiconductors with air slits or holes that introduce the periodic order. When their periodicity approaches the wavelength of light, new diffraction effects appear, most notably, a photonic band gap [7], in full analogy with the electronic band gap in a semiconductor. This way, light propagation can be restricted in the direction of periodicity, in one, two, or three dimensions. Then, by introducing defects or wave guiding homogeneous regions, light can be localized or directed in the desired direction [2]. Selecting the geometric parameters of a photonic crystal may not be easy, but if done right we would have a very broad control over light dispersion and therefore also over the propagation speed of a signal.

Photonic crystal slabs (PhC slabs) are formed by etching a one- or two-dimensional

(1D or 2D) photonic crystal in a dielectric layer of finite (usually subwavelength) thickness. Compared to three-dimensional (3D) photonic crystals, the simplified architecture of PhC slabs makes them attractive for on-chip integrated photonics [14, 15]. In addition, their peculiar diffraction properties have been used in a wide variety of applications, including filters [16–20], vertical-cavity surface-emitting lasers (VCSEL) [21–23], photovoltaics [24, 25], thermal emission [26], and structural colour generation [27].

The unit cell of a PhC slab is usually non-resonant on its own. The resonances that can be observed in their reflection and transmission result from the phenomenon of guided-mode resonance, i.e., the coupling of the incident light to a leaky mode supported by the periodic structure [17, 28–33].

1.2 Metamaterials

When the period is much smaller than the operating wavelength, a periodic medium can be accurately described as a homogeneous one with some effective index. This is the basis of so-called Effective Medium Theory (EMT) [34, 35]. By modifying the geometry, the effective index can in principle be engineered to be a specific value thus offering an optical response unavailable using conventional materials. Such structures became known as metamaterials [36–38]. Metamaterials, in broad terms, are artificially designed and fabricated composite materials engineered to have a specific set of predefined desired properties.

Metamaterials with a negative index of refraction are emblematic examples of such artificial structures [11, 12, 39, 40]. However, the concept of structuring a material at a subwavelength scale for modifying its macroscopic properties is more general and has given birth to a much wider range of optical functionalities. A non-exhaustive list includes form birefringence, as originally used by Hertz to polarise radio waves, anti-reflection coatings, diffractive optical elements with enhanced capabilities, and more recently magnetism at optical frequencies and cloaking.

Although this is not always the case, the constituent elements of metamaterials are often resonant on their own. Metamaterials can be ordered, as well as disordered, or possessing some far order [38, 43–46]. In the simplest case of ordered deep-subwavelength metamaterials, homogenisation techniques can be applied and the metamaterial can be treated as a homogeneous medium with effective permittivity and permeability values. In this regime, the design is greatly simplified since one can use well-known analytical results from the theory of homogeneous media. In

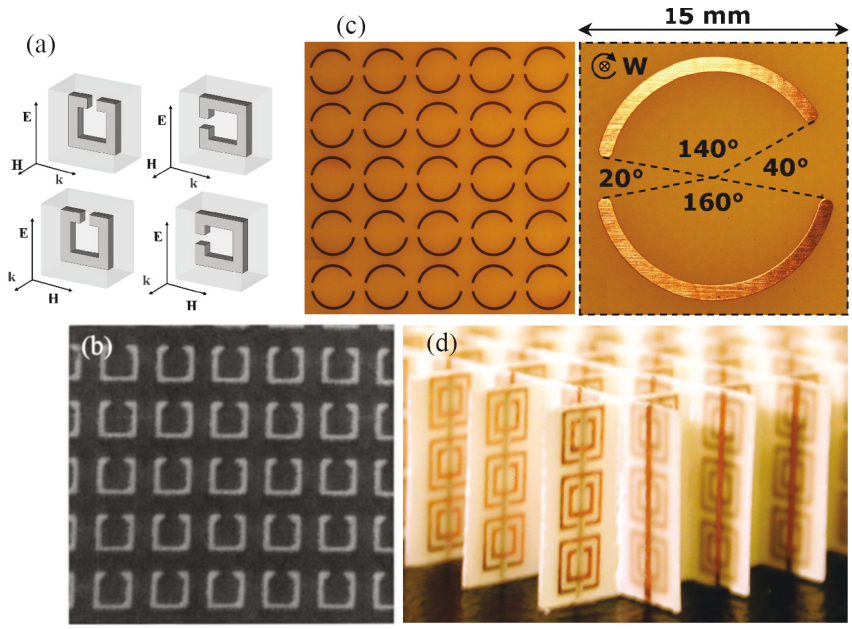

Figure I.2.: Typical examples of a split-ring (SSR) resonator for achieving negative effective index of refraction. (a) Schematic of single unit cells orientation with respect to incident wave polarisation and direction. A major parameter is the gap size. (b) SEM image of fabricated sample. Unit cell size is $7 \times 7\mu m$, nanoring side length is 5 μm. (c) A different example of an asymmetric SSR with additional degrees of tunability, which are the angles indicated in the figure. (d) An image of a fabricated SSR-based metamaterial for the microwave regime. (a,b) adapted from [41], (c) – [42], (d) – [12].

general, metamaterials in the homogenisation regime are equivalent to anisotropic homogeneous media [47–51]. Mostly because of fabrication constraints, as the working wavelength decreases, the characteristic dimensions of the metamaterial unit cell are not much smaller than the wavelength but only slightly smaller. Thus, optical metamaterials often operate in an intermediate, mesoscopic, regime and their homogenisation becomes questionable [52–54].

1.3 Metasurfaces

Fabricating a bulky piece of 3D metamaterial is a very challenging task, particularly in the frequency range going from the visible to the infrared [38, 43]. As a consequence, last 10 years witnessed a growing interest in 2D planar structures that can be realised with standard nanofabrication processes while preserving an excep-

tional control over the flow of light. The study of planar devices is also driven by the need to mitigate losses and to ease integration into optical elements and circuits. Such metamaterials with a reduced dimensionality are currently called metasurfaces, in the sense that they possess optical properties that go far beyond those offered by conventional flat surfaces [55, 56]. In some sense, by going from 3D to planar structures, the optical metamaterials community has followed a similar path compared to the photonic crystal community with the development of photonic crystal slabs.

Generally, metasurfaces (also known as metalattices or metagratings) come in a form of a two-dimensional array whose unit cells are specifically chosen resonant nanoscatterers, sometimes referred to as meta-atoms. Like metamaterials, subwavelength (especially deep subwavelength) metasurfaces can be efficiently modelled as homogenised planar sheets (films) with effective parameters [57–62]. The term "metalens" is often used for metasurfaces that are designed to mimic (and improve upon) the performance of optical lenses [63–68]. They are aimed at achieving wavefront shaping in a general sense (not simply light focusing), mostly in the visible range, while keeping their thickness subwavelength. To achieve a specific wavefront transformation, we need to have a full 2π phase modulation capability. This requires working close to the resonance of the meta-atoms, often packing multiple elements within one unit cell (itself smaller than the wavelength) each giving a certain phase change in the interval $[0,\ 2\pi]$ [69, 70].

In general terms, phase discontinuities on the interface that transform the incident electromagnetic wave into a desired one is the fundamental basis for the functionality of metasurfaces. This idea can be traced back to the Schelkunoff-Huygens principle [71]. Over the years, a substantial work was done to improve the metasurface efficiency [72] and to explore new designs (see, for instance, reviews [55, 73, 74]). Without a doubt, this kind of work will be carried on and expanded further in the following years [75–77].

There are two different types of metasurfaces for the visible and the infrared (see Fig. I.3). The first one employs strongly localised optical resonances induced by metallic nanostructures. This strategy has produced a wide range of devices, such as ultrathin lenses, beam steering devices, and generators of orbital angular momentum of light [78]. The second type of metasurfaces uses arrays of dielectric nanostructures that exhibit geometric Mie-type resonances. This second strategy largely reduces absorption losses [70, 79], enabling high-efficiency beam steering [80], refraction [81], light focusing [82], sensing [83, 84], and holography [85].

Let us now discuss with more detail their differences and commonalities.

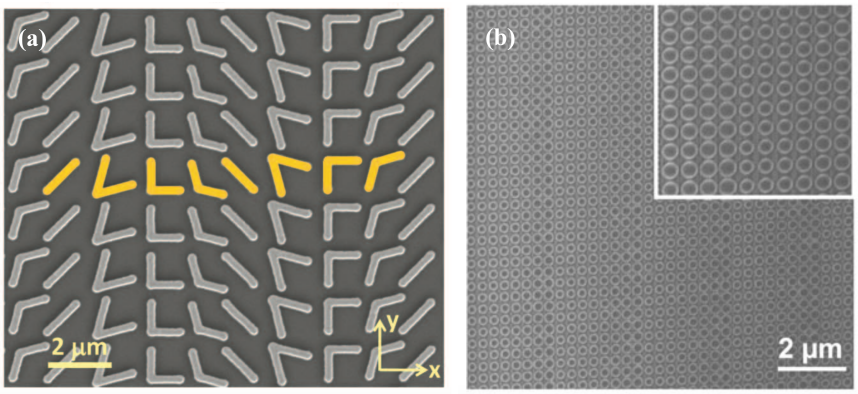

Figure I.3.: Scanning electron microscope (SEM) images of two metasurfaces representing important design principles for plasmonic (a) and dielectric (b) devices. The unit cell in (a) is comprised of eight gold nanoantennas optimised to gradually increase the phase delay of the reflected field to cover the whole $[0,\ 2\pi]$ interval. The unit cell of the metasurface (b) also has a gradient nature. In this case, however, the size, rather than angle of the nanoantenna is modified in order to achieve a similar effect. Image used in (a) is adapted from [69], (b) – [86].

Metallic nanoparticles, such as silver or gold, are called plasmonic, because their resonant nature results from the free electron collective oscillations (plasmons), which leads to the appearance of localised modes known as localised surface plasmon resonances. The resonance (spectral confinement) is associated with a spatial confinement of the electromagnetic field in a small mode volume. However, because of inherent Ohmic losses, especially for infrared and visible regimes, the quality factor of plasmonic resonances remain quite modest, typically in the range 10–50. Ohmic losses mean that some optical energy is being absorbed and transformed into heat. These losses are obviously detrimental for realising efficient optical devices with a high transmission or reflection. On the other hand, absorption is the governing effect for other applications, such as biomedical [87] and photo-/thermo-voltaic [88] among others [89].

Increasing the efficiency of metasurfaces by reducing absorption was a major argument for the study of dielectric (with a large refractive index) nanostructures supporting Mie-type resonances. Of a particular importance to the field is silicon (other popular choices include germanium, gallium phosphide, titanium dioxide, indium tin oxide or silicon nitride, see, for example, review [84] and references therein). The optical properties of such high-index materials are build upon the polarisation charges,

which present inherently lower Ohmic losses. Silicon loss is intrinsically low in the spectral range 0.9—1.65 μm which has led to the design and implementation of several Si-based metasurfaces with transmission higher than 90% and full phase agility over the $[0, 2\pi]$ range [86].

Low losses, while very favourable, is not the only reason for such an enthusiastic development of all-dielectric devices. Planar on-chip fabrication technologies, such as CMOS (Complementary Metal–Oxide–Semiconductor), are well-developed, which would facilitate basic research on metasurfaces, prototyping and eventual potential commercialisation. More crucially, high-index materials possess magnetic-type resonances of comparable strength to the electric ones [90, 91]. A strong magnetic dipole resonance occurs due to a coupling of incoming light to a mode characterised by a circular displacement current. This becomes possible when the wavelength λ/n inside the particle of refractive index n becomes comparable to the particle dimension. In contrast, achieving a similar magnetic response with a plasmonic particle requires complex shapes such as split ring resonators [41, 92] or metallo-dielectric composites, such as metal-insulator-metal (MIM) structures [93–95]. In turn, enhanced electromagnetic fields due to the excitation of the localised surface plasmon resonance in metallic particles can be reproduced with their dielectric counterparts [96]. This is significant as one of the foundational concepts in plasmonics is the large enhancement of the electric field in so-called hot spots. Now, high-index structures are being used to recreate these high electric and magnetic fields concentration spots, while keeping the low losses, to enhance non-linear effects, such as Raman scattering or harmonic generation (see, for example, review [84] and references therein).

The large variety of resonances in dielectric nanostructures enables complex interference phenomena between several excited modes, which in turn drives many novel effects, such as unidirectional scattering [97–101], optical antiferromagnetism [102], optical bound states in the continuum [103, 104], or optical anapoles [103, 105, 106].

2 Electromagnetic modelling in nanophotonics

Since Maxwell's equations are exact for linear materials, their resolution using rigorous numerical methods has always played a very important role in all fields of electromagnetism. Nanophotonics is a perfect example of this statement. The need for numerical computation is even greater because the cost of manufacturing and characterising a structured object at the nanoscale remains high. Thus, to design a photonic component, it is often better to rely on numerical computations rather than

multiple fabrication-characterisation steps.

However, numerical calculation is not necessarily an easy solution. Indeed, one has to calculate light scattering by 3D structures of complex geometry composed of materials with strong refractive index contrasts (thus, far from the perturbation regime). In the case of metasurfaces, the optical response is a complex interplay between the direct scattering from a single unit cell and the multiple scattering between adjacent unit cells. Moreover, non-periodic metasurfaces are characterised by the coexistence of several length scales with large and small dimensions compared to the wavelength. Finally, given the large number of degrees of freedom, the design and optimisation of devices requires tons of calculations. For these reasons, even though today one has easy access to efficient electromagnetic solvers (both commercial and open-source software products) and powerful computers, and recently optimisation techniques have seen huge progress, modelling the optical response of resonant nanostructures is not an easy task.

As a consequence, a variety of different modelling approaches coexist, from simple toy models to rigorous numerical calculations. In the ensuing sections, we give a brief overview of the main techniques used to model the optical properties of resonant nanostructures.

2.1 Exact analytical solutions

Maxwell's equations can be solved exactly and analytically for a few specific problems. By analytical, we do not mean here that no computer has to be used, we mean that the electromagnetic field does not need to be discretised, neither spatially nor spectrally. These "analytical" methods rely on the solving of a linear systems of equations. Among these simple geometries, two are of particular interest, even for real devices:

1. Spherical scatterers. Closed form solutions of Maxwell's equations are provided by Mie theory [107]. Generalisations to spheroids, core-shell spheres, and infinite cylindrical rods are available [108–111];

2. Stratified media. Reflection and transmission by a stack of homogeneous layers can be calculated by stacking 2×2 matrices that simply contains the Fresnel coefficients, the refractive indices, and the thicknesses of the different layers.

These two theories can be extended and combined for the calculation of multiple

scattering by an ensemble of spheres in a homogeneous medium or in a stratified medium [112–115].

2.2 Rigorous numerical methods

Numerical methods that discretise Maxwell's equations have the advantage to be versatile and can be used, in principle, for any geometry.

The family of finite difference time domain methods (FDTD), along with the related finite difference in the frequency domain methods, is largely used in nanophotonics [116, 117]. Probably, the most widely used version is the one based on the Yee's algorithm [118]. Yee suggested to have **E** and **H** shifted by half of the grid step with respect to each other, and to use central spatial and leapfrog time differences for the derivatives. Finite difference algorithms can be implemented on a 1D, 2D, as well as 3D grid. The meshing typically used is cubic, which suits best for dealing with rectangular ridges and leads to step-sensitive approximation of curved surfaces (staircase effect). Even though the computations can be parallelised, a typical Cartesian grid causes them to be usually very computationally expensive.

In contrast stand the finite elements methods (FEM) [116, 119]. They do not experience the same hurdles accounting for the geometry as the finite difference methods do thanks to a tetrahedral mesh. Typically, FEM are used in the frequency domain and are built to solve the inhomogeneous vector wave equation, rather than two Maxwell's equations (Faraday and Ampere's laws), which is the general approach of the FDTD. The tetrahedral mesh does not just model irregularities in the structure better, it also can accommodate smaller meshing size around features that require finer details, and larger one in the bigger homogeneous regions. This increases the overall computational efficiency greatly compared to FDTD.

Another interesting option is the discrete dipole approximation [116, 120]. The idea is to represent a given nanoparticle with a cubic array of small polarisable blocks with dipolar polarisabilities. Despite not being an exact method and employing a discretisation that may neglect some of nanoparticles fine and curved features, this approach has showed promising performance [121].

These methods rely on a full 3D spatial discretisation of the electromagnetic field and require a large amount of memory in the case of 3D complex objects. On the other hand, modal methods are based on a 2D discretisation and an analytical integration along the third dimension. Such techniques usually handle smaller matrices and result in a smaller computational burden. On the other hand, the matrices are

full in contrast to FDTD and FEM that work with sparse matrices. A widely used modal method is the so-called Rigorous Coupled-Wave Analysis (RCWA) [122–127], also known as the Fourier Modal Method. It is based on an expansion of the electromagnetic fields onto a basis of Fourier harmonics. RCWA is dedicated to scattering problems with periodic arrays but can also be extended to aperiodic structures [128, 129].

The main advantage of rigorous numerical methods is their versatility. However, they behave as a black box and do not allow for a clear physical understanding of the results. Moreover, as the complexity of the structures to be modelled increases, the number of degrees of freedom explodes, and the optimisation of devices with a rigorous solving of Maxwell's equations becomes extremely time-consuming.

2.3 Approximate methods

Finally, it is important to mention that numerous approximate methods have been developed for resonant nanophotonics, from toy models to more refined approximate theories. The development of approximate methods is mainly driven by two aspects. First of all, one is rarely fully satisfied with a brute-force calculation and is generally eager to understand the underlying physical mechanism. Secondly, one is always looking for faster calculations in order to accelerate the design and the optimisation of a device.

Widely-used approximate models in nanophotonics are based on the quasi-static approximation. It can be used when the size of the object is much smaller than the wavelength of light. In the context of light scattering by a single object, this approximation stands for the modelling of the scatterer as an electric dipole, whose polarisability is given by a simple analytical expression [116, 130]. In the context of periodic media (photonic crystals, metamaterials), the quasi-static approximation leads to the homogenisation of the structure, so that the new (in general, anisotropic) homogeneous medium can be described by effective optical parameters [34, 130, 131].

In practice, nanophotonic devices do not necessarily fulfil the conditions of the quasi-static approximation. Using such models is then only qualitative. They can help to obtain a coarse physical understanding but they cannot provide accurate predictions. There is clearly some room for improvement, a demand for approximate models that can provide both a good physical understanding and an accurate prediction (i.e., without using fit parameters) of the optical response.

3 Outline of the thesis

The objective of this thesis is to develop semi-analytical models for an efficient modelling of periodic and compact resonant optical nanostructures. By semi-analytical, we mean that the models rely on analytical derivations and closed-form expressions that include some physical parameters, which are calculated with a rigorous numerical method. Such an efficient mix between theory and numerical calculation is realised by starting from a rigorous treatment of the electromagnetic problem and substituting some of the steps with well-chosen analytical approximations. In practice, modal methods constitute a perfect choice for applying this recipe. Indeed, taking into account a large number of modes provides a rigorous, virtually exact, result. On the other hand, if the system response is dominated by the excitation of a few modes, neglecting most of the modes still provides accurate, but now semi-analytical, results. This thesis is divided into three chapters.

In Chapter II we present a semi-analytical model for guided-mode resonances in PhC slabs. By making well-chosen approximations in the RCWA, we show that the problem can be treated as a few-modes Fabry-Perot resonator. Further assumptions allow us to derive analytical expressions of the dispersion curve and the quality factor of leaky modes supported by PhC slabs above the light cone. The multimode Fabry-Perot model provides an insightful and efficient procedure to find and study the so-called bound states in the continuum (BICs) – leaky modes of the PhC slab whose coupling to the continuum of the surrounding space vanishes. Thanks to the semi-analyticity of the multimode Fabry-Perot model, we investigate the dynamics of BICs with the slab thickness in symmetric and asymmetric PhC slabs.

Chapter III switches from PhC slabs to finite 3D scatterers, whose resonant nature can be accurately described by considering their eigenmodes. This approach, known as quasi-normal mode expansion (or resonant-state expansion), has recently undergone very important developments. Considering a large number of modes provides, in principle, a rigorous solution of the electromagnetic problem. On the other hand, neglecting weakly excited modes to keep only a few dominant ones provides approximate but accurate systems. The semi-analyticity comes in that case from the fact that, once the modes have been calculated rigorously, their excitation coefficient (how strongly a mode is excited by a given incident field) can be derived analytically. We apply quasi-normal mode expansion to the calculation of the scatterer T-matrix, which is an intrinsic characteristic of a scatterer that relates linearly any incident field to the corresponding scattered field. The objective is to subsequently

use the semi-analytical calculation of the T-matrix in a multiple scattering formalism to calculate the response of an ensemble of scatterers from the sole knowledge of a few eigenmodes of its constituents. Despite recent important developments, quasi-normal mode expansion techniques are still less mature than other rigorous numerical methods. Because of this, we test the accuracy of our modal expansion of the T-matrix in cases when either a small or a large number of modes is taken into account. We propose two different modal decompositions and show that one of them provides improved accuracy and convergence speed.

Finally, in Chapter IV, we use the results of the previous chapter and combine the modal expansions of the T-matrices of different objects with a multiple scattering theory. We first calculate analytically the T-matrix of a metallic nanorod from the knowledge of its eigenmodes. Then, we use this modal expansion of the T-matrix to calculate scattering by a dimer of metallic nanorods, emission of a dipole source inserted in a Yagi-Uda antenna composed of metallic nanorods, and absorption in a periodic array of the same nanorods. In each case, the sole knowledge of the fundamental mode of the nanorods allows for an approximate reconstruction, which contains most of the physics. Increasing the number of modes improves the accuracy. The results are compared with the rigorous FEM calculation. The strengths and weaknesses of the modal expansion are discussed.

Chapter II

Bound states in the continuum in photonic crystal slabs

In this chapter we present a multimode Fabry-Perot model that allows for a simple yet quantitative analysis of the interference mechanism at the origin of the existence of leaky modes in one-dimensional photonic crystal (PhC) slabs. We apply the multimode Fabry-Perot model with either two or three Bloch waves (BWs) inside the photonic crystal. For some specific values of the optogeometric parameters, a leaky mode supported by a PhC slab can become a truly guided mode, even if it lies above the light cone, i.e., within the radiation continuum. These are the so-called bound states in the continuum (BICs). Thanks to its semi-analytical character, the model allows for easy calculations of the bound states in the continuum positions in the dispersion diagram and their variation as a function of the slab thickness.

We apply the multimode Fabry-Perot model to the calculation of the dispersion curve and the quality factor of leaky modes supported by 1D PhC slabs of varying thickness. We show that the model is able to quantitatively predict the appearance of bound states in the continuum and their position in the parameter space. We show that, regardless of the slab thickness, BICs cannot exist below a cut-off frequency, which is related to the existence of the second-order Bloch wave in the photonic crystal. Thanks to the semi-analyticity of the model, we investigate the dynamics of BICs with the slab thickness in symmetric and asymmetric photonic crystal slabs.

This chapter is structured as follows. Fist of all, Section II.1 defines and briefly discusses the BIC phenomenon. Following, Sec. II.2 introduces the concept of a PhC slab made of a high refractive index material and comments on its principal optical properties. In Sec. II.3 we introduce and discuss in details to different kinds of BICs that can exist in 1D photonic crystal slabs: symmetry-protected and resonance-trapped. Section II.4 is dedicated to the multimode Fabry-Perot model itself. We begin by presenting the BWs that propagate in a periodic medium and how they can be used to calculate PhC slab dispersion (Subsec. II.4.1). Subsection II.4.2 considers the simplest case of a single propagative BW. Successive Subsections II.4.3 and II.4.4 expand the model for the cases of two and three BWs by reducing them to

the single BW case with effective reflection coefficients. The accuracy of the model is further verified against the Rigorous Coupled Wave Analysis (RCWA) calculation, which takes into account a large set of BWs (Sec. II.5). Its limitations are discussed in Sec. II.6. Finally, leveraging on the semi-analyticity of the model, in Sec. II.7 we study and discuss the behaviour of BICs with varying slab thickness for symmetric (Subsec. II.7.1), asymmetric (Subsec. II.7.2), and mounted on a substrate (Subsec. II.7.3) PhC slabs.

1 What is a bound state in the continuum?

In recent years, a lot of interest was generated around the phenomenon of what is now commonly known as bound states in the continuum [103, 104, 132, 133]. A BIC (also called embedded eigenvalue [134]) is a bound state that exists at the same energy level as a continuum of radiation modes [135, 136]. In PhC slabs, it corresponds to an eigenmode that is truly guided (no radiative leakage) despite the fact that it lies above the light cone in the dispersion diagram $\omega = f(\mathbf{k})$, with ω the angular frequency and $\mathbf{k}$ the wave vector. In principle, eigenmodes lying above the light cone should be leaky; they are expected to decay as they propagate due to radiative leakage.

The absence of leakage (the fact that the state is bound) originates from two different physical mechanisms: symmetry incompatibility between the mode and the radiation continuum for so-called symmetry-protected BICs or destructive interference between different leakage channels for so-called resonance-trapped or Friedrich-Wintgen BICs [104, 133, 136].

From a strictly theoretical point of view, BICs, and especially the ones resulting from an interference mechanism, are definitely counter-intuitive and intriguing modes. From a practical point of view, however, BICs do not really exist. Indeed, in a real non-ideal structure, they are anyway faintly coupled to the radiation continuum because of technological imperfections, roughness, or finite size of the device. A BIC thereby becomes a leaky mode with extremely low leakage, i.e., with a very large quality factor Q. Therefore, if a PhC slab can be fabricated with geometrical parameters close enough to the ideal ones, it would exhibit a very sharp resonance with an extremely high quality factor whose value is only limited by technological constraints. Such high-Q resonances that result from the existence of a BIC nearby in the parameter space have been recently investigated [137–139] and exploited for lasing [140, 141] and sensing applications [83, 142, 143].

Up to now, the existence of BICs and their location in the parameter space has been calculated either with rigorous numerical methods [104, 140, 144–148] or with various perturbative techniques based on coupled-wave theory [132, 149–152]. Fully numerical approaches are cumbersome even for simple geometries since the whole parameter space has to be explored blindly to find a BIC. In addition, this blind exploration has to be done with a very fine grid since BICs are usually narrow features in the parameter space. Using a perturbation approach is an interesting alternative. However, if coupled-wave theory is accurate for PhC slabs with a low refractive index contrast, the accuracy drops as the contrast increases. Iterative schemes have been proposed to improve the accuracy of the coupled-wave formalism for high refractive index contrasts but at the cost of a drastic loss in simplicity [150].

To ease the practical implementation of PhC slabs supporting BICs, in particular with semiconductor materials, one needs approximate models that yield fast yet accurate predictions of the BIC location in the parameter space. Improving the understanding of the physical mechanisms that lead to the BIC formation is also an important issue. We propose a semi-analytical model that does not rely on a perturbative approach. The model presents a couple of major advantages. First, it explicitly contains the interference mechanism that leads to the formation of a BIC. And second, it yields quantitative predictions of the corresponding optogeometric parameters for any refractive index contrast.

2 High-contrast photonic crystal slab

We start with a glance at the optical properties of a lamellar 1D PhC slab, that is, a periodic array of slits in a dielectric membrane with refractive index $n_d = 3.5$ embedded in air, as shown in Fig. II.1(a). The PhC period, the membrane thickness, and the filling factor in dielectric material are respectively denoted with a, h, and F. We study the leaky modes supported by this structure in Transverse Electric (TE) polarisation, i.e., with electric field polarised along the slits in the y direction. This structure is also known as a high-contrast grating [153–155].

When a plane wave is incident on the photonic crystal slab, we can distinguish two main operation regimes of a subwavelength photonic crystal slab: resonant and broadband reflector [155]. The two corresponding reflection spectra are depicted in Fig. II.1(b). Since the material is transparent, the transmission is simply given by $T = 1 - R$. In the resonant regime we can observe sharp Fano features, which is an indication of a plane wave (continuum of the outside free-space modes) coupling to

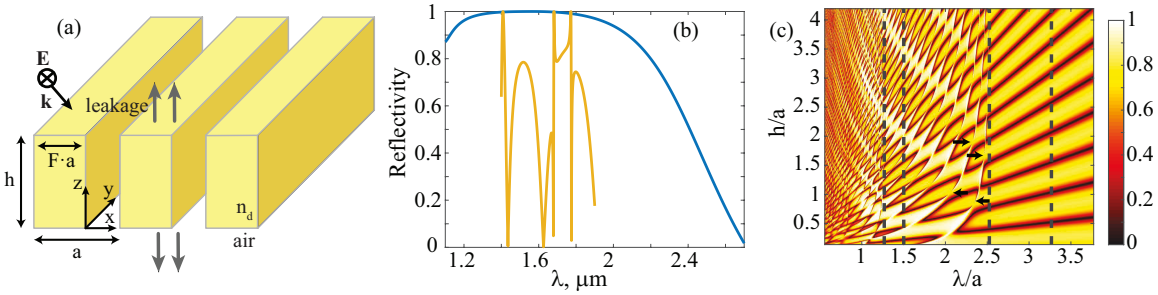

Figure II.1.: (a) Schematic of the symmetric 1D PhC slab under study. Main parameters are the PhC period a, the filling factor F, defined as the fraction of the dielectric material, the refractive index n_d, and the slab thickness h. TE-polarised incident field is schematically marked as well. (b) Two regimes of the PhC slab (HCG): broad band reflector (blue line) and resonant (yellow). Parameters are taken from [155]. Namely, for the blue line: $a = 772$ nm, $h = 502$ nm, $F = 0.77$, $n_d = 3.2137$, TM-polarisation; for the yellow one: $a = 716$ nm, $h = 1494$ nm, $F = 0.7$, $n_d = 3.48$, TE-polarisation. (c) Reflectivity contour of a 1D PhC slab [parameters same as for the reflective regime in (b)] as a function of excitation wavelength λ and slab thickness h. Black dashed lines mark second to fourth Bloch waves cuttoffs respectively from the right. Arrows point to a region where the Fano resonance feature disappears and BIC emerges.

a discrete leaky state of the PhC slab. This phenomenon is known as a guided-mode resonance. By tuning optogeometric parameters, this feature can be made infinitely narrow until it eventually disappears [see the arrows in Fig. II.1(c)] when leaky mode of the PhC slab becomes a BIC [138]. This means that the discrete leaky state is no longer coupled to the outside space and a BIC emerges.

Figure II.1(c) shows the slab reflectivity colour map versus the normalised λ/a and the thickness for the case of normal incidence and TE-polarisation. This characteristic pattern exhibits a few distinct regimes of the slab performance, divided by the vertical dashed lines, which correspond to the cut-offs of the BWs that propagate vertically in the periodic medium. The right-most region is the deep-subwavelength (homogenisation) regime, where only a single BW is propagative. One can immediately recognise interference fringes due to the Fabry-Perot mechanism in a homogeneous slab. To the left of it, roughly between $\lambda/a = 2.5$ and 3.3, is the two BWs region. We do not, however, see any interference pattern yet, as, at the normal incidence, the second BW is decoupled from the outside space and cannot be excited with an incident

plane wave. Shifting farther to the left, we observe an intricate pattern created by the first three BWs interference. Precisely this interference, when totally destructive, leads to the total cancellation of the radiation and emergence of a BIC, and lies in the foundation of the semi-analytical model introduced later in this chapter. As we move further to smaller wavelengths, adding more and more propagating BWs, this pattern becomes more and more complex. The complexity is further exacerbated when diffraction orders emerge, as the wavelength becomes smaller than the period.

Let us emphasise that the multimode Fabry-Perot model is particularly well-suited for the study of the resonant behaviour (such as appearance of BICs) of PhC slabs. First, it is derived from a rigorous theory (the RCWA) simply by neglecting evanescent waves. Therefore, the BWs used in the model to build the transverse resonance are not virtual intermediary means for the calculation; they have a clear physical meaning, even in the case of structures far from the perturbation regime. They exactly correspond to the channels that destructively interfere to form a BIC. Secondly, the BWs are bouncing back and forth vertically inside the PhC slab. The slab thickness is thus a crucial parameter to understand the formation of BICs by destructive interference. The model predictions are analytical with respect to this geometrical parameter. Thirdly, BWs possess cut-off frequencies below which they cannot propagate. Since the multimode Fabry-Perot model contains them explicitly, the zones in the (ω, k) space where BICs of different composition, judging by the number of constituent BWs, can exist become apparent with very few calculations. In particular, the model allows us to evidence the existence of a cut-off frequency (related to the second-order BW) below which no BIC can exist, regardless of the slab thickness.

3 Two types of BICs

The eigenmodes of the PhC slab are characterised by a wavevector $\mathrm{k} = (k_x, k_y)$ and an eigenfrequency $\tilde{\omega} = 2\pi c/\tilde{\lambda}$. Because of radiative leakage – for modes with a real wave vector located above the light cone – the eigenfrequencies are complex with a non-zero imaginary part. The latter is related to the mode quality factor,

$$Q = \mathrm{Re}(\tilde{\lambda})/[2\mathrm{Im}(\tilde{\lambda})]. \tag{II.1}$$

Numerical calculations are performed with the RCWA [123]. The leaky modes (or in fact quasi-normal modes, see Chapter III) of the PhC slab are calculated by searching for the poles of the scattering matrix in the complex frequency plane [156, 157]. The

number of Fourier harmonics retained in the expansion of the electromagnetic field is $2M + 1$ with $M = 30$.

Figure II.2 shows the different types of BICs that can exist in a symmetric 1D PhC slab. It also evidences the crucial role of the slab thickness in the formation of BICs. Figure II.2(b) displays the dispersion curves of the four leaky modes with the lowest frequency for $h = 0.71a$ and $F = 0.6$. The normalised frequency $a/\mathrm{Re}(\tilde{\lambda})$ of the modes has been calculated as a function of the normalised x-component of the wavevector $k_x a/(2\pi)$, which is varied inside the first Brillouin zone, for a fixed $k_y = 0$ (non-conical mount). The quality factors of the four modes are shown in Fig. II.2(c). Two modes (green and blue curves) exhibit a BIC along their dispersion curve while the other two (black curves) do not. Indeed, the quality factor of the green mode diverges for $k_x = 0$ and that of the blue mode diverges for $k_x = 0.046(2\pi/a)$. The locations of these two BICs in the dispersion diagram are shown with dots labelled (1) and (2) in Fig. II.2(b). The corresponding electric fields are displayed in Fig. II.2(d).

The existence of the BIC labelled (1) at $k_x = 0$ (Γ point) can be easily understood: radiative leakage is prohibited due to symmetry incompatibility. The field profile of the mode is antisymmetric with respect to x, $E_y(-x, z) = -E_y(x, z)$, and it cannot couple to the symmetric profile of a plane wave with $k_x = 0$. [1] These non-leaky modes had been identified in earlier works on PhC slabs without referring to them as BICs. In recent literature they are often defined as symmetry-protected BICs [104, 133].

The existence of the BIC labelled (2) is more intriguing. Since $k_x = 0$, its field does not present any symmetry. It should, in principle, be coupled to the radiation continuum. However, radiative leakage is exactly suppressed at $k_x = 0.046(2\pi/a)$. This "accidental" disappearance of leakage results from destructive interference between several leakage channels [104]. In the literature, this type of BIC is referred to as resonance-trapped BIC [133, 140] or Friedrich-Wintgen BIC [136].

As the slab thickness increases to $h = 1.62a$ (same filling factor $F = 0.6$), more modes appear in the spectral range of interest and the number of BICs increases as well, see Figs. II.2(e)-(h). Our calculations show five BICs whose locations in the dispersion diagram of Fig. II.2(f) are marked with the dots labelled from (1) to (5). The corresponding electric fields are shown in Fig. II.2(h). Figure II.2(g) displays the quality factors of the three leaky modes that exhibit one or two BICs along their dispersion curve. The green mode has a diverging quality factor at $k_x = 0$ and

[1] Since we plot the absolute value of E_y in Fig. II.2, we identify the ones which have zero field magnitude in the centre of symmetry as antisymmetric. Similarly, a field profile with non-zero magnitude in the central cross-section of the ridge is called symmetric.

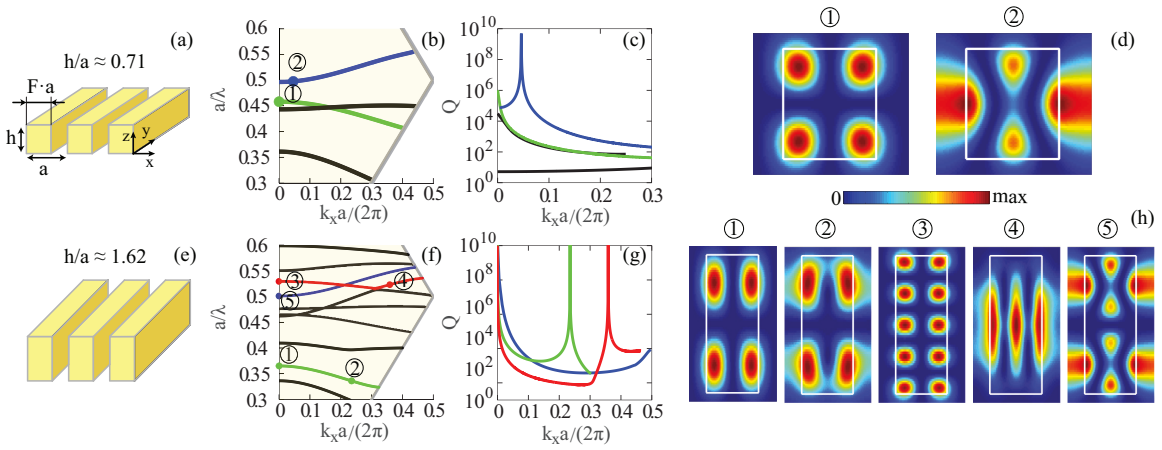

Figure II.2.: BICs in symmetric PhC slabs for two different values of the slab thickness, $h = 0.71a$ (a)-(d) and $h = 1.62a$ (e)-(h). (a) and (e) Schematics of the structure. The filling factor and the refractive index of the dielectric material are fixed, F = 0.6 and $n_d = 3.5$. (b) and (f) Dispersion diagrams of the leaky modes above the light cone (grey line). The bands represented with coloured curves exhibit BICs for some particular values of the wave vector k_x shown by coloured dots. (c) and (g) Quality factors Q of the leaky modes with the same colours as in the dispersion diagram. BICs correspond to Q-factors that tend to infinity (numerically larger than 10^9). (d) and (h) Electric-field distributions $|E_y(x, z)|$ of the BICs shown by coloured dots in (b) and (e). A single period is represented; edges of the dielectric ridge are shown with white lines.

another one at $k_x = 0.235(2\pi/a)$. The first one is a symmetry-protected BIC with an antisymmetric field profile (1) while the second one is a resonance-trapped BIC with a field profile (2) that is almost antisymmetric but not fully. Similarly, the red mode is a symmetry-protected BIC at $k_x = 0$ [antisymmetric field profile (3)] and a resonance-trapped BIC at $k_x = 0.3587(2\pi/a)$ [field profile (4)]. It is important to note that the latter has an almost symmetric field profile, see (4) in Fig. II.2(h), in contrast to the resonance-trapped BIC labelled (2), which has a quasi-antisymmetric field. Finally, the blue mode exhibits a BIC at $k_x = 0$. Since its field profile (5) is symmetric, it cannot be a symmetry-protected BIC but rather a resonance-trapped BIC resulting from destructive interference.

So far, we can only observe in Figs. II.2(f)-(h) that four BICs among five are different in nature. Only BICs (1) and (3) are similar; they are symmetry-protected BICs at $k_x = 0$ with an antisymmetric field profile. The usual classification with two

categories (symmetry-protected and resonance-trapped BICs) is clearly not sufficient to fully characterise BICs in 1D PhC slabs. We summarise in Table II.1 the four different types of BICs that can be inferred from Fig. II.2(f)-(h). We will see in Sec. II.4 that the multimode Fabry-Perot model provides a clear physical understanding of the differences between all four types BICs.

First, as already discussed in the literature, BICs can be separated in two families, symmetry-protected BICs and resonance-trapped BICs. For the first ones, leakage is forbidden because of symmetry incompatibility between the mode of the PhC slab and the radiative plane wave. These BICs can only exist at $k_x = 0$; they have necessarily an antisymmetric field profile. Their existence does not depend on the geometrical parameters of the PhC slab, provided that the horizontal symmetry is conserved. Secondly, leakage can also be suppressed by destructive interference, resulting in the appearance of a resonance-trapped BIC. Figures II.2(f)-(h) evidence that this BIC family can be split in three different subcategories. Resonance-trapped BICs can exist at $k_x = 0$ with a symmetric field profile or at $k_x \neq 0$. In the latter case, the field profile presents no strict symmetry, but it is either quasi-symmetric [e.g., BIC (4) in Fig. 1(h)] or quasi-antisymmetric [e.g., BIC (2) in Fig. 1(h)]. By the prefix quasi, we mean that the BIC belongs to the dispersion curve of a leaky mode that is either symmetric or antisymmetric at $k_x = 0$. In contrast to the symmetry-protected BICs, the existence of resonance-trapped BICs formed by destructive interference strongly depends on the geometrical parameters. It is thus difficult to predict their precise position along the dispersion curve.

4 Multimode Fabry-Perot model

Bound states in the continuum in PhC slabs are leaky modes whose radiative leakage vanishes for a particular set of parameters. Their modelling is intrinsically linked to the phenomenon of guided-mode resonance, which corresponds to the resonant excitation of a leaky mode. Over the years, guided-mode resonance has been described by several theoretical formalisms, such as, for instance, coupled-wave theory [30], perturbation methods [32], or pology framework [28, 31]. Of particular interest to the objectives of this thesis is an approach that consists of modelling the reflection and transmission of a PhC slab as a transverse Fabry-Perot resonance composed of a small number of BWs bouncing back and forth inside the slab. This approach has been first proposed as a qualitative interpretation of the high reflectivity of PhC slabs [29]. It has been made quantitative with $N = 2$ waves in 2006 [33]. Then, this

Table II.1.: Classification of BICs in symmetric 1D PhC slabs according to their symmetry properties along the horizontal x-axis. The symmetry-protected BICs that result from a symmetry incompatibility necessarily have an antisymmetric field profile at $k_x = 0$ and cannot exist at $k_x \neq 0$. The resonance-trapped BICs formed by destructive interference can exist equally at $k_x = 0$ (with a symmetric field profile) or at $k_x \neq 0$. An antisymmetric (resp. symmetric) field corresponds to $E_y(-x, z) = -E_y(x, z)$ [resp. $E_y(-x, z) = E_y(x, z)$]. By quasi-symmetric (resp. quasi-antisymmetric), we mean that the field profile of the BIC is almost symmetric (resp. almost antisymmetric), see BICs labelled (2) and (4) in Fig. II.2(h). The last line of the Table gives the number of BWs that interfere to form a BIC. This can be learned from the multimode Fabry-Perot model.

Symmetry-protected BICs		Resonance-trapped BICs		
$k_x = 0$	$k_x \neq 0$	$k_x = 0$	$k_x \neq 0$	
antisym	—	sym	quasi-sym	quasi-antisym
2^{nd} BW	—	3^{rd} BW $+1^{\text{st}}$ BW	3^{rd} BW $+1^{\text{st}}$ BW $+2^{\text{nd}}$ BW	2^{nd} BW $+1^{\text{st}}$ BW

multimode Fabry-Perot model has been used by several authors to study the optical properties of high contrast gratings [153–155].

In what follows, we derive a semi-analytical model that predicts the dispersion curve and the quality factor of leaky modes supported by a PhC slab. We extend the approach proposed in Ref. [33] for the calculation of the reflection and transmission of a PhC slab. In particular, we introduce more analyticity in the calculation. A leaky mode is nothing but a transverse Fabry-Perot resonance composed of several BWs bouncing back and forth vertically inside the slab. This description is perfectly rigorous as long as a sufficiently large number M of waves is taken into account. This is the mathematical ground of RCWA [123]. In the case of subwavelength periodic structures, only a small number N of BWs are propagative, the other ones being evanescent [33, 158]. Neglecting the impact of the evanescent waves provides approximate closed-form expressions that can be very accurate, provided that the slab thickness is large enough, typically larger than the decay length of the least attenuated evanescent wave [33].

4.1 Photonic crystal modes as a mixture of Bloch waves

Before building a multimode Fabry-Perot resonance in a PhC slab of thickness h, we need to solve the problem of a single interface between a semi-infinite PhC and a semi-infinite homogeneous medium [see Fig. II.3(a)]. We denote by β_i the propagation constant of the i^{th} BW along the vertical z direction. In a non-absorbing PhC, β_i is either purely real (propagative wave) or purely imaginary (evanescent wave). The number of propagative BWs depends on the geometry. For example, for $k_x = 0$, $F = 0.6$, and $n = 3.5$, only up to three BWs are propagative in the band $a/\lambda < 0.6$. Their propagation constants are shown in Fig. II.3(b), where we can observe the second and third BW cut-offs at $a/\lambda = 0.327$ and $a/\lambda = 0.45$, respectively. Note that the fundamental BW (largest propagation constant, blue curve) has no cut-off and is propagative regardless of the a/λ value. The corresponding field profiles $E_y(x)$ are shown in Fig. II.3(c). The fundamental BW is symmetric and the higher-order BWs have alternately an antisymmetric or a symmetric field profile. For $k_x \neq 0$, the cut-off frequencies vary with k_x and the BWs are no longer strictly symmetric nor antisymmetric.

As the i^{th} BW is incident on an interface with a homogeneous medium, it is reflected with a reflection coefficient r_{ii}. In addition, it is reflected into a different BW with a cross-reflection coefficient r_{ij}, and transmitted as a propagative plane wave with a transmission coefficient t_i. The coefficients r_{ii}, r_{ij}, and t_i are the generalised Fresnel coefficients for an interface between homogeneous and periodic media. Note that we limit ourselves to the case where a single plane wave is propagative in the homogeneous medium – the zeroth diffraction order of the PhC slab. The energy contained in this plane wave corresponds to the radiative leakage.

In a PhC slab of thickness h, the BWs are reflected at the top and bottom interfaces. Thus, they propagate back and forth inside the slab, as illustrated in Fig. II.3(d). We denote by u_i^+ and u_i^- the amplitudes of the up- and down-propagating i^{th} wave, respectively. The phase origin for the amplitude u_i^+ (resp. u_i^-) is taken at the bottom interface (resp. the top interface).

Leaky modes of a PhC slab are solutions of Maxwell's equations in the absence of an incident wave. If one considers a finite number M of BWs (propagative and evanescent BWs), the amplitudes u_i^+ and u_i^- are related by

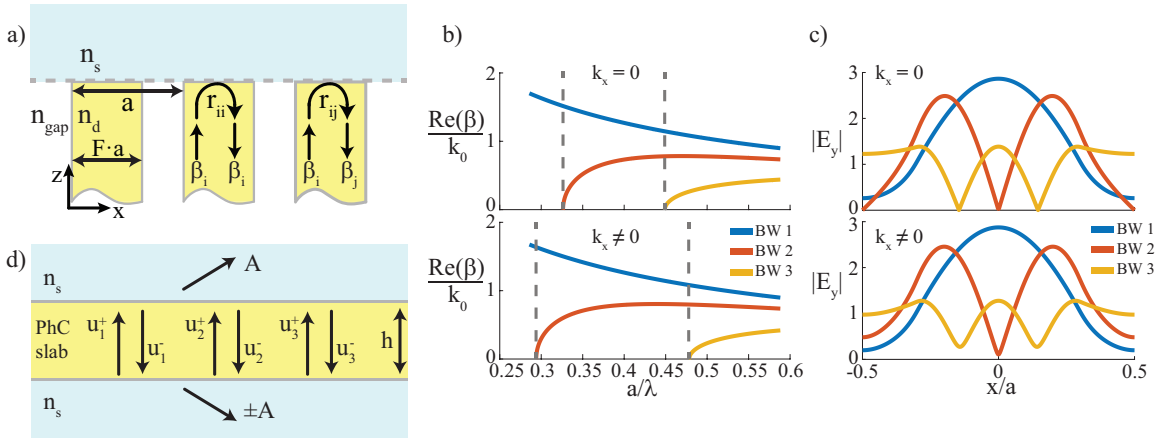

Figure II.3.: Multimode Fabry-Perot model. (a) Interface between a semi-infinite PhC and a homogeneous medium. The refractive index of the homogeneous medium n_s can be different from the index n_{gap} inside the slits of the PhC. At the interface, the Bloch waves (propagation constants β_i) propagating in the periodic medium are reflected with a reflection coefficient r_{ii}, cross-reflected with a reflection coefficient r_{ij}, or transmitted with a transmission coefficient t_i. (b) Normalised propagation constants of the BWs for $F = 0.6$ as a function of the frequency at the Γ-point ($k_x = 0$) and at $k_x = 0.2a/(2\pi)$. The cut-off frequencies of the second and third BWs are shown by vertical dashed lines. (c) Electric-field profile $|E_y(x)|$ of the three propagative BWs for $a/\lambda = 0.526$. (d) Principle of the multimode Fabry-Perot model. In the spectral range of interest, up to three BWs can propagate back and forth inside the PhC slab, all other BWs being evanescent. Each BW is transmitted in the surrounding medium with its own phase. The amplitude A of the plane wave propagating away (radiative leakage) results from the interference between these three contributions.

$$\begin{aligned} u_i^+ &= \sum_{j=1}^{M} r_{ji} u_j^- \exp(i\beta_j h), \\ u_i^- &= \sum_{j=1}^{M} r_{ji} u_j^+ \exp(i\beta_j h). \end{aligned} \tag{II.2}$$

The number M of BWs is equal to the truncation rank of the Fourier series in RCWA [123], $M = 30$ for the calculations shown in Fig. II.2. For the sake of simplicity, we consider a PhC slab surrounded by the same homogeneous medium above and

below. The equations can be straightforwardly generalised to the case of two different media (e.g., for a PhC slab lying over a substrate, as discussed in Subsec. II.7.3); two different families of reflection coefficients r_{ji}^{T} and r_{ji}^{B} have to be considered [159].

Equations (II.2) can be rewritten in a matrix form

$$\mathbf{R}(k_x, \lambda)\mathbf{U} = 0, \tag{II.3}$$

where the vector $\mathbf{U}$ is built with the amplitudes u_i^+ and u_i^-, $\mathbf{U} = [u_1^+, u_1^-, ..., u_M^+, u_M^-]^t$, and the matrix $\mathbf{R}(k_x, \lambda)$ contains all reflections and cross-reflection coefficients. A leaky mode is a non-trivial solution of this linear system of equations; it corresponds to a pair $(k_x, \tilde{\lambda})$ (with k_x a real number and $\tilde{\lambda}$ a complex number) that satisfies [146]

$$\det\left[\mathbf{R}(k_x, \tilde{\lambda})\right] = 0, \tag{II.4}$$

with det being the determinant of a matrix. We calculate rigorously with RCWA the parameters of a single interface (β_i, r_{ii}, r_{ij}, t_i), and thus the matrix $\mathbf{R}(k_x, \lambda)$, as a function of the wavelength for a fixed value of the wave vector k_x. Then, Eq. (II.4) can be solved, typically with an iterative procedure such as the Newton algorithm or a different method using a Padé approximation [156], to find the complex wavelength $\tilde{\lambda}$ of the leaky mode. The dispersion curve and the quality factor are then given respectively by $a/\mathrm{Re}(\tilde{\lambda}) = f(k_x)$ and $Q = \mathrm{Re}(\tilde{\lambda})/[2\mathrm{Im}(\tilde{\lambda})]$.

Regarding the radiative leakage, the amplitude of the outgoing propagative plane wave is given by

$$A = \sum_{j=1}^{M} t_j u_j^+ \exp(i\beta_j h). \tag{II.5}$$

The radiative leakage results from the interference of the BWs amplitudes being transmitted by the interface. Therefore, the leaky mode of the PhC slab is a BIC if, and only if, the interference is perfectly destructive. One readily realises the crucial role of the slab thickness h in this mechanism since it drives the value of the phase difference between the different BWs.

Solving Eq. (II.4) for a large number M of BWs, hence containing a bunch of evanescent waves, yields a rigorous and exact result for the dispersion curve and quality factor. On the other hand, since the period of the PhC slab is subwavelength, neglecting all the evanescent BWs to keep only a small number $N < M$ of propagative BWs drastically reduces the size of the linear system in Eq. (II.2). Within this approximation, it is possible to derive closed-form expressions for the dispersion curve,

the quality factor Q, and the radiative leakage A, as shown hereafter. In particular, these expressions provide analytical results with respect to the thickness h. Note that each of the N propagative BWs is calculated rigorously with $2M + 1$ Fourier terms.

4.2 Transverse resonance for $N = 1$ wave

Let us start with the simplest case $N = 1$ when a single BW is propagative inside the PhC slab, all the other waves being evanescent. Although self-evident, this case allows us to introduce the main equations of the model. The single-mode regime occurs when the period-to-wavelength ratio a/λ is small, typically between the limit $a/\lambda \to 0$ (quasi-static limit) and the cut-off of the second BW. For the example in Fig. II.3(b), it corresponds to $a/\lambda < 0.272$ for all k_x values from zero to the light line.

For a single propagative BW, Eq. (II.4) simply reduces to the usual resonance condition of a Fabry-Perot resonator

$$1 - r_{11}^2 \exp(2i\beta_1 h) = 0\,. \tag{II.6}$$

With no further assumption, the complex wavelengths that satisfy Eq. (II.6) has to be found numerically, typically with an iterative algorithm. In order to derive closed-form expressions of the dispersion curve and, most of all, of the quality factor, we make two additional assumptions. We assume that (i) the quality factor of the resonance is large, $Q \gg 1$, and (ii) the modulus of r_{11} varies slowly with the wavelength over the resonance bandwidth, $\partial|r_{11}|/\partial\lambda \approx 0$. The validity of these assumptions will be discussed in Sections II.5 and II.6. They are important to really reach closed-form expressions of the dispersion curve and the quality factor. Without them, one would have to solve Eq. (II.6) iteratively for every value of the slab thickness and the model would not be analytic with respect to h.

With these two assumptions, an eigenmode of the PhC slab corresponds to a BW that returns in phase after half a round trip [160, 161],

$$\Phi_T(\lambda_0, k_x) = \beta_1 h + \arg(r_{11}) = p\pi\,, \tag{II.7}$$

where $\lambda_0 = \mathrm{Re}(\tilde{\lambda})$ and p is an integer. The phase Φ_T is the total phase accumulated by the BW after half a round trip inside the slab. This phase-matching condition gives an implicit definition of the dispersion curve. The quality factor Q is given by [161, 162]

$$Q = -\frac{\lambda_0}{1-|r_{11}|^2}\frac{\partial \Phi_T}{\partial \lambda}\,, \tag{II.8}$$

where the derivative and the reflection r_{11} are taken at $\lambda = \lambda_0$.

Within the Fabry-Perot model with $N = 1$ propagative BW, the amplitude A of the radiated plane wave is simply proportional to the BW amplitude inside the slab,

$$A = t_1 u_1^+ \exp(i\beta_1 h)\,. \tag{II.9}$$

In this case, the leakage does not result from the interference between several channels. It vanishes if, and only if, the transmission t_1 is strictly equal to zero. This, however, never happens for symmetry reasons. It means that in order for Bloch-wave-to-plane-wave transmission t_i to disappear, the BW must have an antisymmetric field profile at $k_x = 0$, in contrast to the symmetric profile of the plane wave. Since the fundamental Bloch wave $i = 1$ has a symmetric field profile at $k_x = 0$, t_1 has always a non-zero value.

The Fabry-Perot model allows us to draw an important conclusion: no BIC can exist at a frequency where a single BW is propagative. This result sets a spectral cut-off to this existence of BICs, see Fig. II.3(b). We emphasise that this cut-off is independent of the slab thickness.

4.3 Transverse resonance for $N = 2$ waves

For larger period-to-wavelength ratios, the second BW, which has an antisymmetric field profile, becomes propagative, see Fig. II.3(b). Let us start with the situation $k_x = 0$. Since the fundamental BW is symmetric whereas the second BW is antisymmetric, see Fig. II.3(c), the cross-reflections r_{12} and r_{21} are equal to zero and Eqs. (II.2) reduce to two uncoupled sets of two equations each:

$$\begin{aligned} u_i^+ &= r_{ii} u_i^- \exp(i\beta_i h), \\ u_i^- &= r_{ii} u_i^+ \exp(i\beta_i h), \end{aligned} \tag{II.10}$$

with $i = 1, 2$. As a consequence, leaky modes result from a transverse resonance built either with the fundamental BW alone or with the second BW alone. The dispersion curve and the quality factor are given by Eqs. (II.7) and (II.8) with either (β_1, r_{11}) or (β_2,r_{22}).

Because of the symmetry mismatch between the BW and the propagative plane

wave, $|r_{22}| = 1$ and $t_2 = 0$. Therefore, the mode of the PhC slab that corresponds to a transverse resonance built with the second BW alone is necessarily a BIC whatever the geometrical parameters. In particular, varying the slab thickness h shifts the dispersion curve according to the phase-matching condition but the Q-factor remains infinite (since $|r_{22}| = 1$) and this mode at $k_x = 0$ is truly guided with no radiative leakage. It is the aforementioned symmetry-protected BIC, which results from symmetry incompatibility (see Table II.1).

As we depart from the Γ-point, the BWs become coupled, since $r_{12} \neq 0$ and $r_{21} \neq 0$. As a consequence, Eqs. (II.2) become a set of four coupled equations and any transverse resonance results from the interplay between both BWs.

$$\begin{aligned} u_1^+ &= r_{11}u_1^- \exp(i\beta_1 h) + r_{21}u_2^- \exp(i\beta_2 h), \\ u_1^- &= r_{11}u_1^+ \exp(i\beta_1 h) + r_{21}u_2^+ \exp(i\beta_2 h) \\ u_2^+ &= r_{12}u_1^- \exp(i\beta_1 h) + r_{22}u_2^- \exp(i\beta_2 h), \\ u_2^- &= r_{12}u_1^+ \exp(i\beta_1 h) + r_{22}u_2^+ \exp(i\beta_2 h). \end{aligned} \tag{II.11}$$

It is possible to replace such two-waves resonator with the usual single-wave Fabry-Perot by introducing an effective reflection coefficient r_{eff} [159]. The effective reflection fully includes the impact of the second wave. For $k_x = 0$, a leaky mode is a purely single-wave transverse resonance built either with the fundamental BW or with the second BW. When k_x becomes non-zero, both BWs are mixed but one keeps a larger contribution than the other. For instance, for a band with a symmetry-protected BIC at $k_x = 0$ [green curves in Figs. II.2(b) and (f)], $|r_{11}| < |r_{22}|$ and $|r_{12}| < |r_{22}|$. In that case, the second BW is dominant and we incorporate the effect of the first BW in the effective reflection coefficient. The resonance condition given by Eq. (II.4) becomes

$$1 - \left(r_{\text{eff}}^{(12)}\right)^2 \exp(2i\beta_2 h) = 0\,, \tag{II.12}$$

where the effective reflection $r_{\text{eff}}^{(12)}$ is given by

$$r_{\text{eff}}^{(12)} = \frac{r_{22} + \alpha r_{11} r_{21} r_{12} \exp(2i\beta_1 h)}{1 - \alpha r_{21} r_{12} \exp\left[i(\beta_1 + \beta_2)h\right]}\,, \tag{II.13}$$

with $\alpha = \left[1 - r_{11}^2 \exp(2i\beta_1 h)\right]^{-1}$. The superscript $^{(12)}$ stands for the fact that $r_{\text{eff}}^{(12)}$ includes the multiple cross-reflections between BWs 1 and 2. Note that for $k_x = 0$, since $r_{12} = r_{21} = 0$, we recover $r_{\text{eff}}^{(12)} = r_{22}$. Details on the derivation of Eq. (II.12) can be found in the Appendix A.

We can thus apply the usual equations of a Fabry-Perot resonator provided that

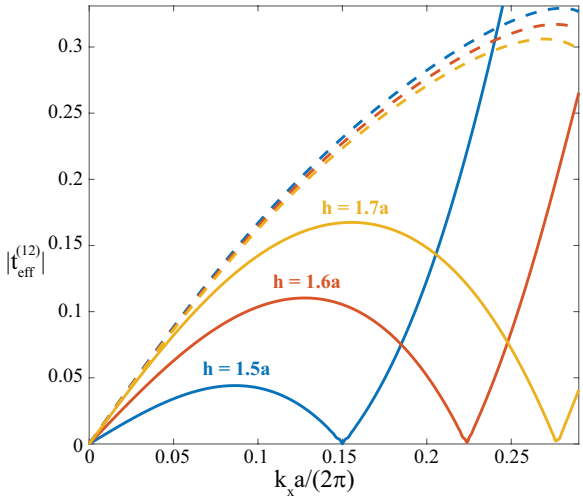

Figure II.4.: Effective transmission $t_{\text{eff}}^{(12)}$ (solid lines) for $N = 2$ propagative BWs in a 1D symmetric PhC slab with $F = 0.6$. The first cancellation of t_{eff} for $k_x = 0$ results from symmetry arguments. The second cancellation for $k_x \neq 0$ results from destructive interferences between both BWs and varies with the slab thickness. The frequency follows the dispersion curve of the leaky mode shown by the green curve in Fig. II.2(f). Dashed lines show the transmission coefficent t_2 alone and evidence the impact of the first BW on the radiative leakage.

$|r_{\text{eff}}^{(12)}|$ varies smoothly with the wavelength. The dispersion curve and the quality factor of a leaky mode composed of two BWs are given by Eqs. (II.7) and (II.8) by replacing β_1 and r_{11} by β_2 and $r_{\text{eff}}^{(12)}$. The amplitude of the radiated plane wave is now given by the superposition of both BWs, $A = t_1 u_1^+ \exp(i\beta_1 h) + t_2 u_2^+ \exp(i\beta_2 h)$. Similarly to the resonance condition, an effective transmission coefficient can be introduced,

$$A = t_{\text{eff}}^{(12)} u_2^+ \exp(i\beta_2 h)\,, \tag{II.14}$$

with

$$t_{\text{eff}}^{(12)} = t_2 + t_1 \alpha r_{21} e^{i\beta_1 h}\left[r_{\text{eff}}^{(12)} e^{i\beta_2 h} + r_{11} e^{i\beta_1 h}\right]. \tag{II.15}$$

Again, for $k_x = 0$, $t_{\text{eff}}^{(12)} = t_2$ since $r_{21} = 0$. One readily realises that the effective transmission can be cancelled if the second term in Eq. (II.15) is equal to $-t_2$. In that case, both BWs interfere destructively to cancel the overall leakage, leading to the formation of a BIC. Figure II.4 illustrates the interference mechanism as a

function of k_x for different values of the slab thickness. For $k_x = 0$, $t_{\text{eff}}^{(12)} = t_2 = 0$ for symmetry reasons. For $k_x \neq 0$, $t_{\text{eff}}^{(12)}$ is largely different from t_2 due to the impact of the first BW. The second cancellation of $t_{\text{eff}}^{(12)}$ is due to destructive interferences between both BWs. The slab thickness drives the phase difference between both BWs and the wave vector that corresponds to destructive interference increases with h.

The multimode Fabry-Perot model allows us to understand that the resonance-trapped BIC labelled (2) in Figs. II.2(f)-(h) is formed by the interference between the first and the second BW, with a dominant contribution from the second BW. This is because it has an antisymmetric field profile for $k_x = 0$ and a quasi-antisymmetric one for $k_x \neq 0$, which causes the BIC labelled (2) in Figs. II.2(f)-(h) to have a quasi-antisymmetric profile as well (see Fig. II.2(h) and Table II.1).

Note that Eqs (II.12)-(II.15) have been written in the case where the second BW is dominant over the first one. Conversely, when the first BW is dominant over the second one, we have $1 - r_{11}^2 \exp(2i\beta_1 h) \approx 0$ and the coefficient α becomes extremely large. Calculations are thus more stable if we keep the first BW and incorporate the second BW into the effective reflection. In that case, the subscripts 1 and 2 have simply to be inverted in Eqs. (II.12)-(II.13).

4.4 Transverse resonance for $N = 3$ waves

As the period-to-wavelength ratio is further increased, the third BW becomes propagative, see Fig. II.3(b). For $k_x = 0$ and $F = 0.6$, this corresponds to $a/\lambda > 0.45$. In that case, Eqs. (II.2) become a 6×6 system.

$$\begin{aligned}
u_1^+ &= r_{11}u_1^- \exp(i\beta_1 h) + r_{21}u_2^- \exp(i\beta_2 h) + r_{31}u_3^- \exp(i\beta_3 h),\\
u_1^- &= r_{11}u_1^+ \exp(i\beta_1 h) + r_{21}u_2^+ \exp(i\beta_2 h) + r_{31}u_3^+ \exp(i\beta_3 h)\\
u_2^+ &= r_{12}u_1^- \exp(i\beta_1 h) + r_{22}u_2^- \exp(i\beta_2 h) + r_{32}u_3^- \exp(i\beta_3 h),\\
u_2^- &= r_{12}u_1^+ \exp(i\beta_1 h) + r_{22}u_2^+ \exp(i\beta_2 h) + r_{32}u_3^+ \exp(i\beta_3 h)\\
u_3^+ &= r_{13}u_1^- \exp(i\beta_1 h) + r_{23}u_2^- \exp(i\beta_2 h) + r_{33}u_3^- \exp(i\beta_3 h),\\
u_3^- &= r_{13}u_1^+ \exp(i\beta_1 h) + r_{23}u_2^+ \exp(i\beta_2 h) + r_{33}u_3^+ \exp(i\beta_3 h).
\end{aligned} \tag{II.16}$$

Although more tedious, it is still possible to replace the complex interplay between the three BWs by effective reflection and transmission coefficients.

As for $N = 2$, let us start the discussion with the case $k_x = 0$. At the Γ-point, the first and third BWs have a symmetric field profile while the second BW is anti-

symmetric. The latter is thus decoupled from BWs 1 and 3. Even if three BWs are propagative, the leaky modes of the PhC slab are either formed by the second BW alone (symmetry-protected BIC) or by the interplay between first and third BWs. In that case, we can apply the results from previous section by introducing an effective reflection coefficient $r_{\text{eff}}^{(13)}$ instead of $r_{\text{eff}}^{(12)}$. Such a leaky mode formed by BWs 1 and 3 is a BIC if the interference leads to $|r_{\text{eff}}^{(13)}| = 1$ and $t_{\text{eff}}^{(13)} = 0$. This is the case of the blue mode labelled (5) in Figs. II.2(f)-(h).

For $k_x \neq 0$, the three BWs are coupled and we introduce an effective reflection coefficient $r_{\text{eff}}^{(123)}$, whose closed-form expression can be found below. Similarly to the $N = 2$ case, we keep the BW that has the most important contribution and incorporate the impact of the two other BWs inside the effective reflection. For a band with a symmetry-protected BIC at $k_x = 0$, the dominant BW is the second one; for a band without symmetry-protected BIC at $k_x = 0$, the dominant BW is usually the third one. In the latter case, the resonance condition given by Eq. (II.4) simply becomes

$$1 - \left(r_{\text{eff}}^{(123)}\right)^2 \exp(2i\beta_3 h) = 0\,, \tag{II.17}$$

where the effective reflection $r_{\text{eff}}^{(123)}$ is given by

$$r_{\text{eff}}^{(123)} \exp(i\beta_3 h) = \frac{r_{\text{eff}}^{(13)} \exp(i\beta_3 h) + R^{(23)}\Delta + \delta_{13}\gamma}{1 - R^{(23)}\gamma - \delta_{13}\Delta}, \tag{II.18}$$

with

$$\begin{aligned}
\Delta &= \alpha_{\text{eff}}^{(12)} R^{(32)} r_{\text{eff}}^{(12)} \exp(i\beta_2 h) + \alpha_{\text{eff}}^{(12)} \delta_{12}, && \text{(II.19)}\\
\gamma &= \alpha_{\text{eff}}^{(12)} \delta_{12} r_{\text{eff}}^{(12)} \exp(i\beta_2 h) + \alpha_{\text{eff}}^{(12)} R^{(32)}, && \text{(II.20)}\\
R^{(23)} &= \frac{r_{23} + \alpha r_{11} r_{13} r_{21} \exp(2i\beta_1 h)}{1 - \alpha r_{13} r_{31} \exp\left[i(\beta_1 + \beta_3)h\right]} \exp(i\beta_2 h), && \text{(II.21)}\\
\delta_{12} &= \frac{\alpha r_{12} r_{31} \exp\left[i(\beta_1 + \beta_3)h\right]}{1 - \alpha r_{12} r_{21} \exp\left[i(\beta_1 + \beta_2)h\right]}, && \text{(II.22)}\\
\alpha_{\text{eff}}^{(12)} &= \left[1 - \left(r_{\text{eff}}^{(12)}\right)^2 \exp(2i\beta_2 h)\right]^{-1}, && \text{(II.23)}\\
\alpha &= \left[1 - r_{11}^2 \exp(2i\beta_1 h)\right]^{-1}. && \text{(II.24)}
\end{aligned}$$

In these expressions, the coefficient $R^{(32)}$ has the same expression as $R^{(23)}$ but with indices 2 and 3 swapped. The coefficient δ_{13} can be deduced from δ_{12} by replacing the index 2 by 3. The effective reflection coefficients $r_{\text{eff}}^{(1j)}$ have the same expression

as in Eq. (II.13) with $j = 2, 3$:

$$r_{\text{eff}}^{(1j)} = \frac{r_{jj} + \alpha r_{11} r_{j1} r_{1j} \exp(2i\beta_1 h)}{1 - \alpha r_{j1} r_{1j} \exp\left[i(\beta_1 + \beta_j)h\right]} . \tag{II.25}$$

The details on the derivation of Eq. (II.18) can be found in Appendix A.

We can thus apply the usual equations of a Fabry-Perot resonator, provided that $|r_{\text{eff}}^{(123)}|$ varies smoothly with the wavelength. The dispersion curve and quality factor of a leaky mode composed of three BWs are given by Eqs. (II.7) and (II.8) by replacing β_1 and r_{11} by β_3 and $r_{\text{eff}}^{(123)}$.

The multimode Fabry-Perot model with $N = 3$ propagative BWs allows for the understanding of the formation of the symmetric resonance-trapped BICs at $k_x = 0$ and of the quasi-symmetric resonance-trapped BICs at $k_x \neq 0$ identified in Table II.1 and Figs. II.2(f)-(h). The first ones arise from the interference between two symmetric BWs, the first and third ones, which are not coupled to antisymmetric BWs at $k_x = 0$. The second ones are formed by the interference between three BWs (first, second, and third) with a dominant contribution from the third BW, whose field profiled is almost symmetric for $k_x \neq 0$.

Finally, the multimode Fabry-Perot model used either with $N = 2$ or $N = 3$ propagative BWs allows for the understanding of all four types of BICs observed in Fig. II.2 and summarised in Table II.1.

5 Model validation

To validate the multimode Fabry-Perot model, we consider the symmetric 1D PhC slab of Fig. II.2(e). We apply the model, either with $N = 2$ or $N = 3$ BWs, and calculate the dispersion curves and quality factors of the different leaky modes supported by the PhC slab. The model prediction for the dispersion curves and for the Q-factors (see Fig. II.5) are in quantitative agreement with the rigorous RCWA calculation, which takes into account a large number of evanescent BWs ($M = 30$). It is noteworthy that the semi-analytical model accurately predicts all four types of BICs supported by a 1D symmetric PhC slab, as summarised in Table II.1.

From a numerical point of view, the analyticity of the multimode Fabry-Perot model relies on Eqs. (II.7) and (II.8). In practice, one simply needs to calculate numerically with the RCWA the single-interface quantities defined in Fig. II.3 (β_i, r_{ii}, and r_{ij}) over the spectral range of interest. Then, one can apply Eq. (II.7) for any value of the slab thickness h to find analytically the eigenfrequencies λ_0 for a given

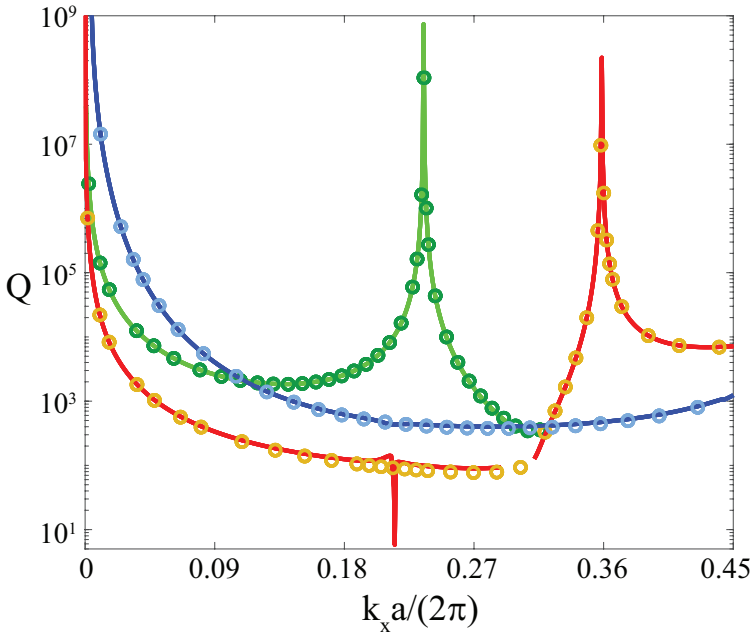

Figure II.5.: Quality factors of three leaky modes supported by a 1D symmetric PhC slab with $n_d = 3.5$, $F = 0.6$, and $h = 1.62a$, see Fig. II.2(e). The predictions of the multimode Fabry-Perot model (solid lines) are in excellent agreement with the exact calculations (markers). The model accurately reproduces the existence and positions of all four types of BICs. The discrepancies between the red curve and the yellow circles for $k_x \approx 0.215(2\pi/a)$ and $k_x \approx 0.3(2\pi/a)$ are explained in the text.

value of the integer p. Finally, Eq. (II.8) gives the corresponding quality factor with no further calculations. The model is therefore extremely efficient to investigate the dynamics of BICs with the slab thickness.

The model also provides some physical insight into the nature of the BICs, which before we could only qualitatively infer from the field profiles. The green mode in Fig. II.2(f) is mostly given by the second antisymmetric BW, with a small contribution of the fundamental BW for $k_x \neq 0$. To calculate it we used the phase matching condition Eq. (II.12) with $r_{\text{eff}}^{(12)}$ from Eq. (II.13). The blue mode in Fig. II.2(f) is dominated by the third BW with a small impact of the first and second BWs. For this mode, $r_{\text{eff}}^{(123)}$ with the phase factor $\exp(i\beta_3 h)$ was used, see Eq. (II.17).

We can also assert that the BIC labelled (5) in Fig. II.2(f) is fundamentally different from the ones labelled (1) and (3), which are also lying at the Γ-point. Indeed, it is a resonance-trapped BIC resulting from the destructive interference between the first and third BWs whereas BICs (1) and (3) are symmetry-protected BICs. Similarly,

the red leaky mode is also formed by three BWs. However, it couples with a different leaky mode around $k_x \approx 0.3(2\pi/a)$, see the anti-crossing between the red and black dispersion curves in Fig. II.2(f). Because of this coupling, the red leaky mode changes its symmetry from quasi-antisymmetric (for $k_x < 0.3(2\pi/a)$) to the quasi-symmetric (for $k_x > 0.3(2\pi/a)$), which is reflected in the BIC field profiles labelled (3) and (4) in Fig. II.2(h). In this case, different phase-matching equations have to be used for the left and right parts of the dispersion curve. Basically, indices 2 and 3 have to be interchanged in the expression of $r_{\text{eff}}^{(123)}$ and in the phase matching condition, to reflect the fact that on one side of the coupling region the second BW is dominant while on the other side the third BW is dominant. Then $r_{\text{eff}}^{(123)}$ becomes equal to r_{22} at $k_x = 0$ and gives rise to the symmetry-protected BIC labelled (3). In contrast, the other BIC at $k_x \approx 0.36(2\pi/a)$ stems from the interference of three BWs, the third (symmetric) being the dominant one.

This aspect of the model can be a source of erroneous results. The algebraic manipulations that lead to the definition of an effective reflection assume that some quantities (such as α^{-1} in Eq. (II.13)) are different from zero. As a consequence, some roots of the two-waves or three-waves resonance condition are not contained in the single-wave resonance condition given by Eqs. (II.12) and (II.17). The phase-matching condition gives thus a crossing of the dispersion curves instead of an anti-crossing. This is the reason why the model fails in Fig. II.5 for the red curve around $k_x \approx 0.3(2\pi/a)$. This point is further discussed in the following section.

Finally, we would like to clarify the obviously false feature of the red curve around $k_x \approx 0.215(2\pi/a)$. As mentioned in previous sections, the resonance condition and quality factor can be written in the form of Eqs. (II.7) and (II.8) only under the assumption that the modulus of the reflection coefficient varies smoothly with the wavelength. However, this assumption is not always valid when we deal with effective reflection coefficients. The appearance of an erroneous resonance in the dispersion curve predicted with the Fabry-Perot model (see the red solid curve in Fig. II.5) is due to this situation: $|r_{\text{eff}}^{(123)}|$ experiences a sudden resonance-like variation as a function of the wavelength (see Fig. II.7 of the ensuing section), which causes Eqs. (II.7) and (II.8) to lose their accuracy.

6 Limitations of the model

Coupling of two leaky modes manifests itself as an anti-crossing in the band diagram. When it occurs, two modes swap their symmetries: the branches of increasing

frequency with k_x are quasi-symmetric, while the ones of decreasing frequency are quasi-antisymmetric. Since the principal symmetry of a leaky mode is determined by the choice of the main BW, which is fixed, the model treats such anti-crossings, as crossings. In other words, as mentioned in the main text, since we approximate the system as a Fabry-Perot resonator with one mode and an effective reflection coefficient [2], we get a dispersion diagram of an unperturbed setup. Because the two modes have to maintain different symmetries, anti-crossings are only present above the third BW cut-off. An example is shown in Fig.II.6.

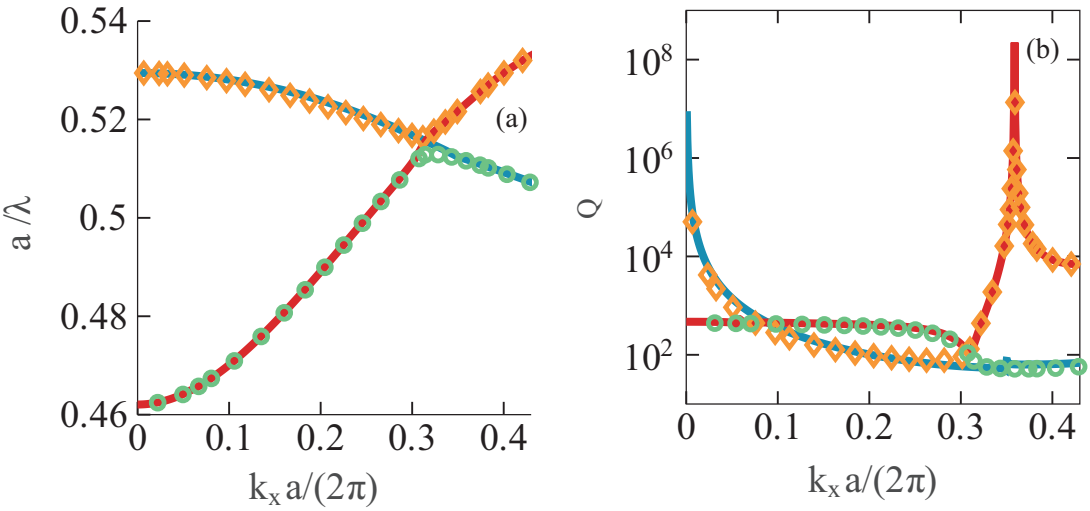

Figure II.6.: Demonstration of a limitation of the model. The dispersion (a) and quality factors (b) of two leaky modes that couple [the red one and one of the black ones in Figs. II.2(f,g)]. The solid lines are the outputs of the model, the circles and diamonds – the exact calculation. The modes coupling is not taken into account in the model and incorrect prediction is made in the vicinity of the anti-crossing.

Another erroneous feature of Fig. II.5 is the case when $|r_{\text{eff}}^{(123)}|$ varies rapidly with λ. Under this assumption we cannot safely rely on Eq. (II.7) for the phase-matching condition. Figure II.7 illustrates the point. There, we superimpose the curve, that corresponds to phase-matching condition of the form of Eq. (II.7) over the colour map of $|r_{\text{eff}}^{(123)}|$. The jump around $k_x = 0.215(2\pi/a)$ causes the incorrect Q-factor values (shown in Fig. II.5, red curve) and dispersion (black curve in Fig. II.7) around this point.

[2] Neglecting the evanescent Bloch waves does not break the coupling mechanism. The coupling mechanism is probably lost in the algebraic process of introducing an effective reflection coefficient. The latter is done by introducing several parameters (in particular, in the $N = 3$ case) whose denominator has to be non-zero.

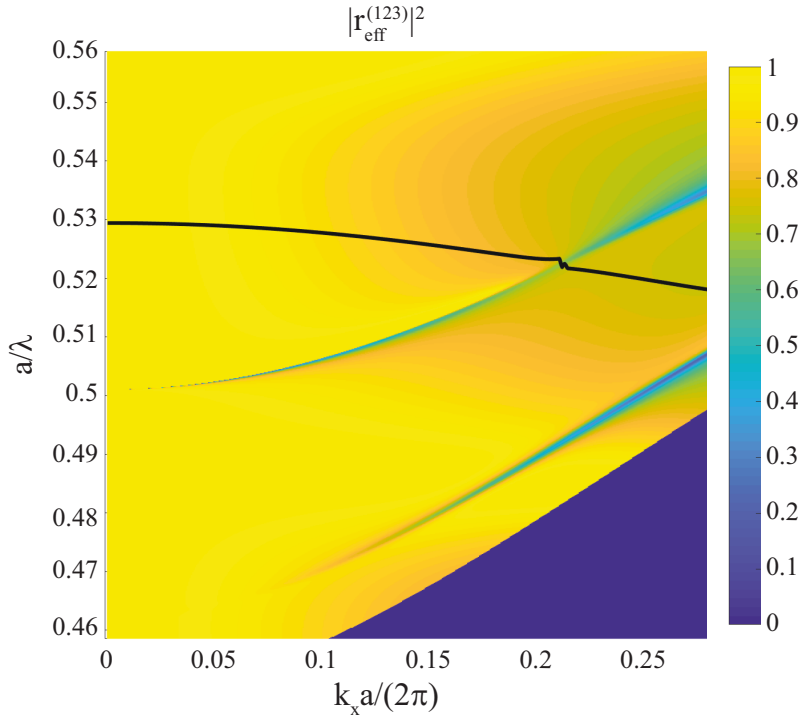

Figure II.7.: Square of the absolute value of $r_{\text{eff}}^{(123)}$. Black line indicates the phase matching condition (essentially the dispersion curve for the selected leaky mode). Around $k_x = 0.215(2\pi/a)$, it crosses a sharp variation of $r_{\text{eff}}^{(123)}$.

7 Dynamics of BICs with the slab thickness

Thanks to the analyticity of the model with respect to the slab thickness, it can be applied for a large number of h values to observe the dynamics of BICs with no additional RCWA calculations. In this section, we look at the evolution of BICs in PhC slabs as h is varied in three cases: (i) symmetric structure, (ii) broken horizontal symmetry, (iii) broken vertical symmetry (substrate).

7.1 Symmetric one-dimensional photonic crystal slabs

7.1.a Two propagating BWs regime

Figure II.8 shows the variation of the quality factor of a leaky mode of the PhC slab depicted in Fig. II.2(e), in the spectral range between the second and third BW cut-offs, as a function of the thickness h/a and the wave vector $k_x a/(2\pi)$. We have chosen to follow the dynamics of the mode represented with the green curve in

Fig. II.2(f)-(g).

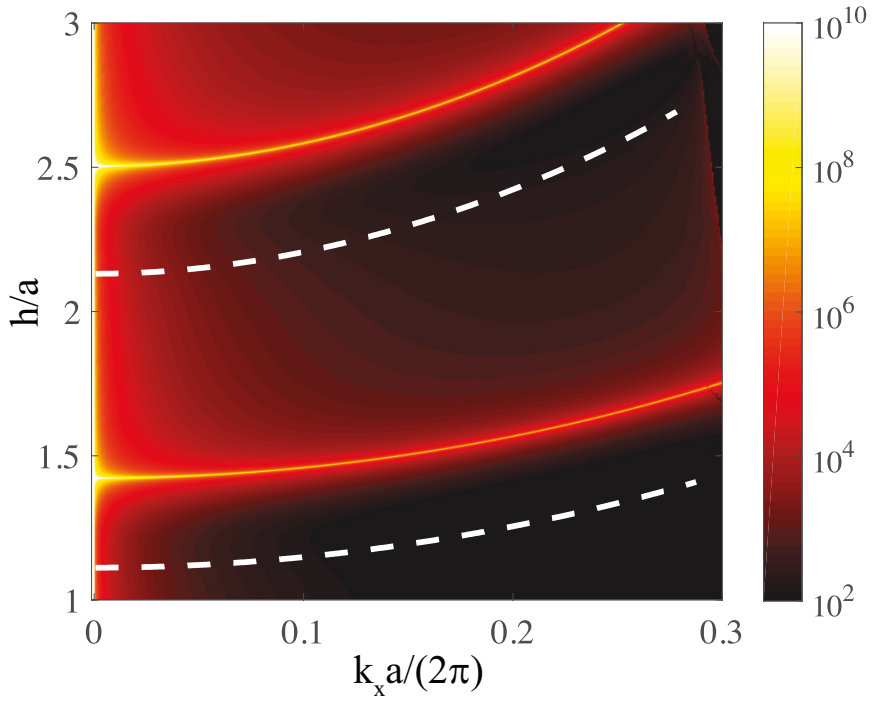

Figure II.8.: Quality factor (logarithmic scale) of the green leaky mode in Fig. II.2(f) as a function of h/a and $k_x a/(2\pi)$. The wavelength range specified during the calculations is such that only the first two BWs are propagating. The integer p from Eq. (II.7) is set to 1, which corresponds to the green line in Figs. II.2(f)-(g). Three branches (light yellow to white) showing an infinite Q-factor (BICs positions) are clearly visible. Dashed white lines indicate the positions two more such branches for $p = 0$, which correspond to a different leaky mode also formed by the first and second BWs.

We can clearly see three branches where $r_{\text{eff}}^{(12)}$ equals exactly 1, leading to an infinite Q-factor. The first branch is vertical at $k_x = 0$ and corresponds to the symmetry-protected BIC, which exists regardless of the value of h. The two other branches mark the (h, k_x) values for which the interference between the first and second BWs is perfectly destructive and results in the formation of a resonance-trapped BIC. The dashed lines show the positions of similar resonance-trapped BICs for $p = 0$ in Eq. (II.7). They belong to the dispersion curve of a different leaky mode.

7.1.b Three propagating BWs regime

Figure II.9(a) shows a colour map of the Q-factor for a leaky mode that consists of three propagative BWs. This figure demands a few more explanations and clarifica-

tions. Unlike Fig. II.8, here we do not see the Q-factor of a single selected leaky mode everywhere, rather, a different mode is confined between a pair of consecutive dashed blue lines. The lines themselves are the positions of the anti-crossings between the pairs of neighbouring modes. As explained in the previous section, this is a pitfall of the model. Depending on the BW that we choose to keep in the matrix $\mathbf{R}$, either number two or three, the model "looks for" a leaky mode with the same principal field symmetry, quasi-antisymmetric and quasi-symmetric, respectively. This causes it to treat anti-crossings as plain crossings. The values predicted before and after the anti-crossings are correct, but belong to different leaky modes. In the vicinity of the anti-crossing itself, where the dispersion curves experience a bend, it gives non-physical noisy-looking results.

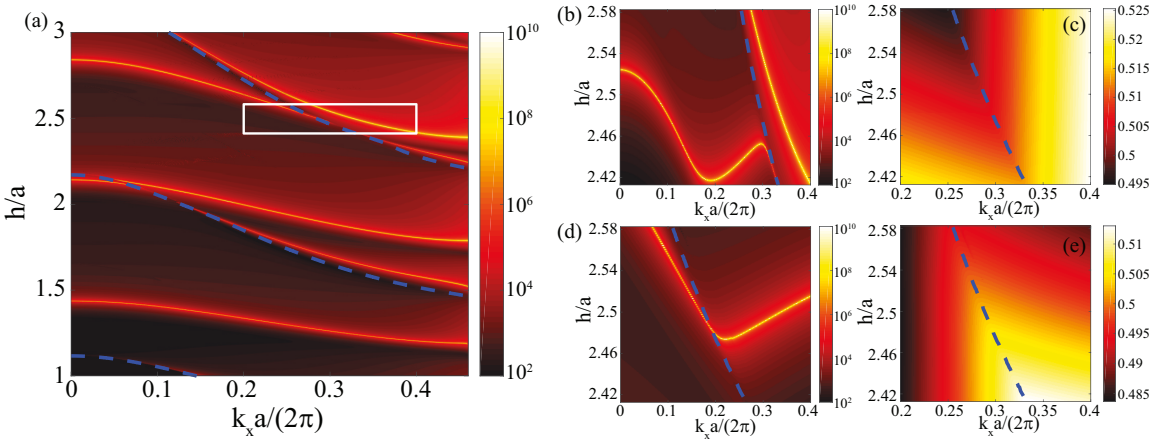

Figure II.9.: (a) Colour map of the Q-factor, calculated with the help of Eq. (II.18). Dashed blue lines indicate the position of anti-crossings in the dispersion diagram. The Q-factors immediately to the left and right of these curves belong to two different leaky modes. The white box indicates the region of the (k_x, h) space that we look closer into in (c-e). (b), (c) Q-factor and a/λ ratio (normalised frequency), respectively, for one mode that is coupled [the one to the right in the box]. Similarly, (d), (e) – Q and dispersion of the other [the one to the left in the box]. Note that the horizontal axis of (b) and (d) is different from those of (c) and (e).

To further investigate this issue, we zoom in to a smaller region in the (k_x, h) space, traced with a white box in Fig. II.9(a). Figures II.9(b,c) display the Q-factor and dispersion, respectively, of the leaky mode in the right part of the box (above the anti-crossing line) in Fig. II.9(a). Similarly, the other mode occupies Figs. II.9(d,e).

The mode in Fig.II.9(b,c) has the quasi-antisymmetric field profile to the left of

the anti-crossing line, and quasi-symmetric to the right. Vice versa for the mode in Fig.II.9(d,e). A couple of interesting observations can be made. Firstly, as can be seen in Fig.II.9(b) we could have four BICs due to a single mode when $h/a \in (2.42, 2.45)$ at different k_x and λ. Secondly, the diverging Q-factor curve displays one or multiple bends. If we were to plot several Q-factor curves, increasing h, past the point of the bend, we would register an "annihilation" of the BICs – two BICs coming closer to each other on the k_x axis until they "collide" and none is present any longer, as previously reported in Ref. [146], where the parameter that had been gradually changed was the refractive index of the surrounding space. This point is also illustrated in Fig. II.4, where the zero of $|t_{eff}^{(12)}|$ is moving toward the light line cut-off with h. The parameter region in the vicinity of the bend possesses extremely high Q's for a range of optogeometric parameters, which might be appealing for practical realisations and applications.

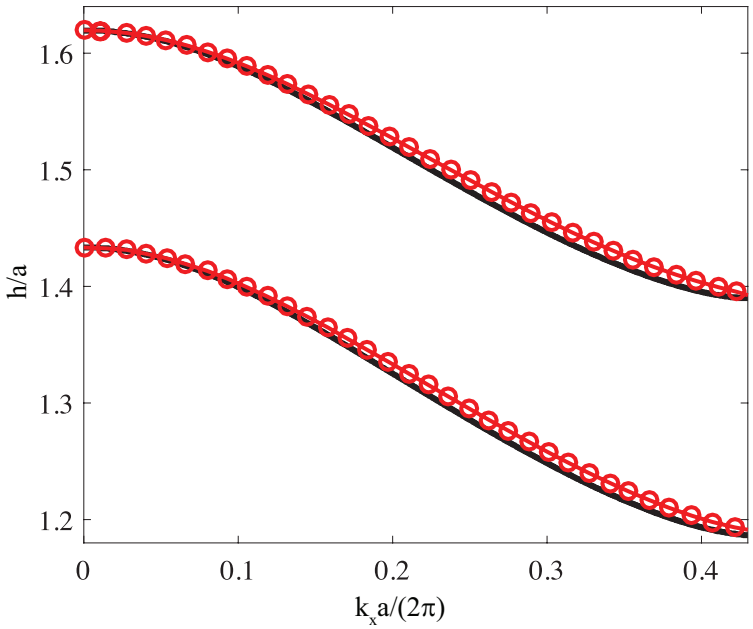

Figure II.10.: Position of two BICs, as a function of $k_x a/(2\pi)$ and h/a. Black lines were obtained using the model only with the first two symmetric BWs (number one and three) that have the major contribution. Red circles – exact calculation, connected with a red line, acting as a guide to an eye.

Ever so slight perturbation by a BW of a different symmetry is crucial to get the correct Q-factor values. However, their position and the dispersion curves are less sensitive. To qualitatively illustrate this point, on Fig. II.10 we plot the dynamics of two resonance-trapped BICs that consist of three BWs versus h/a and $k_x a/(2\pi)$.

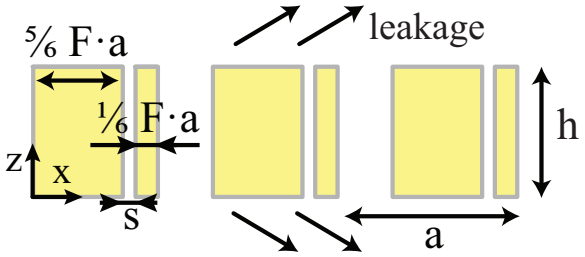

Figure II.11.: Schematics of the asymmetric 1D PhC slab. The newly introduced parameter for the asymmetric PhC slab is a slit of width s (no asymmetry for $s = 0$) that divides the dielectric ridge into a bigger and smaller part of size $5/6Fa$ and $1/6Fa$, respectively, preserving the total filling factor of material used throughout this chapter, $F = 0.6$

Black solid curves are the predictions of the model, with the second BW deliberately excluded,[3] while red circles were obtained with the exact calculation. Other parameters of the PhC slab are the same as in Fig. II.2. As can be seen, h (and therefore λ_0) that produce a BIC can be predicted reasonably well, even though the PhC modes are considered as purely symmetric, and the value of the Q-factor is completely off.

7.2 Asymmetric one-dimensional photonic crystal slabs

In this subsection, we use the multimode Fabry-Perot model to study the behaviour of BICs under broken mirror symmetry. We consider a 1D PhC slab with a vertical mirror symmetry but no horizontal mirror symmetry as depicted in Fig. II.11. The asymmetry parameter s is the size of the air gap that divides the dielectric ridge into a bigger and a smaller part of size $5/6Fa$ and $1/6Fa$, respectively. Note that the total filling factor in dielectric material is preserved, $F = 0.6$. Recently, a study of a PhC slab with a slot in different positions for a fixed thickness and normal incidence angle has been published [145]. We evidence that symmetry-protected BICs, which exist in symmetric structures at the Γ-point of the dispersion diagram, become resonance-trapped ones when the horizontal mirror symmetry is broken, but only for specific values of the slab thickness.

Figure II.12 shows the variation of the Q-factor of a leaky mode in different situations. In Fig. II.12(a) we plot Q as a function of the slab thickness h and the asymmetry parameter s for a fixed $k_x = 0$ in a spectral range where only two BWs

[3] In this case, we do not see a sharp infinite-Q resonances, but broad and finite ones. Black solid lines in Fig. II.10 simply trace their maxima.

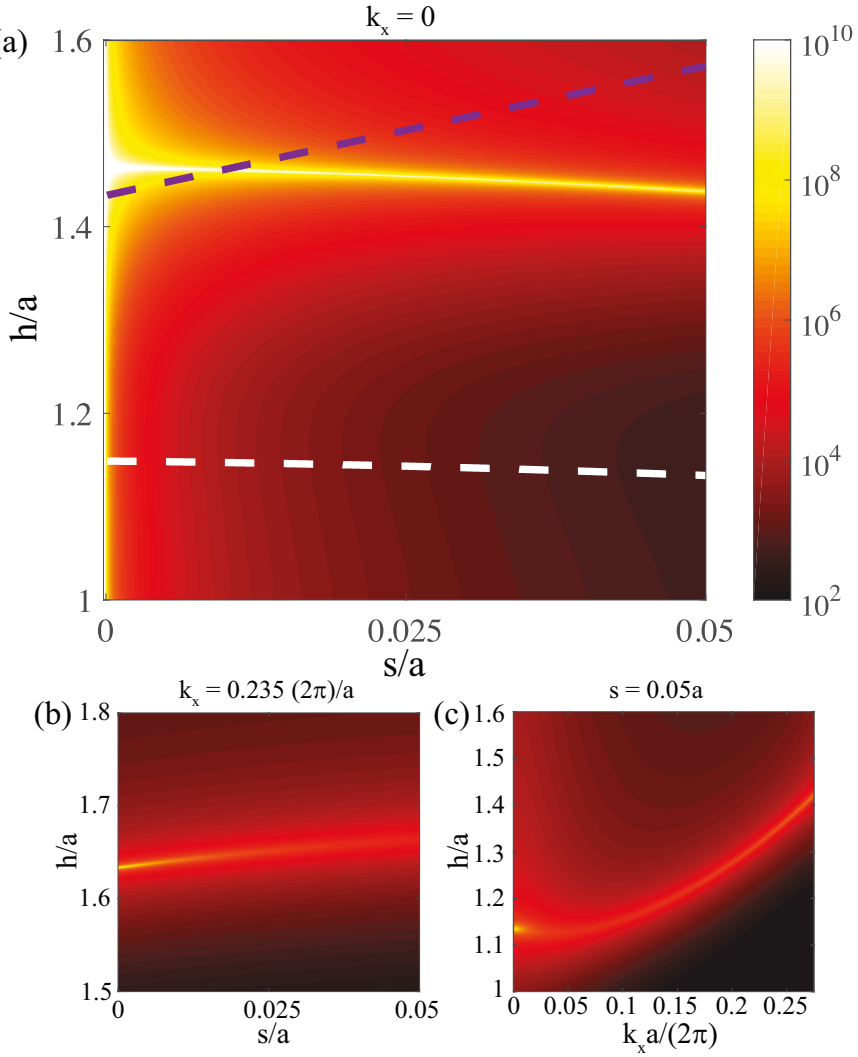

Figure II.12.: Quality factor (logarithmic scale) for the asymmetric PhC slab with two propagative BWs. (a) Q-factor as a function of the slab thickness h/a and the asymmetry parameter s/a for $k_x = 0$. The leaky mode is calculated with $p = 1$ in Eq. (II.7). A BIC (diverging quality factor) is clearly visible whatever the value of the asymmetry parameter. It is a symmetry-protected BIC for $s = 0$ ($r_{12} = 0$ and $|r_{22}| = 1$) but a resonance-trapped BIC for $s \neq 0$ ($r_{12} \neq 0$, $|r_{22}| < 1$, and $|r_{\text{eff}}^{(12)}| = 1$). The dashed white line indicates the position of a similar BIC for $p = 0$ and the dashed magenta line indicates the position of a BIC formed by three BWs with $p = 0$. (b) Same as (a), but for $k_x \approx 0.235(2\pi/a)$. (c) Q-factor as a function of h/a and $k_x a/(2\pi)$ for $s = 0.05a$. Colour scale and other optogeometric parameters are the same for all three subfigures.

are propagative. We readily observe two branches that correspond to a diverging Q, and thus a BIC. The vertical branch for $s = 0$ signifies a symmetry-protected BIC. As the horizontal symmetry is broken ($s \neq 0$), the symmetry-protected BIC cannot exist anymore. Nevertheless, for specific values of the pair (h, s), it becomes a resonance-trapped BIC, as evidenced by the second white branch in Fig. II.12. Under the broken symmetry, r_{12} no longer vanishes for $k_x = 0$, which allows us to observe this trajectory of a resonance-trapped BIC.

Figure II.12(b) displays the Q-factor as a function of h and s for $k_x \neq 0$. In that case, a BIC can only exist in symmetric structures for $s = 0$; it is the resonance-trapped BIC labelled (2) in Fig. II.2(f). This BIC disappears ($Q < 10^9$) when the symmetry is broken. Lastly, Fig. II.12(c) displays the Q-factor of the same leaky mode as a function of h and k_x with a fixed asymmetry parameter $s = 0.05a$. A resonance-trapped BIC exists for $k_x = 0$ [the one shown in Fig. II.12(a)] and disappears for $k \neq 0$.

To sum up, resonance-trapped BICs can exist in asymmetric 1D PhC slabs with a broken horizontal symmetry, but only for $k_x = 0$.

7.3 Case of a substrate: broken vertical symmetry

Finally, let us consider a symmetric PhC slab on a substrate. The substrate can either have a finite thickness or be considered infinite. Such a case of broken vertical symmetry means that the reflection coefficients of the BWs, and thus the effective quantities as well, have to be calculated separately for the upper and lower interfaces [33]. The factor $|r_{\text{eff}}^{(12)}|^2$ in Eq. II.12 has to be substituted with $|r_{\text{eff}}^{(12),T} r_{\text{eff}}^{(12),B}|$, where superscripts T and B stand for top and bottom interfaces, respectively. Two different RCWA problems between a semi-infinite periodic medium and a semi-infinite homogeneous medium [see Fig. II.3(a)] with dissimilar refractive indices of the homogeneous space region have to be solved. Note that the coefficients $r_{\text{eff}}^{(12),T}$ and $r_{\text{eff}}^{(12),B}$ do not contain the reflection coefficients of their respective interface exclusively (see Appendix A for their expressions).

Figure II.13(a) confirms the fact that has been already understood that no resonance-trapped BICs are possible in this case [139, 163], while the Q-factor for $k_x = 0$ still goes to infinity (symmetry-protected BIC). We note that the location of the maximum has shifted slightly in terms of h and λ (assuming k_x is fixed) and that the resonance has also become broader, but the Q-factor still reaches extremely huge values around 10^6.

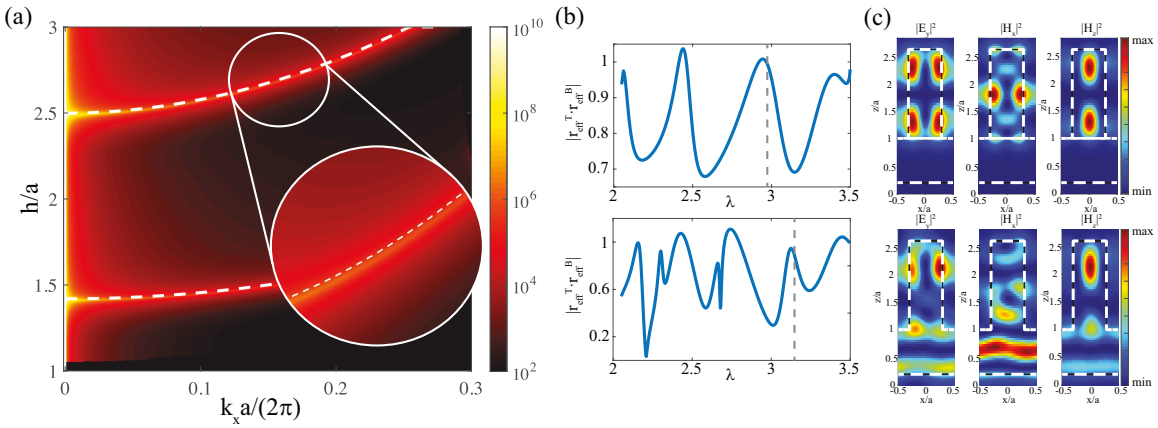

Figure II.13.: (a) Same as Fig. II.8, but with the refractive index $n = 1.45$ of the semi-infinite homogeneous space on one side of the slab, and $n = 1$ on the other. Dashed lines in (a) indicate the infinite Q branches location in the case when the PhC slab is in the air, i.e. the two branches in Fig. II.8. (b) The spectra of $|r_{\text{eff}}^{(12),T} r_{\text{eff}}^{(12),B}|$ for a PhC slab ($h = 1.6a$) lying on a substrate of thickness $0.8a$ with the refractive index $n = 1.5$ and $n = 3.5$ (same as the slab) for top and bottom, respectively; $k_x = 0.23(2\pi/a)$. (c) Field profiles of the PhC modes that are excited in the corresponding (top and bottom) configurations. Their wavelengths are marked with dashed lines in (b). White lines trace the border of the refractive index contrast. The wavelength range is such that only two Bloch waves are propagative.

It worth mentioning that a substrate of a particular thickness and refractive index may introduce a large number of new resonances and reflections, which can result in the appearance of a resonance-trapped BIC [148, 164]. These resonances will, in turn, bring sharp features to $|r_{\text{eff}}^{(12),B}|$, rendering the model unusable by violating the conditions for phase-matching [Eq. (II.7)]. This point is illustrated in Fig. II.13(b,c). In the case when no guided modes are excited in the substrate (top row), both effective reflection coefficients vary smoothly, allowing for a phase-matching in the form of Eq. (II.7). If, however, the refractive index contrast is removed (bottom row), or, alternatively, thickness or wavelength might be modified, we observe sharp resonances in the spectrum of $|r_{\text{eff}}^{(12),T} r_{\text{eff}}^{(12),B}|$, due to the guided mode excitation, which requires Eq. (II.12) to be solved numerically for complex $\tilde{\lambda}$, which would obviously negate its semi-analytical nature.

From our calculations it appears that two BW in the weak coupling regime with the substrate are not sufficient to produce the required destructive interference for

an accidental BIC. We note, however, that a resonance-trapped BICs was recently revealed in a high-contrast PhC slab with an index-matched substrate of a finite thickness, under the conditions of three propagating BWs [148].

8 Conclusion

To sum up, in this chapter we have used a multimode Fabry-Perot model to calculate the dispersion curves and the quality factors of leaky modes supported by 1D symmetric and asymmetric PhC slabs. Leaky modes are transverse Fabry-Perot resonances composed of a few propagative BWs bouncing back and forth vertically inside the slab. This multimode Fabry-Perot model, which does not rely on a perturbative approach, accurately predicts the existence of BICs and their positions in the parameter space regardless of the refractive index contrast. The model equally applies to symmetry-protected BICs (absence of leakage is due to symmetry incompatibility between a single BW composing the mode and the radiative plane waves) and resonance-trapped BICs (radiative leakage accidentally disappears because the contributions of several BWs interfere destructively).

The multimode Fabry-Perot model allows us to show that, regardless of the slab thickness, BICs cannot exist below a cut-off frequency, which is related to the existence of the second-order BW in the PhC. In other words, BICs cannot exist in the homogenisation regime. Thanks to the semi-analyticity of the model, we investigate the dynamics of BICs with the slab thickness in symmetric and asymmetric photonic crystal slabs. Our calculations show that resonance-trapped BICs can exist in asymmetric 1D PhC slabs with a broken horizontal symmetry, but only for $k_x = 0$. We evidence that the symmetry-protected BICs that exist in symmetric structures at the Γ-point of the dispersion diagram can still exist when the horizontal mirror symmetry is broken, but only for specific values of the slab thickness.

Since the multimode Fabry-Perot model yields fast yet accurate predictions of the BIC location in the parameter space and provides a better understanding of the physical mechanisms that lead to the BIC formation, we think that it can become an important tool for designing PhC devices relying on the existence of a BIC. The model can also be applied to 1D PhC slabs in TM polarisation and to 2D PhC slabs.

Chapter III

Modal expansion of T-matrix with quasi-normal modes

A powerful and widespread mathematical tool for representing light scattering by an arbitrary-shaped object is the System Transfer (or Transition) Operator approach, usually shortened to the T-matrix approach [165, 166]. It defines an operator **T** that relates linearly the incident field to the scattered field. It is intrinsic to the scatterer and captures all the complexity of the object. Once the T-matrix has been determined, it can be used with any excitation field to calculate the corresponding scattered field. Most importantly, the T-matrix can be used to calculate the optical response of an ensemble of scatterers, be it an aggregation of a finite number of objects or a periodic arrangement. Indeed, multiple scattering between several scatterers can be efficiently calculated from the sole knowledge of the individual T-matrices of each object (as we explore in Chapter IV) [167]. The scatterers can be located in a homogeneous environment or inside a stratified medium [115]. This rigorous semi-analytical method to compute multiple scattering by arbitrary-shaped objects is often referred to as the T-matrix method or the multipole method [112–114, 168].

In the process of calculating multiple scattering by an ensemble of scatterers with the T-matrix approach, the difficult part is the computation of the T-matrix of a single object. For spherical scatterers (homogeneous or core-shell spheres), the T-matrix is diagonal and can be analytically calculated from Mie theory [107]. However, for non-spherical objects, the form of the T-matrix is more complex and one has to rely on numerical calculations. Earlier works have used the Null-Field Method (also known as the Extended Boundary Condition Method) to compute the T-matrix [165]. A huge bulk of literature is devoted to this approach (see, for instance, a substantial reference database in [169] and later updates). However, the null-field method can only be applied to calculate the scattering by homogeneous objects. Moreover, since it is not based on a rigorous solution of Maxwell's equations everywhere inside the scatterer, the accuracy and stability of the null-field method are questionable for scatterers with a large aspect ratio. Combining the null-field method with discrete sources has been proposed to improve the calculation of objects with a large aspect

ratio [168, 170]. However, this extension of the null-field method suffers from similar limitations: the scattering problem is not solved rigorously everywhere inside the scatterer. Recent works have proposed to use the well-established Finite Element Method (FEM) to compute the T-matrix [171, 172]. This solution has the advantage to be rigorous and applicable to arbitrary-shaped and inhomogeneous scatterers. Its main limitation is a heavy numerical burden for three-dimensional objects with a complex geometry since numerous rigorous calculations of the scattered field have to be performed for different incident fields to get the full T-matrix.

In this chapter, we develop an original approach for a fast and accurate calculation of the T-matrix of a single resonant scatterer. Our approach is based on recent developments on modal theories for nanoresonators [173]. We apply a powerful technique, called quasi-normal mode (QNM) expansion (or resonant-state expansion), to calculate the electromagnetic field scattered by a resonant scatterer. After a projection of the modal expansion on the Vector Spherical Harmonics (VSHs, sometimes also referred to as vector partial waves or vector spherical waves) basis, we obtain the T-matrix. In contrast to previous works that have used QNM expansions to study light scattering by isolated resonant scatterers [156, 174, 175] or by periodic arrays of resonant scatterers [174, 176], we do not simply calculate observables such as cross-section, reflection, or transmission. We recover the full T-matrix, which can be used in a second step as a building block to solve any scattering problem involving the considered scatterer, be it alone or inside a more complex ensemble. During the preparation of this thesis, a QNM expansion of the T-matrix based on Mie theory has been proposed for lossless and dispersionless dielectric spheres [177]. Since our approach relies on a more general formalism, the modal decomposition of the T-matrix that we have developed can be applied to arbitrary-shaped objects composed of dispersive and absorptive materials.

The main advantages of using a modal formalism are: (i) it introduces semi-analyticity to the computation and (ii) it brings some physical insight into the nature and interference of the scatterer's resonances. By combining these two techniques (T-matrix and modal expansion), we aim at transmitting these advantages into the calculation of light scattering by an ensemble of resonant scatterers. Our approach should make it possible to study how the resonances of an individual nanoresonator translate into the collective response of a periodic or non-periodic arrangement of these resonators.

We introduce in Sec. III.1 the theoretical concepts used to derive a modal expansion of the T-matrix. Subsection III.1.1 is devoted to a brief presentation of the T-matrix.

We first define the T-matrix and then we show that it can be evaluated from a calculation of the scattered field either over a closed surface outside the scatterer or inside the volume of the scatterer. In Subsec. III.1.2, we review recent results on quasi-normal mode expansion that we use in Sec. III.2 to derive a modal expansion of the T-matrix. We evidence that two different formulations of the modal expansion can be derived. Finally, we validate our modal approach in Sec. III.3 by considering the test case of a metallic nanosphere. We show that if both QNM expansions of the T-matrix provide accurate results for a large number of modes, they do not converge with the same speed as the number of modes is increased. Our results show that only one formulation guarantees a good accuracy of the modal expansion for a small number of modes.

1 Theoretical introduction

We review in this section the theoretical concepts used for the derivation of a modal expansion of the T-matrix. First of all, we briefly recall the definition of the T-matrix and the different methods that can be used to calculate it. As a second step, we present the main ingredients of the quasi-normal mode theory.

1.1 T-matrix: Definition and calculation

The T-matrix method was formally introduced by Waterman in 1965 [165], further developed in the 1970s [167, 178, 179], and then extended by numerous works, see for instance [169, 180, 181] and references therein. Within this formalism, the incident and scattered time-harmonic electromagnetic fields are expanded in the basis of VSHs. The linear relation between the respective expansion coefficients is provided by the T-matrix. This concept is general and has been applied to individual scatterers, their clusters and ensembles, as well as separate parts of composites [169, 181].

In a nutshell, T-matrix coefficients are the projections onto the VSHs basis of the fields scattered by the object illuminated by each VSH. We present in Subsec. 1.1.a a brief definition of the T-matrix and show in Subsec. 1.1.b that there are two equivalent possibilities to evaluate the projection of the scattered field. Indeed, the projection onto the VSHs basis can be evaluated either from a calculation of the scattered field over a closed surface outside the scatterer or from a calculation of the total field inside the volume of the scatterer.

1.1.a Definition of the T-matrix

Let us consider an inhomogeneous object with an arbitrary shape located in a homogeneous medium of refractive index n_b, see Fig. III.1. The object is illuminated by an incident electromagnetic field $\mathbf{\Psi}_{\text{inc}} = (\mathbf{E}_{\text{inc}}, \mathbf{H}_{\text{inc}})$ and the scattering process gives rise to a scattered field $\mathbf{\Psi}_s = (\mathbf{E}_{\text{s}}, \mathbf{H}_{\text{s}})$. The total field is $(\mathbf{E}, \mathbf{H}) = (\mathbf{E}_{\text{inc}}, \mathbf{H}_{\text{inc}}) + (\mathbf{E}_{\text{s}}, \mathbf{H}_{\text{s}})$. Since VSHs are solutions of Maxwell's equations (expressed in spherical coordinates) in a homogeneous medium, they form a convenient basis that can be used to express both incident and scattered field outside a circumscribing sphere Σ, see Fig. III.1.

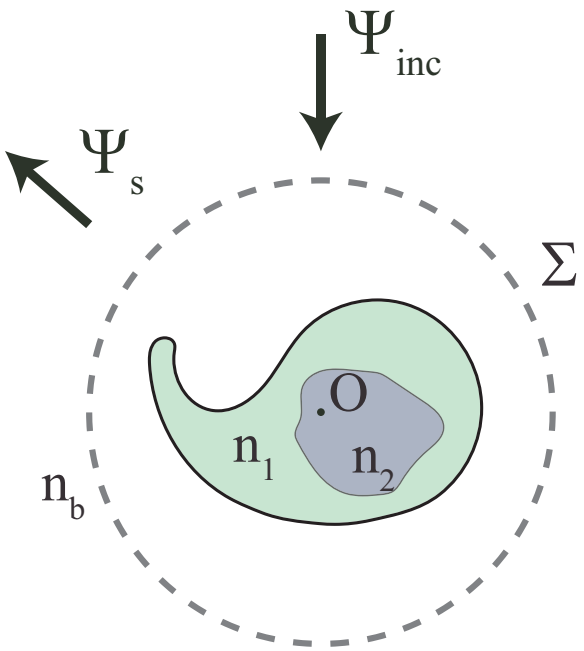

Figure III.1.: Schematic of the problem. The E- and H-fields are collectively denoted as $\mathbf{\Psi} = (\mathbf{E}, \mathbf{H})$. An incident field is illuminating an object of arbitrary shape within a homogeneous environment characterised by the refractive index n_b, producing a scattered field. An imaginary sphere Σ that includes the entire scatterer with the centre in O is traced with a dashed line.

Regular VSHs, denoted as $\text{Rg}\mathbf{M}_{mn}$ and $\text{Rg}\mathbf{N}_{mn}$ for magnetic and electric waves, respectively, serve as a basis for the incident field. On the other hand, the scattered field can be decomposed into outgoing VSHs, labelled as $\mathbf{M}_{mn}^{(+)}$ and $\mathbf{N}_{mn}^{(+)}$. We expand the incident and scattered fields in VSH (or multipole expansion) as follows [166, 182]:

$$\mathbf{E}_{\text{inc}}(\mathbf{r}) = \sum_{n=1}^{\infty}\sum_{m=-n}^{n}\left[a_{mn}\text{Rg}\mathbf{M}_{mn}(k\mathbf{r}) + b_{mn}\text{Rg}\mathbf{N}_{mn}(k\mathbf{r})\right], \tag{III.1}$$

$$\mathbf{E}_{\text{s}}(\mathbf{r}) = \sum_{n=1}^{\infty}\sum_{m=-n}^{n}\left[p_{mn}\mathbf{M}^{(+)}_{mn}(k\mathbf{r}) + q_{mn}\mathbf{N}^{(+)}_{mn}(k\mathbf{r})\right], \tag{III.2}$$

where $k = k_0 n_b = 2\pi/\lambda n_b$, $\mathbf{r}$ is the space coordinate vector, n is the VSH degree ($n = 1$ corresponds to dipolar terms), and $m \in [-n, n]$ is the azimuthal number. The coordinate origin is the centre of a virtual sphere, which circumscribes the resonator as shown in Fig. III.1. The detailed expressions of the regular and outgoing VSHs are given in Appendix B.

For the sake of convenience, we adopt a more compact notation, which is adapted from the one used in [166]. We introduce a single index L that gathers the indices n and m, as well as the polarisation label (electric or magnetic), as defined in Table III.1. Since we have chosen to combine both electric and magnetic VSHs into the new index L, we have to introduce a new notation for the VSHs. As detailed in Table III.1, we denote the outgoing (resp. incoming) electric and magnetic VSHs $\mathbf{N}^{(+)}_{mn}$ and $\mathbf{M}^{(+)}_{mn}$ (resp. $\mathbf{N}^{(-)}_{mn}$ and $\mathbf{M}^{(-)}_{mn}$) as $\mathbf{\Xi}^{(+)}_L$ (resp. $\mathbf{\Xi}^{(-)}_L$). Regular VSHs are denoted by ξ_L. Odd values of the index L correspond to magnetic VSHs while even values correspond to electric VSHs.

With the notation in Table III.1, Eqs. (III.1) and (III.2) can be rewritten in a compact form as

$$\mathbf{E}_{inc}(\mathbf{r}) = \sum_{L=1}^{\infty} a_L \xi_L(k\mathbf{r}), \tag{III.3}$$

$$\mathbf{E}_{\text{s}}(\mathbf{r}) = \sum_{L=1}^{\infty} p_L \mathbf{\Xi}^{(+)}_L(k\mathbf{r}). \tag{III.4}$$

The outgoing and incoming VSHs, $\mathbf{\Xi}^{(+)}_L$ and $\mathbf{\Xi}^{(-)}_L$, are singular at the origin $\mathbf{r} = 0$. The regular VSHs ξ_L are defined as the half-sum of incoming and outgoing VSHs,

$$\xi_L = \frac{\mathbf{\Xi}^{(-)}_L + \mathbf{\Xi}^{(+)}_L}{2}. \tag{III.5}$$

These are regular (non-singular) functions at the origin. Note that, in the following, the notations $\mathbf{\Xi}^{(\pm)}_L$ and ξ_L will be used indifferently for an electric field $\mathbf{E}$ or for a pair $(\mathbf{E}, \mathbf{H})$. The presence or absence of other magnetic fields in the equations lifts possible ambiguities.

Combined index L	1	2	3	4	5
n	1	1	1	1	1
m	-1	-1	0	0	1
Polarisation	magn.	elec.	magn.	elec.	magn.
$\boldsymbol{\Xi}_L^{(\pm)}$	$\mathbf{M}_{1,-1}^{(\pm)}$	$\mathbf{N}_{1,-1}^{(\pm)}$	$\mathbf{M}_{1,0}^{(\pm)}$	$\mathbf{N}_{1,0}^{(\pm)}$	$\mathbf{M}_{1,1}^{(\pm)}$
ξ_L	$\mathrm{Rg}\mathbf{M}_{1,-1}$	$\mathrm{Rg}\mathbf{N}_{1,-1}$	$\mathrm{Rg}\mathbf{M}_{1,0}$	$\mathrm{Rg}\mathbf{N}_{1,0}$	$\mathrm{Rg}\mathbf{M}_{1,1}$
Combined index L	6	7	8	9	10
n	1	2	2	2	2
m	1	-2	-2	-1	-1
Polarisation	elec.	magn.	elec.	magn.	elec.
$\boldsymbol{\Xi}_L^{(\pm)}$	$\mathbf{N}_{1,1}^{(\pm)}$	$\mathbf{M}_{2,-2}^{(\pm)}$	$\mathbf{N}_{2,-2}^{(\pm)}$	$\mathbf{M}_{2,-1}^{(\pm)}$	$\mathbf{N}_{2,-1}^{(\pm)}$
ξ_L	$\mathrm{Rg}\mathbf{N}_{1,1}$	$\mathrm{Rg}\mathbf{M}_{2,-2}$	$\mathrm{Rg}\mathbf{N}_{2,-2}$	$\mathrm{Rg}\mathbf{M}_{2,-1}$	$\mathrm{Rg}\mathbf{N}_{2,-1}^{(\pm)}$

Table III.1.: Definition of a combined index L that gathers the VSH degree n, the azimuthal number $m \in [-n, n]$, and the electric/magnetic polarisation. Since we have chosen to combine both electric and magnetic VSHs into the new index L, we introduce also a combined notation for the VSHs, $\boldsymbol{\Xi}_L^{(\pm)}$ for outgoing/incoming VSHs and ξ_L for regular VSH.

In any scattering problem, the expansion coefficients for $\mathbf{E}_{\mathrm{s}}(\mathbf{r})$, the p_L's, are the unknowns to be determined from their counterparts for $\mathbf{E}_{inc}(\mathbf{r})$, the a_L's, which are known. They are linearly related through the T-matrix as follows

$$p_L = \sum_{K=1}^{\infty} T_{LK} a_K \,, \tag{III.6}$$

or in the matrix notation

$$\left[\mathrm{p}\right] = \mathbf{T} \left[\mathrm{a}\right], \tag{III.7}$$

where [a] and [p] are the column vectors formed by the expansion coefficients a_L and p_L of the incident and scattered in the VSH basis.

The key feature of the T-matrix is that its elements T_{LK} are independent of the incident field. They depend only on the permittivity and permeability distributions inside the circumscribing sphere, i.e., on the geometry of the scatterer, on the permittivity and permeability distributions inside the scatterer, and on the refractive index of the surrounding medium, as well as on the scatterer orientation with respect to the coordinate system. Once the T-matrix is known for a given orientation of the scattering object, another T-matrix for any rotation of the scatterer can be deduced analytically [180]. As a result, once the T-matrix corresponding to one scat-

terer in a given homogeneous medium is known, we are able to calculate analytically the scattering for any incident field, any scatterer orientation, and any assembly of this scatterer, as long as the incident field is represented in the basis formed by the regular VSHs. It is noteworthy that the T-matrix method is not limited to a homogeneous environment. It can also be used to calculate light scattering by scatterers in a stratified medium [115].

Let us finally briefly comment on the limitations of the T-matrix applicability to multiple scattering by an ensemble of objects. Within this framework of VSH expansion, it is impossible to obtain the total field distribution inside the scatterer, or anywhere within the circumscribing sphere, except, of course, for spherical objects. This is the origin for the two main limitations of the T-matrix approach: (i) it cannot be used to calculate the multiple scattering by elongated objects separated by a distance smaller than the largest dimension of the scatterers and (ii) it cannot be used for an object close to an interface. These two cases are schematically depicted in Fig. III.2.

1.1.b Calculation of the T-matrix

In the first presentation of the System Transfer Operator approach [165], the T-matrix was calculated with the so-called Null-Field Method (or Extended Boundary Condition Method). It relies on the Schelkunoff's equivalence theorem, which states that the field in a source-free region bounded by a surface Σ could be produced by a distribution of electric and magnetic currents on this surface, and, in this sense, the actual source distribution can be replaced by an equivalent one [179, 182]. In addition, the Null-Field Method relies on a decomposition of the field inside the scatterer in the VSH basis. However, such a decomposition is only rigorous for homogeneous scatterers inside the inscribed sphere of the scatterer. As a result, the Null-Field Method cannot be applied to inhomogeneous objects and it is only approximate for non-spherical homogeneous objects; the more the object is elongated, the more inaccurate the method is. Combining the Null-Field Method with the concept of discrete sources has allowed to partially circumvent the issue of the scatterer shape [168, 170], but the inapplicability to inhomogeneous objects remain.

The only way to calculate rigorously the T-matrix for an inhomogeneous scatterer with an arbitrary shape is to use a rigorous numerical method to compute the scatterer field. In a second step, the scattered field has to be projected onto the VSH basis. For this projection, the scattered field should be calculated either on a spherical surface around the object [171], on an arbitrary-shaped closed surface [172], or in the

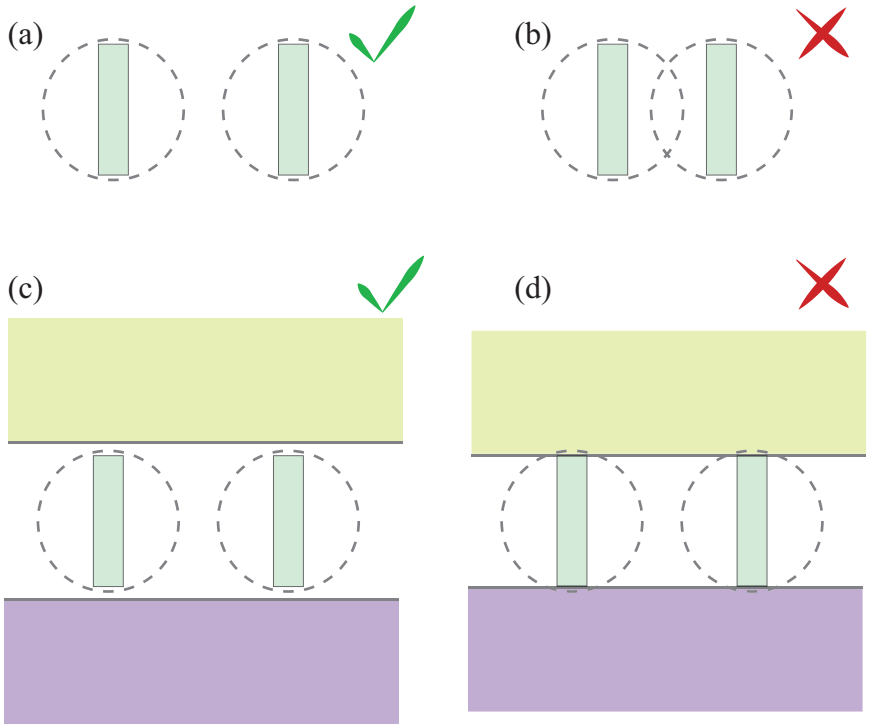

Figure III.2.: Schematic of different use-cases for calculating multiple scattering with the T-matrix method and their limitations. An elongated object is confined within an imaginary sphere, inside which the field cannot be determined. When multiple such objects are being brought together it is important to pay attention that their 'excluded' regions do not cross. Otherwise, it will give rise to numerical errors. (a) and (b) show, respectively, configurations of two elongated objects in a homogenous environment that can and cannot be treated with the T-matrix method. Subfigures (c) and (d) show similarly allowed and forbidden configurations when two scatterers are placed in a stratified medium. In that case , if two identical scatterers are located in two layers with different refractive indices, two different T-matrices have to be calculated, one for each refractive index. The objects cannot lie directly on top of a substrate, or, equally, touch the superstate, as shown in (d). Some gap has to be introduced, so that the circumscribing spheres do not cross any interface, see (c).

scatterer volume [183, 184].

We provide hereafter a brief demonstration of two equivalent closed-form expressions of the T-matrix elements T_{LK}. The first one involves the scattered field on a closed surface surrounding the scatterer, while the second one involves the total field inside the scatterer.

Since the operational basis is fixed, the T-matrix elements can be worked out column by column by successively computing the scattered fields upon the illumination with each regular VSH. For an incident field $\mathbf{E}_{inc}(\mathbf{r}) = \xi_P(k\mathbf{r})$, the expansion coefficients p_L of the scattered field are simply $p_L = T_{LP}$ since the coefficients a_K in Eq. (III.6) are equal to 0 for $K \neq P$ and 1 for $K = P$. Thus, calculating the scattered field for an incident field equal to a regular VSH and projecting it on the set of outgoing VSHs provides one column of the T-matrix. By repeating this calculation for all the desired regular VSHs (up to a chosen truncation rank), we obtain the whole T-matrix.

Let us now detail the projection of the scattered field onto the VSH basis. In other words, let us derive the closed-form expression of T-matrix elements T_{LP} as a function of the scattered field and the VSHs of order L and P.

The incoming/outgoing VSHs $\boldsymbol{\Xi}_L^{(\pm)}$ defined in Table III.1 are orthogonal to each other,

$$\begin{cases} \boldsymbol{\Xi}_L^{(\pm)} \otimes \breve{\boldsymbol{\Xi}}_K^{(\pm)} = \pm 4\delta_{LK}, \\ \boldsymbol{\Xi}_L^{(\pm)} \otimes \breve{\boldsymbol{\Xi}}_K^{(\mp)} = 0, \end{cases} \tag{III.8}$$

where δ_{LK} is the Kronecker symbol and a breve above $\boldsymbol{\Xi}$ transforms an outgoing (resp. incoming) VSH with an azimuthal number m into an incoming (resp. outgoing) VSH with an azimuthal number $-m$, $\breve{\boldsymbol{\Xi}}_{L(n,m)}^{(\pm)} = \boldsymbol{\Xi}_{L(n,-m)}^{(\mp)}$. The operator $\otimes$ denotes the following inner product between two electromagnetic fields $\boldsymbol{\Psi}_1 = (\mathbf{E}_1, \mathbf{H}_1)$ and $\boldsymbol{\Psi}_2 = (\mathbf{E}_2, \mathbf{H}_2)$,

$$\boldsymbol{\Psi}_1 \otimes \boldsymbol{\Psi}_2 \equiv \iint_\Sigma (\mathbf{E}_2 \times \mathbf{H}_1 - \mathbf{E}_1 \times \mathbf{H}_2) \cdot \mathrm{d}\mathbf{S} \tag{III.9}$$

with Σ a closed surface around the origin.

By combining the multipole expansion of the scattered field $\boldsymbol{\Psi}_s = (\mathbf{E}_s, \mathbf{H}_s)$ in Eq. (III.4) and the orthogonality of the VSHs, we get

$$\begin{aligned} \boldsymbol{\Psi}_s \otimes \breve{\boldsymbol{\Xi}}_L^{(+)} &= 4p_L, \\ \boldsymbol{\Psi}_s \otimes \breve{\boldsymbol{\Xi}}_L^{(-)} &= 0. \end{aligned} \tag{III.10}$$

The half-sum of these two equations provides a closed-form expression of the T-matrix elements

$$T_{LP} = \frac{1}{2}\mathbf{\Psi}_s^{(P)} \otimes \breve{\xi}_L, \tag{III.11}$$

where $\breve{\xi}_L$ is the regular VSH with an opposite azimuthal number compared to ξ_L. We have added the superscript $^{(P)}$ to the scattered field to stress that it is the field scattered by the object for an incident VSH of order P, $\mathbf{E}_{inc} = \xi_P$.

Equation (III.11) gives a closed-form expression of the T-matrix elements T_{LP} as a function of the scattered field evaluated over a closed surface surrounding the scatterer. With this formulation, the calculation of the T-matrix amounts to calculate the scattered field on this surface for different incident harmonics.

When using QNM theories for calculating light scattering, it is in general preferable to work with the field inside the scatterer [173]. We now show by using Lorentz reciprocity theorem that Eq. (III.11) is completely equivalent to a different closed-form expression that involves the total field inside the scatterer instead of the scattered field outside.

Lorentz reciprocity theorem relates two different solutions of Maxwell's equations. Two time harmonic electromagnetic fields $\mathbf{\Psi}_1 = (\mathbf{E}_1, \mathbf{H}_1)$ and $\mathbf{\Psi}_2 = (\mathbf{E}_2, \mathbf{H}_2)$ generated by current distributions $\mathbf{J}_1$ and $\mathbf{J}_2$ at the same frequency ω in the same medium (be it homogeneous or inhomogeneous) are related by

$$\mathbf{\Psi}_1 \otimes \mathbf{\Psi}_2 = \iint_\Sigma (\mathbf{E}_2 \times \mathbf{H}_1 - \mathbf{E}_1 \times \mathbf{H}_2) \cdot d\mathbf{S} = \iiint_V (\mathbf{J}_2 \cdot \mathbf{E}_1 - \mathbf{J}_1 \cdot \mathbf{E}_2)\, d\mathbf{r}^3, \tag{III.12}$$

where Σ is a closed surface encompassing a volume V. Note that the shape and position of the surface Σ are arbitrary. The demonstration of Lorentz reciprocity theorem and its most general expression for different frequencies and different media are given in Appendix C.

Let us apply Eq.(III.12) with $(\mathbf{E}_1, \mathbf{H}_1) = \breve{\xi}_L$. The latter is solution of Maxwell's equations at the frequency ω without source ($\mathbf{J}_1 = 0$) in the homogeneous medium of permittivity $\varepsilon_b = \varepsilon_0 n_b^2$. As a second solution $(\mathbf{E}_2, \mathbf{H}_2)$, we consider the scattered field $\mathbf{\Psi}_s^{(P)} = (\mathbf{E}_s^{(P)}, \mathbf{H}_s^{(P)})$ generated by an incident VSH of order P. As shown in Appendix D, the scattered field is solution of Maxwell's equations in the homogeneous medium of permittivity ε_b for a current distribution $\mathbf{J}_2 = -i\omega\Delta\varepsilon(\omega)\mathbf{E}$ with $\Delta\varepsilon(\omega) = \varepsilon(\omega) - \varepsilon_b$. In this expression, $\varepsilon(\omega)$ is the permittivity distribution of the scatterer and

$\mathbf{E} = \mathbf{E}_{\text{inc}} + \mathbf{E}_s$ is the total field. Equation(III.12) becomes

$$\breve{\xi}_L \otimes \mathbf{\Psi}_s^{(P)} = -i \iiint_V \omega \Delta\varepsilon(\omega)(\mathbf{E}_{\text{inc}} + \mathbf{E}_s^{(P)}) \cdot \breve{\xi}_L d\mathbf{r}^3. \tag{III.13}$$

Finally, by using Eq. (III.11) and replacing the incident field by its value we obtain

$$T_{LP} = \frac{1}{2i} \iiint_{V_{\text{scat}}} \omega \Delta\varepsilon(\omega)(\xi_P + \mathbf{E}_s^{(P)}) \cdot \breve{\xi}_L d\mathbf{r}^3. \tag{III.14}$$

Note that the volume integral is limited to the scatterer volume V_{scat} since $\Delta\varepsilon = 0$ outside the scatterer.

As a result of the orthogonality of the VSHs and Lorentz reciprocity theorem, we can compute the T-matrix elements either as an integral of the scattered field over a closed surface outside the scatterer [see Eq. (III.11)] or as an integral of the total field inside the volume of the scatterer [see Eq. (III.14)].

In the former case, the scattered field on a surface around the object has to be calculated. Some numerical methods (e.g., FEM) can accurately approximate a spherical surface with a tetrahedron mesh and calculate the field on the curved surface. Other are better fitted to produce the field on a rectangular box. On the other hand, Eq. (III.14) relates the total field inside the scatterer to a T-matrix element. This is the equation we will use in the following. To get the total field inside the object, we will use the QNM theory. Since to obtain the full T-matrix we have to recalculate the scattered field multiple times, we will greatly benefit from the semi-analytical nature of the QNM approach.

1.2 Quasi-normal mode formalism

Resonant physical systems support eigenmodes, which are non-trivial solutions of the underpinning state equations. In a closed (or periodic) conservative system they describe oscillations that can be sustained with a fixed frequency – the resonance frequency of the system.

Optical micro and nanoresonators make possible a number of modern optical devices and technologies, such as integrated photonic circuits, non-classical light sources (e.g., single photon sources), sensors, metamaterials, metasurfaces, etc. In optics we often deal with open non-conservative (non-Hermitian) systems, whose natural resonant modes are known as quasi-normal modes (QNMs) or resonant states. The prefix "quasi" is used to stress that they are the modes of non-conservative systems with

complex frequencies, whose imaginary part describes energy damping [173, 185–187]. Once a resonator is pumped and the excitation is removed, it begins to give off the energy through its modes via radiative channels or non-radiative ones (material absorption). This is why they are also known as leaky modes [188] or decaying states [189].

Resonances are commonly characterised by their quality factor Q – the ratio between the resonance frequency and its full width at half maximum. Any resonance with a finite Q-factor can be attributed to the excitation of a QNM. There are two generally distinguished types of optical resonances: (i) high-Q ones, typically achieved in lossless dielectric materials, where the sole decay channel is radiative; (ii) low-Q ones, typically in plasmonic cavities, where, in addition to radiation, a strong absorption is present.

Since they are the natural modes of the system, QNMs are very attractive to describe light interaction with optical resonators. However, because of the non-hermiticity of the system, a wide use of QNM-expansion formalisms has been hindered for a long time by mathematical and numerical difficulties. These difficulties were tackled in the 90s for 1D cavities and spherical resonators [186], but general QNM theories for 3D systems were still lacking. Recent works have made important progress in the development of modal theories based on QNM expansions for arbitrary 3D structures [156, 157, 175, 177, 190–193]. Quasi-normal mode theories now start to be mature and are used for an increasing number of applications thanks to the numerical efficiency they might offer, along with an improved physical interpretation [194].

This section is divided into four parts. First, in Subsection 1.2.a we lay out the formal definition of QNMs. Then, in Subsec. 1.2.b we briefly review current techniques for the calculation of QNM fields and complex frequencies. We use Subsec. 1.2.c to address the question of the QNM field normalisation. Finally, in Subsec. 1.2.d we discuss the representation of scattered fields as a weighted sum of QNMs. Analytical expressions for the excitation coefficients ('weights') are presented.

1.2.a Definition of quasi-normal modes

Any damped resonator, mechanical, acoustic or electromagnetic, exhibit multiple resonances of different frequencies and damping rates. In the frequency domain they correspond to sharp variations (e.g., maxima, minima, Fano line shapes) in the spectrum of the resonator response to an external excitation (transmission, absorption, scattered power, etc.). Within the framework of modal theories, the scattered field

of a resonator is represented as a sum of its different resonant modes,

$$\mathbf{\Psi}_s(\mathbf{r},\omega) = \sum_m \alpha_m(\omega)\tilde{\mathbf{\Psi}}_m(\mathbf{r}), \tag{III.15}$$

with ω the angular frequency of the excitation, $\tilde{\mathbf{\Psi}}_m = (\tilde{\mathbf{E}}_m, \tilde{\mathbf{H}}_m)$ the field vector that consists of the electric and magnetic fields, $\tilde{\mathbf{E}}_m$ and $\tilde{\mathbf{H}}_m$, of the m^{th} QNM, and α_m the complex excitation coefficient of the m^{th} QNM. The value of the excitation coefficient depends on the incident field. In addition to its field $\tilde{\mathbf{\Psi}}_m$, the m^{th} QNM is characterised by its complex eigenfrequency

$$\tilde{\omega}_m = \omega_m - i\frac{\omega_m}{2Q_m}, \tag{III.16}$$

with ω_m the resonance frequency and Q_m the quality factor.

Eigenmodes are intrinsic quantities of the system, independent of the excitation field. They are the solutions of time-harmonic source-free Maxwell's equations

$$\nabla \times \tilde{\mathbf{E}}_m = i\tilde{\omega}_m \mu(\mathbf{r},\tilde{\omega}_m)\tilde{\mathbf{H}}_m, \tag{III.17}$$

$$\nabla \times \tilde{\mathbf{H}}_m = -i\tilde{\omega}_m \varepsilon(\mathbf{r},\tilde{\omega}_m)\tilde{\mathbf{E}}_m, \tag{III.18}$$

with outgoing-wave boundary conditions. The materials, characterised by the permittivity $\varepsilon(\mathbf{r},\omega)$ and the permeability $\mu(\mathbf{r},\omega)$, can be inhomogeneous, dispersive (frequency-dependent), and absorptive. The system of equations takes the form of an eigenproblem with $\tilde{\omega}_m$ as eigenvalues and the fields $\tilde{\mathbf{\Psi}}_m$ as eigenvectors,

$$\begin{bmatrix} 0 & -i\mu^{-1}(\mathbf{r},\tilde{\omega}_m)\nabla\times \\ i\varepsilon^{-1}(\mathbf{r},\tilde{\omega}_m)\nabla\times & 0 \end{bmatrix} \begin{bmatrix} \tilde{\mathbf{H}}_m \\ \tilde{\mathbf{E}}_m \end{bmatrix} = \tilde{\omega}_m \begin{bmatrix} \tilde{\mathbf{H}}_m \\ \tilde{\mathbf{E}}_m \end{bmatrix}. \tag{III.19}$$

For non-dispersive materials, the eigenvalue problem is linear (the left-hand side does not depend on the frequency), of the form $\mathbf{M}\mathbf{u} + \omega\mathbf{u} = 0$ with $\mathbf{M}$ some operator matrix and $\mathbf{u}$ a vector. In contrast, for dispersive materials, Eq. (III.19) corresponds to a non-linear eigenvalue problem of the form $\mathbf{M}(\omega)\mathbf{u} + \omega\mathbf{u} = 0$. The latter can be solved with different strategies, which are briefly presented in the next subsection. The permittivity and permeability have to be defined at the complex frequency $\tilde{\omega}_m$, thus, their analytical continuation in the complex frequency plane is required, see for instance [195].

1.2.b Calculation of quasi-normal modes

Nowadays, there exist several different methods to calculate QNMs, which can be sorted in two main categories: the pole-search approach and the auxiliary-field approach. In the following, we briefly describe each approach. In this thesis, we have used the pole-search approach to calculate QNMs but we have also used theoretical concepts belonging to the auxiliary-field approach to derive a modal expansion of the T-matrix. More details on each approach can be found in [173] and different implementations of each method are described in a recent benchmark [157].

When driving excitation frequency approaches the one of the resonance in the complex plane, the system response diverges. This fact is commonly used to identify the resonant frequencies and to calculate QNMs by calculating poles of a given quantity. The diverging quantity may be the field itself or the determinant of the scattering matrix. For a 3D object (with the exception of a perfect sphere), an analytical form of the scattering matrix is not available, so it has to be computed numerically. One approach is to use an iterative method to converge on the pole value by searching for the complex zero of the diverging quantity inverted. To be efficient, such methods require a starting point (guess value) not to far in the complex plane from the pole.

In practice, to find the starting point for the iterations, we use Cauchy integrals with a crude mesh to obtain approximate locations of the poles in the region of the complex frequency plane under study. Then, we apply an iterative procedure based on an approximation of the inverse of the system response with a Padé approximant [156].

A completely different way to calculate QNMs is the auxiliary-field approach. It is based on the idea of introducing auxiliary fields to linearise the eigenvalue problem in Eq. (III.19), bringing it to the form of an augmented eigenvalue problem [175, 191, 196]. Here, the term "augmented" means that the eigenvector has a dimension larger than $(\mathbf{E}, \mathbf{H})$. This approach is more suitable than the pole-search approach when a large number of QNMs is searched for.

For the sake of illustration, let us consider a particular case, where the materials are non-magnetic ($\mu = \mu_0$) and their permittivity can be described by a single-pole Lorentz model,

$$\varepsilon(\omega) = \varepsilon_\infty - \varepsilon_\infty \frac{\omega_p^2}{\omega^2 - \omega_0^2 + i\omega\gamma}, \tag{III.20}$$

where the standard notations for the plasma frequency, ω_p, the damping rate, γ, the resonant frequency, ω_0, and the high-frequency permittivity, ε_∞, are used. For $\omega_0 = 0$, the Lorentz model reduces to the usual Drude model that can be used to describe metals at visible and near-infrared frequencies. The following equations

can be straightforwardly modified to accommodate for multiple Lorentz poles, i.e., multiple terms in Eq. (III.20) with different values of the parameters ω_p, ω_0, and γ.

For such dispersions, the eigenvalue problem can be linearised by introducing two auxiliary fields [175, 191, 196]. Namely, the polarisation $\mathbf{P} = -\varepsilon_\infty \omega_p^2 \left(\omega^2 - \omega_0^2 + i\omega\gamma\right)^{-1} \mathbf{E}$ and the current $\mathbf{J} = -i\omega\mathbf{P}$. Incorporating these two definitions into Maxwell's equations, we obtain an augmented but linear eigenvalue problem

$$\begin{bmatrix} 0 & -i\mu_0^{-1}\nabla\times & 0 & 0 \\ i\varepsilon_\infty^{-1}\nabla\times & 0 & 0 & -i\varepsilon_\infty^{-1} \\ 0 & 0 & 0 & i \\ 0 & i\omega_p^2\varepsilon_\infty & -i\omega_0^2 & -i\gamma \end{bmatrix} \begin{bmatrix} \tilde{\mathbf{H}}_m \\ \tilde{\mathbf{E}}_m \\ \tilde{\mathbf{P}}_m \\ \tilde{\mathbf{J}}_m \end{bmatrix} = \tilde{\omega}_m \begin{bmatrix} \tilde{\mathbf{H}}_m \\ \tilde{\mathbf{E}}_m \\ \tilde{\mathbf{P}}_m \\ \tilde{\mathbf{J}}_m \end{bmatrix} \tag{III.21}$$

An additional pair of auxiliary fields $\mathbf{J}$ and $\mathbf{P}$ are required for each new Lorentz pole, which, in case of a N-pole model of the permittivity, leads to a $2(N+1) \times 2(N+1)$ matrix. On the other hand, the particular case of a Drude model ($\omega_0 = 0$, the pole of the function $\varepsilon(\omega)$ becomes purely imaginary, $\omega = -i\gamma$), a single auxiliary field $\mathbf{J}$ suffices. This is the model used later in this work.

Equation (III.21) is a generic expression written with operators. In practice, it has to be discretized by using a numerical method. Finite Element Method is well suited for this purpose; different FEM implementations of the auxiliary-field approach are described in [157, 175, 197]. The auxiliary-field approach has also been implemented with the Finite Difference (FD) method in the frequency domain [191, 196].

1.2.c Normalisation of quasi-normal modes

Normalisation is an important issue to handle when using QNMs. The known and obvious hurdle for normalising QNMs is the fact that, for open systems, the QNM field diverges exponentially away from the resonator for $\mathbf{r} \to \infty$. This singular behaviour of the field in the frequency domain (there is no divergence in the time domain) is due to the presence of the imaginary part of $\tilde{\omega}_m$. Energy of a non-conservative system is necessarily damped in time, which imposes a negative imaginary part for $\tilde{\omega}_m$ when using the $\exp(-i\omega t)$ convention for time-harmonic fields, see Eq. (III.16). As a consequence, in the far field, an outgoing wave of the form $(1/r)\exp[-i\tilde{\omega}_m(t - r/c)]$ grows exponentially as $(1/r)\exp[\omega_m r/(2Q_m c)]$ because of the necessary minus sign in the propagation term $(t - r/c)$. The field divergence is obviously problematic to normalise a QNM with some integral of the electromagnetic field over the whole space.

Two main normalisation approaches that solve the divergence issue have been re-

cently proposed. The first one is based on an integration along a well-chosen axis in the complex $\mathbf{r}$ plane that allows cancelling the exponential growth of the field, as originally proposed in [186] for 1D systems. For 3D geometries with an arbitrary shape, this integration in the complex plane can be realised by using perfectly matched layers (PMLs). A PML is a complex anisotropic refractive index transformation in the space surrounding the scattering object in the calculation domain. They cause the field strength to decrease exponentially inside this region. Thus, the field can be integrated in the 'whole space' without encountering any divergent quantities. The normalisation condition is [190]

$$\iiint_{\Omega\cup\Omega_{\mathrm{PML}}} \left[\tilde{\mathbf{E}}_m \cdot \frac{\partial\omega\varepsilon}{\partial\omega}\tilde{\mathbf{E}}_m - \tilde{\mathbf{H}}_m \cdot \frac{\partial\omega\mu}{\partial\omega}\tilde{\mathbf{H}}_m\right] \mathrm{d}^3\mathbf{r} = 1, \tag{III.22}$$

where the integration is over all computational space including the PML. QNM normalisation can also be performed by replacing the volume integral in the PML domain by a surface integral that avoids the divergence by compensating for the exponential increase [198]. A detailed discussion of these normalisation approaches can be found in [173, 199].

A totally different normalisation method is the pole-response normalisation [156, 173]. It relies on the fact that QNMs are poles of the scattering matrix. It is more general than the normalisation with PMLs, working with any type of numerical boundary, and directly provides the normalised mode that fulfils Eq. (III.22) without the need to calculate an integral of the electromagnetic field. As one approaches the QNM eigenfrequency, the scattered field goes to infinity and becomes dominated by the corresponding QNM:

$$\boldsymbol{\Psi}_s(\mathbf{r}) \approx \alpha_m(\omega, \tilde{\omega}_m, \tilde{\boldsymbol{\Psi}}_m)\tilde{\boldsymbol{\Psi}}_m(\mathbf{r}), \tag{III.23}$$

where the m^{th} QNM field $\tilde{\boldsymbol{\Psi}}_m$ is assumed to be normalised. Since the sum over the modes is absent, a closed form expression for the normalised mode $\tilde{\boldsymbol{\Psi}}_m$ as a function of the scattered field $\tilde{\boldsymbol{\Psi}}_s$ can be derived from Eq. III.23, as shown in [156]. This approach requires the knowledge of the source and the scattered field at a complex frequency close to the pole $\omega \approx \tilde{\omega}_m$. This is the normalisation approach used in this work.

1.2.d QNM expansion of the scattered field: excitation coefficient α_m expression

Within the framework of modal theories, the scattered field of a resonator is represented as a sum of its different resonant modes. In practice, the sum is truncated

to a finite number M of QNMs,

$$\mathbf{E}_s(\omega, \mathbf{r}) \approx \sum_{m=1}^{M} \alpha_m(\omega) \tilde{\mathbf{E}}_m(\mathbf{r}). \tag{III.24}$$

The accuracy of the field decomposition over the QNM basis directly depends on how many (and which) modes we take into account. The method is most efficient and convenient when a relatively small number of QNMs is sufficient to reach the desired accuracy. The mode excitation coefficient, $\alpha_m(\omega)$, is a quantity that explicitly depends on the excitation and can be given by a closed-form expression. Thus, once the modes frequencies $\tilde{\omega}_m$ and their fields $\tilde{\mathbf{E}}_m(\mathbf{r})$ are pre-calculated rigorously, the scattered field $\mathbf{E}_s(\omega, \mathbf{r})$ can be obtained analytically. This will be especially useful when calculating the full T-matrix, as we have to iterate over all VSHs.

Different expressions for the $\alpha_m(\omega)$ coefficients can be found in the literature [173]. In this thesis, we use the expression derived in [175] for resonators composed of dispersive materials. We briefly present hereafter the key points of the derivation, which is based on the use of Lorentz reciprocity theorem.

Let us apply Lorentz reciprocity theorem [Eq. (C.6), see derivation in Appendix C] to the following solutions of Maxwell's equations. The first solution $(\mathbf{E}_1, \mathbf{H}_1)$ is the field scattered by the resonator at the frequency ω. As shown in Appendix D, the scattered field is the field radiated by a current source $-i\omega\Delta\varepsilon\mathbf{E}_b$ in a medium described by the permittivity and permeability distributions $\varepsilon(\mathbf{r}, \omega)$ and $\mu(\mathbf{r}, \omega)$. As a second solution $(\mathbf{E}_2, \mathbf{H}_2)$, we consider the n^{th} QNM, which is solution of Maxwell's equations without source at the complex frequency $\tilde{\omega}_n$. The volume enclosed by the surface Σ in Eq. (C.6) is taken as the integration domain $\Omega \cup \Omega_{\text{PML}}$ used in the QNM norm. Since the field vanishes at the PML outer boundary, the surface integral in the left-hand side of Lorentz reciprocity theorem vanishes. Finally, we arrive at the following equation

$$\iiint_{\Omega\cup\Omega_{\text{PML}}} \left\{ \mathbf{E}_s \cdot \left[\omega\varepsilon(\mathbf{r}, \omega) - \tilde{\omega}_n\varepsilon(\mathbf{r}, \tilde{\omega}_n)\right] \tilde{\mathbf{E}}_n - \mathbf{H}_s \cdot \left[\omega\mu(\mathbf{r}, \omega) - \tilde{\omega}_n\mu(\mathbf{r}, \tilde{\omega}_n)\right] \tilde{\mathbf{H}}_n \right\} dV = \\ -\omega \iiint_{V_{\text{scat}}} \Delta\varepsilon(\mathbf{r}, \omega)\mathbf{E}_b \cdot \tilde{\mathbf{E}}_n dV, \tag{III.25}$$

with V_{scat} the volume of the scatterer where $\Delta\varepsilon \neq 0$.

Plugging in the expansion of the scattered field in the form of Eq.(III.24), this

equation is transformed into

$$\sum_{m=1}^{M} B_{nm}(\omega)\alpha_m(\omega) = -\omega \iiint_{V_{\text{scat}}} \Delta\varepsilon(\mathbf{r},\omega)\mathbf{E}_b \cdot \tilde{\mathbf{E}}_n dV, \tag{III.26}$$

where

$$B_{nm}(\omega) = \iiint_{\Omega\cup\Omega_{\text{PML}}} \left\{\mathbf{E}_m \cdot [\omega\varepsilon(\omega) - \tilde{\omega}_n\varepsilon(\tilde{\omega}_n)]\,\tilde{\mathbf{E}}_n - \mathbf{H}_m \cdot [\omega\mu(\omega) - \tilde{\omega}_n\mu(\tilde{\omega}_n)]\,\tilde{\mathbf{H}}_n\right\} dV. \tag{III.27}$$

Solving this system of M equations will yield the α_m's. In the general case of some arbitrary $\varepsilon(\omega)$ function, the system has to be solved numerically. However, two particular cases that are of a significant importance in practice allow for a derivation of a closed-form solution for the α_m's. These are the non-dispersive case and the Lorentz (or Drude) dispersion.

For non-dispersive materials, we get $B_{nm}(\omega) = 0$ for $n \neq m$ due to the QNM orthogonality [190] and $B_{mm}(\omega) = (\omega - \tilde{\omega}_m) \iiint \left(\tilde{\mathbf{E}}_m \cdot \varepsilon\tilde{\mathbf{E}}_m - \tilde{\mathbf{H}}_m \cdot \mu\tilde{\mathbf{H}}_m\right) dV$. Therefore, the system of equations (III.26) is diagonal and gives trivially

$$\alpha_m(\omega) = -\frac{\omega}{\omega - \tilde{\omega}_m} \iiint_{V_{\text{scat}}} \Delta\varepsilon(\mathbf{r})\mathbf{E}_b \cdot \tilde{\mathbf{E}}_m dV \tag{III.28}$$

where we have taken into account the normalisation condition (III.22). The integration is performed inside the resonator, since $\Delta\varepsilon$ is zero outside.

The second important case corresponds to materials that can be described by the Lorentz-Drude dispersion model. In that case, it has been demonstrated that the augmented eigenmodes composed of the electromagnetic field and the auxiliary field [see Eq. (III.21)] are also orthogonal, but with respect to a different inner product, which incorporate the auxiliary fields $\mathbf{J}$ and $\mathbf{P}$ [175]. The derivation follows the same idea as in the case of non-dispersive materials, but Lorenz reciprocity theorem has to be modified to take into the auxiliary fields, which makes the process more algebra heavy. The detailed derivation can be found in the Supplemental Material of [175] and yields the following closed-form expression for the excitation coefficients

$$\alpha_m(\omega) = \left[\varepsilon_b - \varepsilon_\infty - \frac{\tilde{\omega}_m}{\omega - \tilde{\omega}_m}(\varepsilon(\tilde{\omega}_m) - \varepsilon_b)\right] \iiint_{V_{\text{scat}}} \mathbf{E}_b(\mathbf{r})\tilde{\mathbf{E}}_m dV. \tag{III.29}$$

We have considered here a homogeneous scatterer (ε is constant inside the volume V_{scat}), but a similar expression exists for the inhomogeneous ones [175].

2 T-matrix quasi-normal mode expansion

In this section we derive the QNM expansion of the T-matrix. We show that the same QNM formalism [same excitation coefficient $\alpha_m(\omega)$] can lead to two different formulations of the T-matrix modal decomposition. We derive a first "direct" formulation of the T-matrix modal expansion in Subsec. III.2.1. This formulation directly combines the expression of the T-matrix elements given in Eq. (III.14) as a function of the total field and the permittivity difference $\Delta\varepsilon$ with the QNM expansion given in Eq. (III.24). We refer to this expression as the field-based formulation. Then, we show in Subsec. III.2.2 that a different QNM decomposition is obtained if one introduces the current auxiliary field $\mathbf{J}$ in the expression of the T-matrix elements. We refer to this second formulation as the current-based formulation. The differences between both formulations and their origin are discussed in Subsec. III.2.3.

2.1 Field-based formulation of the T-matrix modal decomposition

For the sake of convenience, let us first recall the expression of the T-matrix elements as a function of the total field inside the scatterer [Eq. (III.14)] and the QNM decomposition of the scattered field [Eq. (III.24)].

The T-matrix elements can be expressed as

$$T_{LP} = \frac{1}{2}\iiint_{V_{\text{scat}}} (-i\omega)[\varepsilon(\omega) - \varepsilon_b]\mathbf{E}\cdot\breve{\xi}_L d\mathbf{r}^3, \tag{III.30}$$

where the total field inside the volume V_{scat} is given by $\mathbf{E} = \xi_P + \mathbf{E}_s^{(P)}$, with ξ_P the regular VSH of order P that serves as the incident field and $\mathbf{E}_s^{(P)}$ the corresponding scattered field defined as $\mathbf{E}_s = \mathbf{E} - \mathbf{E}_{\text{inc}}$.

Within the QNM formalism, the scattered field can be expressed as a sum of QNMs,

$$E_s^{(P)}(\mathbf{r},\omega) = \sum_m \alpha_m^{(P)}(\omega)\tilde{\mathbf{E}}_m(\mathbf{r}), \tag{III.31}$$

where we have used the superscript $^{(P)}$ on the excitation coefficient to keep in mind that it depends on the incident field ξ_P.

By combining these two equations we directly obtain a QNM expansion of the T-matrix

$$T_{LP} = \frac{1}{2}\iiint_{V_{\text{scat}}} (-i\omega)[\varepsilon(\omega) - \varepsilon_b]\left(\xi_P + \sum_m \alpha_m^{(P)}(\omega)\tilde{\mathbf{E}}_m\right)\cdot\breve{\xi}_L d\mathbf{r}^3, \tag{III.32}$$

which can be rewritten in the form of a non-resonant term (independent of the QNMs) and a sum over modal quantities weighted by the excitation coefficient $\alpha_m^{(P)}$

$$\boxed{T_{LP} = \frac{\omega}{2i} \iiint_{V_{\text{scat}}} [\varepsilon(\omega) - \varepsilon_b] \xi_P \cdot \breve{\xi}_L d\mathbf{r}^3 + \sum_m \alpha_m^{(P)}(\omega) \left[\frac{\omega}{2i} \iiint_{V_{\text{scat}}} [\varepsilon(\omega) - \varepsilon_b] \tilde{\mathbf{E}}_m \cdot \breve{\xi}_L d\mathbf{r}^3 \right].} \tag{III.33}$$

This equation is the field-based formulation of the T-matrix QNM expansion. For the excitation coefficient $\alpha_m^{(P)}$, we use the expression derived in [175] for dispersive systems, see Eq. (III.29).

We will see now that, if one introduces the QNM formalism in a slightly modified expression of the T-matrix elements, we get a different modal decomposition.

2.2 Current-based formulation of the T-matrix modal decomposition

The T-matrix elements depend on the current induced inside the scatterer, $-i\omega[\varepsilon(\omega) - \varepsilon_b]\mathbf{E}$. In a dispersive material, the permittivity $\varepsilon(\omega)$ results from the movement of the free electrons in a medium of permittivity ε_∞. Thus, the current induced inside the scatterer is given by the sum of two contributions: a polarisation current proportional to $(\varepsilon_\infty - \varepsilon_b)$ and a current $\mathbf{J}$ that results from the movement of the free electrons,

$$\mathbf{J} = -i\omega \frac{-\varepsilon_\infty \omega_p^2}{\omega^2 - \omega_0^2 + i\omega\gamma} \mathbf{E} = -i\omega[\varepsilon(\omega) - \varepsilon_\infty]\mathbf{E}. \tag{III.34}$$

The latter exactly corresponds to the auxiliary field introduced in the QNM formalism of dispersive resonators, see Eq. (III.21). Note that the quantity $\varepsilon(\omega) - \varepsilon_\infty$, which corresponds to the free-electrons contribution to the scatterer permittivity, is different from $\Delta\varepsilon(\omega) = \varepsilon(\omega) - \varepsilon_b$ in Eq. (III.30), which is the difference between the permittivity distribution inside the scatterer and the permittivity of the surrounding medium.

By reintroducing the hidden auxiliary field $\mathbf{J}$ in Eq. (III.30), the expression of the T-matrix elements becomes

$$T_{LP} = \frac{1}{2} \iiint_{V_{\text{scat}}} \left[(-i\omega)(\varepsilon_\infty - \varepsilon_b)(\xi_P + \mathbf{E}_s^{(P)}) + \mathbf{J}^{(P)} \right] \cdot \breve{\xi}_L d\mathbf{r}^3. \tag{III.35}$$

Again, the superscript $^{(P)}$ is used to keep in mind that $\mathbf{E}_s^{(P)}$ and $\mathbf{J}^{(P)}$ are produced by considering the regular VSH of order P as an incident field. Of course, Eq. (III.35) is completely equivalent to Eq. (III.30).

Within the QNM formalism based on the introduction of auxiliary fields [175], both

the scattered field $\mathbf{E}_s^{(P)}$ and the current $\mathbf{J}^{(P)}$ are expanded onto the set of QNMs. Therefore, in addition to Eq. (III.31), we also have

$$\mathbf{J}^{(P)}(\mathbf{r},\omega) = \sum_m \alpha_m(\omega)^{(P)}\tilde{\mathbf{J}}_m(\mathbf{r}). \tag{III.36}$$

According to the linearised eigenvalue problem given by Eq. (III.21), the following relation holds between the modal field $\tilde{\mathbf{E}}_m$ and the modal current $\tilde{\mathbf{J}}_m$,

$$\tilde{\mathbf{J}}_m = -i\tilde{\omega}_m[\varepsilon(\tilde{\omega}_m) - \varepsilon_\infty]\tilde{\mathbf{E}}_m. \tag{III.37}$$

By combining Eqs. (III.35)-(III.37), as well as Eq. (III.31), we obtain the second QNM expansion of the T-matrix

$$\boxed{\begin{aligned} T_{LP} &= \frac{\omega}{2i}\iiint_{V_{\text{scat}}} (\varepsilon_\infty - \varepsilon_b)\xi_P\cdot\breve{\xi}_L d\mathbf{r}^3 + \\ &+ \sum_m \alpha_m^{(P)}(\omega)\left[\frac{\omega}{2i}\iiint_{V_{\text{scat}}} (\varepsilon_\infty - \varepsilon_b)\tilde{\mathbf{E}}_m\cdot\breve{\xi}_L d\mathbf{r}^3 + \frac{\tilde{\omega}_m}{2i}\iiint_{V_{\text{scat}}} [\varepsilon(\tilde{\omega}_m) - \varepsilon_\infty]\tilde{\mathbf{E}}_m\cdot\breve{\xi}_L d\mathbf{r}^3\right]. \end{aligned}} \tag{III.38}$$

This equation is the current-based formulation of the T-matrix QNM expansion. We use the same excitation coefficient $\alpha_m^{(P)}$ as in Eq. (III.33), namely the expression derived in [175] for dispersive systems, see Eq. (III.29). We would like to stress that even though Eq. (III.38) was derived using the auxiliary field $\mathbf{J}$, only the electric field of a QNM finally appears in the formula. This is an important point, which makes Eq. (III.38) usable with any QNM solver, even one which does not rely on auxiliary fields [157].

2.3 Discussion on the difference between the field and the current-based formulations

Both Eqs. (III.33) and (III.38) are written in the form of a non-resonant term (independent of the QNMs) and a sum over modal quantities weighted by the excitation coefficient $\alpha_m^{(P)}$. However, if one compares carefully both equations, one readily sees that the non-resonant terms are slightly different and the modal quantities are also slightly different. Since the starting points, Eqs. (III.30) and (III.35), are completely equivalent, the differences can only come from the application of the QNM formalism.

In the field-based formulation, the total current induced inside the scatterer, $-i\omega$

$\Delta\varepsilon(\omega)\mathbf{E}$, is split in two parts: the first one results from the incident field while the second one is proportional to the scattered field. This separation between both contributions is imposed by QNM theory, which expands the scattered field onto the QNM set, and not the total field. On the other hand, in the current-based formulation, we reintroduce the hidden contribution of the free electrons. The latter is, in the QNM formalism developed in [175], entirely expanded onto the QNM set without separating the part proportional to the incident field from the one proportional to the scattered field. This is the origin of the difference between Eqs. (III.33) and (III.38). The fraction of the induced current that is due to the movement of the free electrons driven by the incident field is expressed as a sum of QNMs in the current-based formulation, while it is incorporated in the non-resonant term in the field-based formulation.

At first sight, this point seems to be the signature of an inconsistency in the QNM formalism. In fact, the issue of the role and the expression of non-resonant contributions in QNM decompositions is currently an open issue in the community. Recent works on QNM theory have proposed different expressions of the non-resonant contribution [175–177, 200]. In order to test this point, we compare in Sec. III.3 the convergence of both formulations as the number of QNMs in the expansion is increased. We show that Eqs. (III.33) and (III.38) both provide a good accuracy for a large enough number of modes. However, the convergence speed of both formulations for a small number of modes is different.

2.4 Cross-sections

Cross-section (scattering, absorption, extinction) is an important physical quantity that is often used to characterise a scatterer resonant behaviour. In this section, for completeness, we provide expressions to derive extinction and scattering cross-sections (absorption is equal to their difference) from a given T-matrix.

The extinction cross-section σ_{ext} is proportional to the real part of the T-matrix:

$$\sigma_{\text{ext}} = -\frac{1}{4S_0}\sum_L\sum_P \Re\text{e}\left[(\mathbf{B}^*\mathbf{B}\mathbf{T})_{LP}\right], \tag{III.39}$$

where S_0 is the time-averaged Poynting vector of the incident plane-wave, $\mathbf{B}$ a diag-

onal matrix, such that

$$\begin{cases} B_{LL} = \dfrac{i^n}{k_0}\sqrt{\dfrac{2\pi}{\sqrt{\varepsilon_b}}(2n+1)}, & \text{if } |m| = 1, \\ B_{LL} = 0, & \text{if } m \neq 1 \end{cases} \tag{III.40}$$

where n and m are the degree and the azimuthal number, respectively, that correspond to a given L index (see Table III.1) and the asterisk stands for the complex conjugation.

The scattering cross-section, on the other hand, and therefore the absorption one as well, since $\sigma_{\text{abs}} = \sigma_{\text{ext}} - \sigma_{\text{sca}}$, does not depend linearly on the QNMs, which does not allow for the separation of their contributions. The scattering cross-section is related to the T-matrix according to the following relation:

$$\sigma_{\text{sca}} = \frac{1}{4S_0}\sum_L\sum_P |\,(\mathbf{BT})_{LP}\,|^2. \tag{III.41}$$

3 Test case of a sphere

In this section, we test the accuracy of the modal decompositions of the T-matrix derived above. We test both the field and the current-based formulations, Eqs. (III.33) and (III.38), respectively, and compare their convergence speed as the number of QNMs retained in the expansion is increased. In order to really test the modal decomposition and not the accuracy of a given numerical method, we need a system whose T-matrix can be calculated analytically.

We consider a metallic nanosphere for which exact values of the T-matrix elements can be calculated with Mie theory. In addition, the QNMs of a sphere can also be easily calculated by taking advantage of the analytic form of the scattering matrix. It is thus feasible to calculate an arbitrary large number of QNMs. A Drude model [see Eq. (III.20)] with $\omega_0 = 0$, $\varepsilon_\infty = 1$, $\omega_p = 1.26\times10^{16}\text{rad}\cdot\text{s}^{-1}$, and $\gamma = 0.01125\omega_p$ will be used throughout this section. This model can closely represent the dispersion of gold in the infra-red band and was previously used in [190]. We study two spheres with different radii: $R = 25$ nm and $R = 100$ nm. Since the resonances are less pronounced for larger metallic spheres, the convergence of the QNM decomposition is expected to be slower. Therefore, the $R = 100$ nm case constitutes a more demanding test.

3.1 Quasi-normal modes

To get the QNMs frequencies of a homogeneous sphere, we have calculated the poles of the scattering matrix (S-matrix) in the complex plane. For a sphere, the scattering matrices for electric and magnetic polarisations are known analytically. They are given by [201]

$$S_n^{(e)} = -\frac{h_n^{(-)}(k_bR)}{h_n^{(+)}(k_bR)} \frac{\varepsilon_s(\omega)\varphi_n^{(-)}(k_bR) - \varphi_n^{(1)}(k_sR)}{\varepsilon_s(\omega)\varphi_n^{(+)}(k_bR) - \varphi_n^{(1)}(k_sR)}, \tag{III.42}$$

$$S_n^{(h)} = -\frac{h_n^{(-)}(k_bR)}{h_n^{(+)}(k_bR)} \frac{\varphi_n^{(-)}(k_bR) - \varphi_n^{(1)}(k_sR)}{\varphi_n^{(+)}(k_bR) - \varphi_n^{(1)}(k_sR)}, \tag{III.43}$$

where $k_b = k_0 n_b$ and k_s are the wavenumbers in the surrounding medium and inside the sphere, respectively, $\varphi_n^{(\pm)}(z) = \xi_n'^{(\pm)}(z)/h_n^{(\pm)}(z)$, $\varphi_n^{(1)}(z) = \psi_n'(z)/j_n(z)$, with $j_n(z)$ and $\psi_n(z)$ being respectively the spherical Bessel and Riccati-Bessel functions, $h_n^{(+)}(z)$ and $\xi_n^{(+)}(z)$ – spherical Hankel and Riccati-Hankel functions of the first kind (superscript '$-$' denotes their counterparts of the second kind). The superscripts (e) and (h) denote electric and magnetic polarisations and index n indicates the degree.

The S-matrix has a similar physical sense to the T-matrix: it relates the incoming field to the outgoing. They are related in a linear manner as $\mathbf{S} = 2\mathbf{T} + \mathbf{I}$, with $\mathbf{I}$ being the identity matrix. The S-matrix elements of a sphere are diagonal and degenerate with respect to the azimuthal number $m \in [-n, n]$. As a consequence, the QNMs of a sphere are also degenerate with respect to m. Each value of the degree n corresponds to a different set of complex frequencies, see Fig. III.3. For $n = 1$, each QNM is threefold degenerate, for $n = 2$, each QNM is fivefold degenerate, etc.

An iterative method is most suitable and efficient to get the QNM complex frequencies by searching for the roots of the S-matrix denominator of Eqs. (III.42) and (III.43) for electric and magnetic polarisations, respectively. Since the calculations are rapid, it is feasible to select almost arbitrary starting points on the complex grid.[1] A better approach might be to map the values of the inverse of the denominator in the complex plane and use the Cauchy integral theorem to determine the locations of the poles with a good approximation which can later be refined in a few iterations of a root-search method.

Figure III.3 shows the calculated QNM frequencies (for electric polarisation) $\tilde{k}_m = \tilde{\omega}_m/c = 2\pi/\tilde{\lambda}_m$ in the complex plane for a sphere of $R = 25$ nm in air. An infinite

[1] S-matrix poles of a sphere can be imagined as positioned on a single curve in the complex wavenumer space (see Fig. III.3), rather than scattered randomly, which is helpful for an arbitrary, but educated, guess of a starting point.

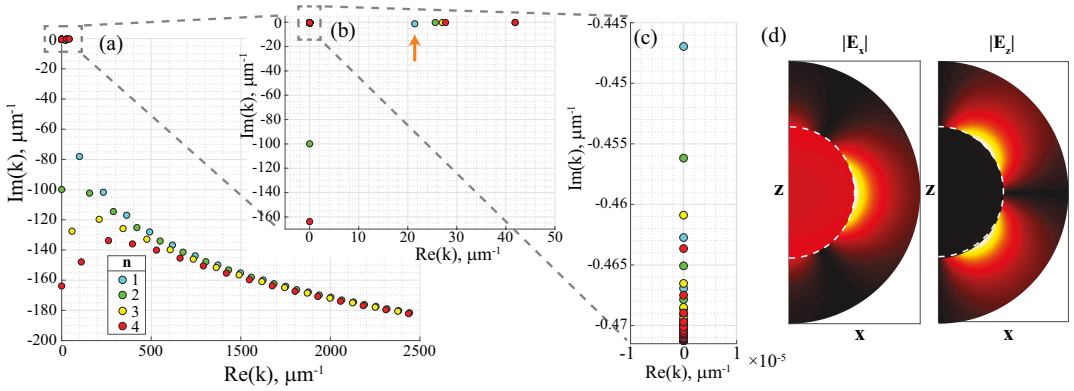

Figure III.3.: Frequencies $\tilde{k} = \tilde{\omega}/c$ in μm^{-1} of the modes in the complex plane, as indicated by the circles of four different colours, corresponding to the values of n between one and four, as labelled on the figure (a). The mode with $n = 1$ closest to the imaginary axis, but not lying on it, is the electric dipole mode. It is pointed out with an arrow in (b); its field profile is displayed in (d). Subfigure (c) shows the enlarged region where the stationary modes (purely imaginary eigenfrequency) accumulate around the pole of the Drude model $\omega = -i\gamma$. Sphere radius is $R = 25$ nm, surrounding space index $n_b = 1$, Drude dispersion parameters are specified in the introduction of this chapter.

discrete set of modes exists for each value of the degree n; we have gathered in Fig. III.3 73 modes for $n = 1$ (blue dots), 88 for $n = 2$ (green dots), 68 for $n = 3$ (yellow dots), and 87 for $n = 4$ (red dots). Three distinct categories of modes can be identified for each value of the degree n. First, a long tail formed by QNMs with a very large frequency (both real and imaginary parts) that tends to infinity can be seen in Fig. III.3(a). A second category of QNMs highlighted in Fig. III.3(b) corresponds to the well-known electric dipole resonance ($n = 1$, see the arrow), the electric quadrupole resonance ($n = 2$), etc. The complex frequencies of these modes have a small imaginary part (compared to all other modes) and a real part that lie in the visible part of the spectrum. These modes are responsible for the resonances that can be observed in the spectrum of the sphere response to any incident field. Finally, a third category of QNMs is shown in Fig. III.3(c). It is a infinite family of stationary modes (real part of the frequency equals to zero) with an accumulation point at $\omega = -i\gamma$. This value corresponds to the pole of the Drude model used for the metal permittivity. For a structure composed of a material described by a Lorentz model [see Eq. (III.20)] with $\gamma \ll \omega_0$, the accumulation point will be located at $\omega = \omega_0 - i\gamma/2$ in the complex plane.

If we are concerned with a working frequency close to the electric-dipole resonance in the visible [see the arrow in Fig. III.3(b)], the excitation coefficient of a given mode, and thus its contribution to the reconstruction of any physical quantity, decreases rapidly with its eigenfrequency, as we move farther from the resonance in the complex plane. So much so that, beyond a certain point, the contribution of the stationary modes (purely imaginary eigenfrequency) becomes larger than the contribution of the modes in the high frequency tail.

If ω and $(\mathbf{E}, \mathbf{H})$ are solutions of Maxwell's equations without source, then $-\omega^*$ and $(\mathbf{E}^*, \mathbf{H}^*)$ are as well, where the asterisk indicates complex conjugation, since $\varepsilon(-\omega^*) = \varepsilon^*(\omega)$ due to the Hermitian symmetry of real Fourier transforms. This means that there is a second family of modes (with $\mathrm{Re}(\tilde{\omega}_m) < 0$ and $\mathrm{Im}(\tilde{\omega}_m) < 0$) symmetrically located in the complex plane with respect to the imaginary axis to the ones in Fig. III.3. They have to be included in the QNM expansion as well and, obviously, no additional numerical calculations are required since these modes can be deduced from the ones with $\mathrm{Re}(\tilde{\omega}_m) > 0$ by complex conjugation.

Having computed $\tilde{k}$ for a given n and polarisation, the field of the mode can be calculated for a fixed azimuthal number m, as a harmonic of the corresponding degree L defined in Table III.1 (see, for example, Ref. [201]).

For objects that possess rotation symmetry, the volume integrals in the modal expansion of the T-matrix can be easily transformed to surface integrals, by switching to the spherical coordinates and integrating over the azimuthal angle φ analytically. This greatly reduces the time and memory requirements of the calculation, making this approach even more attractive for cylindrical scatterers, as will be demonstrated in the following chapter.

3.2 Reconstruction of the T-matrix

In this subsection we study the convergence of the two QNM decompositions for the T-matrix coefficients, the field-based formulation [see Eq. (III.33)] and the current-based formulation [see Eq. (III.38)].

Because the sphere we take as a study example is small compared to the wavelength (radius $R = 25$ nm $\approx \lambda/10$ in air) and the Drude model approximates the permittivity of gold in the infra-red part of the spectrum, its scattering properties can be reasonably well approximated with the electric dipole mode ($n = 1$), which gives the major contribution to the most significant T-matrix elements, in the visible

spectral range around the resonance. The complex frequency of the electric dipole mode is $\tilde{k}_m = 21.42 - 1.26i\ \mu m^{-1}$; it is shown by the arrow in Fig. III.3(b). The T-matrix elements with electric polarisation have a much larger contribution than the magnetic ones. Furthermore, the magnitude of T-matrix elements of degree $n = 2$ is five times smaller than the dipolar one. The first complex frequency of the dominant $n = 2$ mode is $\tilde{k}_m = 25.6 - 0.26i\ \mu m^{-1}$. The magnitude of the T-matrix elements of degree $n = 3$ is about 50 times smaller than the one of $n = 2$.

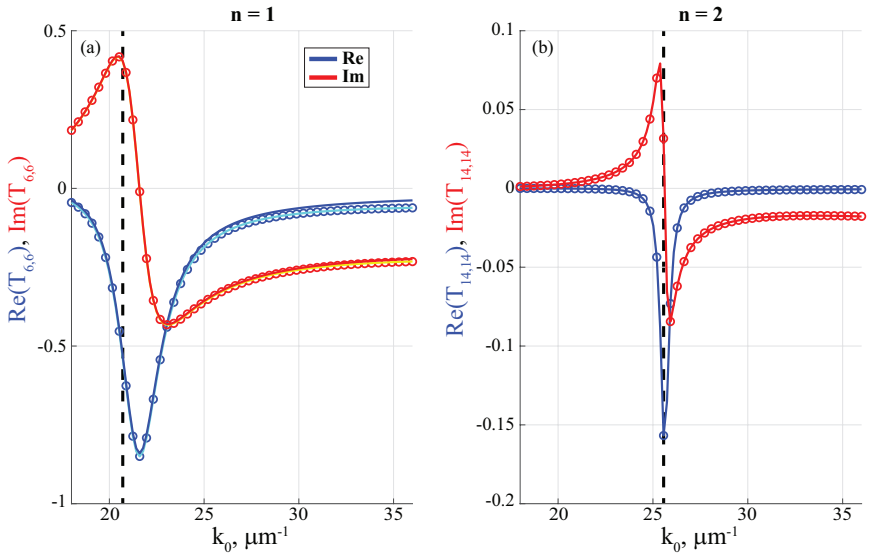

Figure III.4.: Diagonal T-matrix elements with $L = 6$ ($n = 1$, $m = 1$, electric) and $L = 14$ ($n = 2$, $m = 1$, electric) for (a) and (b), respectively, as a function of the frequency for a sphere of radius $R = 25$ nm in air (same sphere as in Fig. III.3). Circles mark the exact Mie theory solution and solid lines show the results obtained using Eq. (III.38) with a single QNM that corresponds to the appropriate resonance. Colour is used to tell the real part (blue) from the imaginary part (red). Additionally, in (a) cyan and yellow lines (for real and imaginary parts, respectively) are used for the results obtained with 40 QNMs. The dashed black vertical line shows $\mathrm{Re}(\tilde{k}_m)$ of the principal QNM that were singled out for each case.

The above point is illustrated in Fig. III.4, where we plot the T-matrix elements with $L = 6$ ($n = 1$, $m = 1$, electric) and $L = 14$ ($n = 2$, $m = 1$, electric) as a function of the frequency $k_0 = \omega/c = 2\pi/\lambda$. The T-matrix elements are rigorously calculated with Mie theory (circles) and the results are compared with the modal decomposition of Eq. (III.38). For both values of L, a single mode of the corresponding degree n is sufficient for an accurate reconstruction of the resonant spectrum. By adding

additional QNMs, the accuracy improves and for the $T_{6,6}$ elements the two solutions become indistinguishable with the naked eye after a few dozen of modes are included. For $T_{14,14}$ one QNM is sufficient for the two curves to practically overlay, because its resonance has a higher quality factor than the one for $T_{6,6}$.

Let us now study more precisely the convergence of the modal expansion as the number of modes is increased. Figure III.5 overlays the results for a sphere of $R = 25$ nm in air obtained using Eq. (III.33) (blue lines) and Eq. (III.38) (orange lines). The QNM excitation coefficients $\alpha_m(\omega)$ were calculated using Eq. (III.29) in both cases. We show the relative error on the real part and the imaginary part of the T-matrix elements, $|\mathrm{Re}(T_{\mathrm{modal}} - T_{\mathrm{Mie}})|/|\mathrm{Re}(T_{\mathrm{Mie}})|$ and $|\mathrm{Im}(T_{\mathrm{modal}} - T_{\mathrm{Mie}})|/|\mathrm{Im}(T_{\mathrm{Mie}})|$, versus the number of modes we take into account in the expansion [M in Eq. (III.24)]. Subfigures (a) and (c) show the error on the real part of the diagonal T-matrix element with $L = 6$ ($n = 1$, $m = 1$, electric) for $k_0 = 22\mu m^{-1}$ and $L = 14$ ($n = 2$, $m = 1$, electric) for $k_0 = 26\mu m^{-1}$, respectively. The values for k_0 were chosen close to the respective resonance for quicker convergence in order to better test the limits. Similarly, (b) and (d) show the error on the imaginary parts of the same T-matrix elements.

In Fig. III.5, a given mode with an eigenfrequency $\tilde{k}_m$ is considered separately from its $-\tilde{k}_m^*$ cousin. The modes are sorted according to their contribution to modulus of the T-matrix elements. The $-\tilde{k}_m^*$ modes have a smaller contribution then the $\tilde{k}_m$ modes. For the high frequency modes, both contributions from $\tilde{k}_m$ and $-\tilde{k}_m^\star$ are almost equal and can be of a different sign (positive or negative). This results in the oscillations that can be observed in Fig. III.5, either on the real or the imaginary part of $\mathbf{T}$. In Fig. III.5(a), the first mode is the electric-dipole mode, $\tilde{k}_1$, the second mode is the next closest to it in the complex plane ($\tilde{k}_2 = 99.4 - 78i$), followed by $-\tilde{k}_2^*$ and $-\tilde{k}_1^*$, and so on. The stationary (purely imaginary) modes have a contribution on the order between 10^{-7} and 10^{-13} (the closer to $-i\gamma$, the higher the contribution) relative to the absolute value of the T-matrix element, which means that in Fig. III.5 they are spread in the second part of the curve. There is an additional stationary mode for even values of the degree n. Its role is more significant, however. In fact, it is the fourth most significant mode in Fig. III.5(c,d), between $-\tilde{k}_2^*$ and $-\tilde{k}_1^*$.

We can see that the current-based formulation shows a quicker convergence than the field-based one. The relative error of the current-based formulation is smaller than 10^{-3} for only 5 modes in the expansion, whereas the field-based formulation needs more than 50 modes to reach the same accuracy. The relative error on $\mathrm{Im}(T_{6,6})$ stays even above 10^{-3} for a modal expansion with 200 modes. However, the current-based

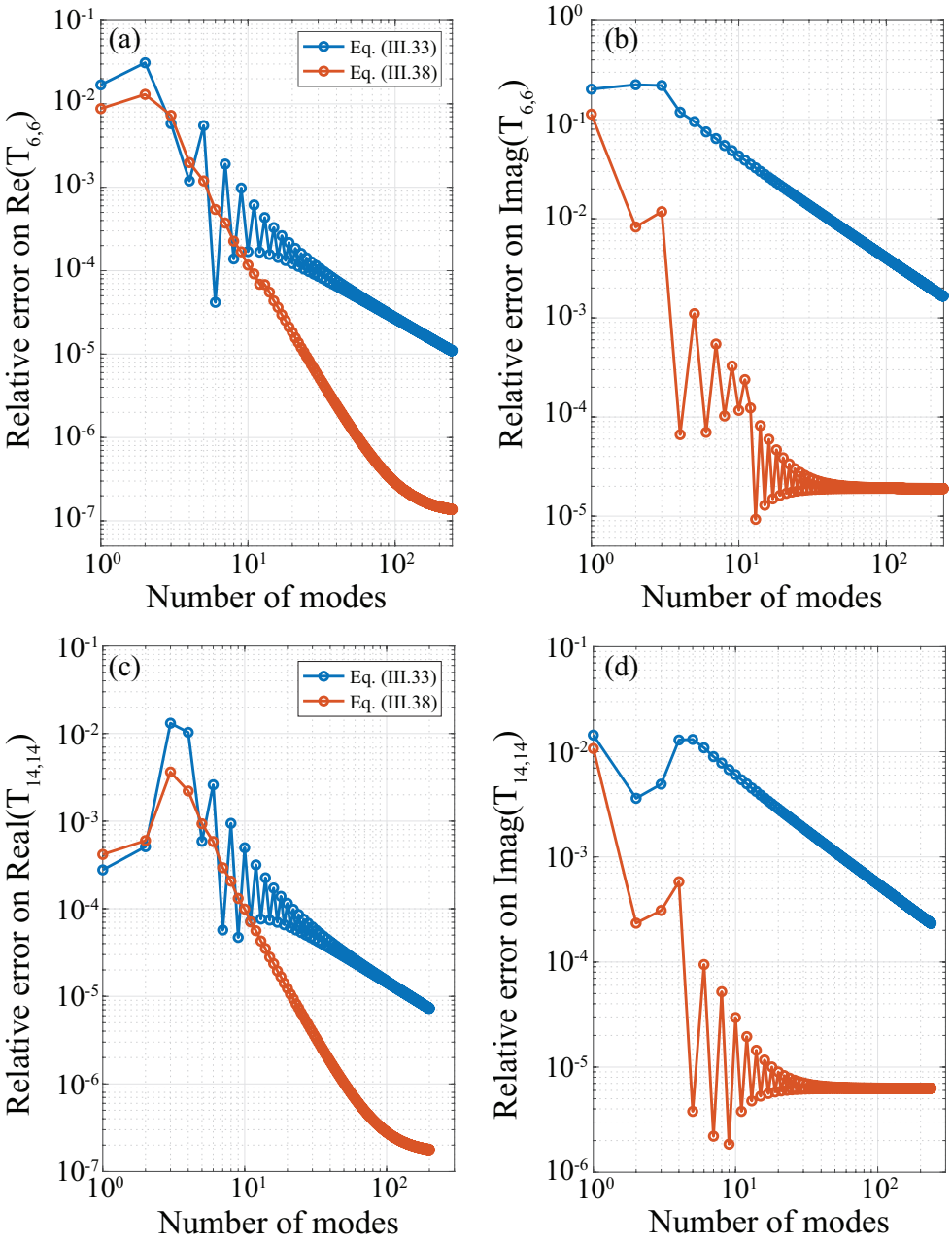

Figure III.5.: Relative error on the real [(a) and (c)] and imaginary [(b) and (d)] parts of the diagonal T-matrix elements with $L = 6$ ($n = 1$, $m = 1$, electric) [(a) and (b)] and $L = 14$ ($n = 2$, $m = 1$, electric) [(c) and (d)] versus the number of QNMs taken into account. The sphere radius is $R = 25$ nm and its permittivity is given by the Drude model specified in the introduction to this section. Index of the surrounding medium $n_b = 1$. The frequency is chosen close to the resonance of the T-matrix elements (see black dashed lines in Fig. III.4), $k_0 = 22\mu m^{-1}$ for $T_{6,6}$ in (a) and (b) and $k_0 = 26\mu m^{-1}$ for $T_{14,14}$ in (c) and (d).

formulation seems to converge towards a value slightly different from the correct one, as evidenced by a "saturation" of the error for a large number of modes, especially for the imaginary part of the T-matrix. We believe that this behaviour could be improved with a modified QNM formulation with a different non-resonant term.

Finally, in Fig. III.6 and III.7 we provide the same results as in Figs. III.4 and III.5, but for a bigger sphere of radius $R = 100$ nm. Since the resonances of a larger plasmonic object are less pronounced due to stronger radiation losses, the spectrum of the T-matrix elements cannot be as accurately represented with a single mode, see Fig. III.6. As a consequence, both formulations of the modal decomposition convergence more slowly, as seen in Fig. III.7. In addition, the saturation of the current-based formulation for a large number of modes appears sooner, i.e., for a larger relative error.

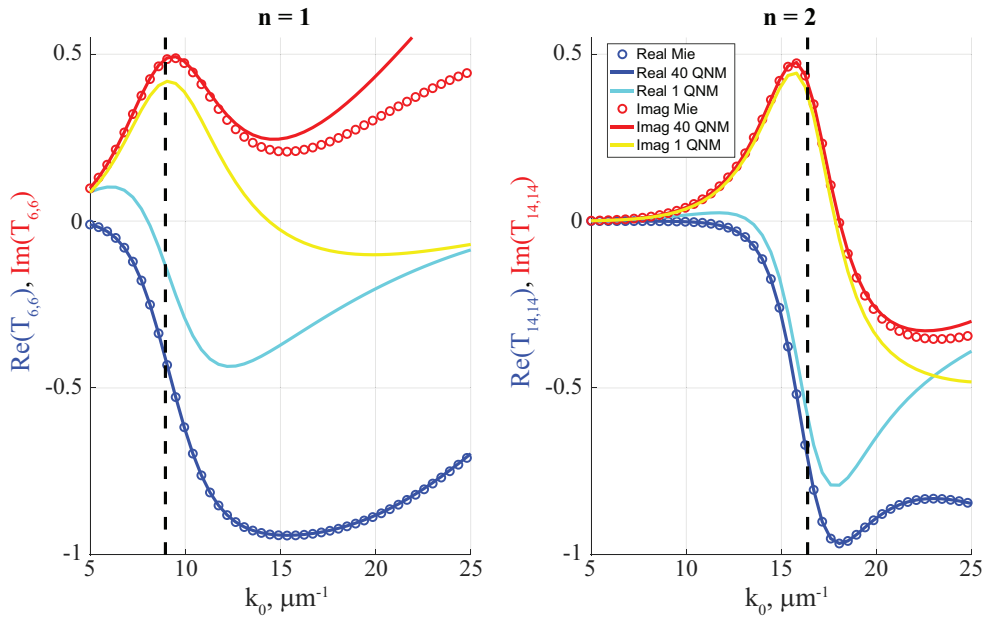

Figure III.6.: Diagonal T-matrix elements with $L = 6$ ($n = 1$, $m = 1$, electric) and $L = 14$ ($n = 2$, $m = 1$, electric) for (a) and (b), respectively, as a function of the frequency for a sphere of radius $R = 100$ nm in air. Circles mark the exact Mie theory solution and solid lines show the results obtained using Eq. (III.38) with a single QNM that corresponds to the appropriate resonance. Colour is used to tell the real part (blue) from the imaginary part (red). Additionally, cyan and yellow lines (for real and imaginary parts, respectively) are used for the results obtained with 40 QNMs. The dashed black vertical line shows $\mathrm{Re}(\tilde{k}_m)$ of the principal QNM that were singled out for each case.

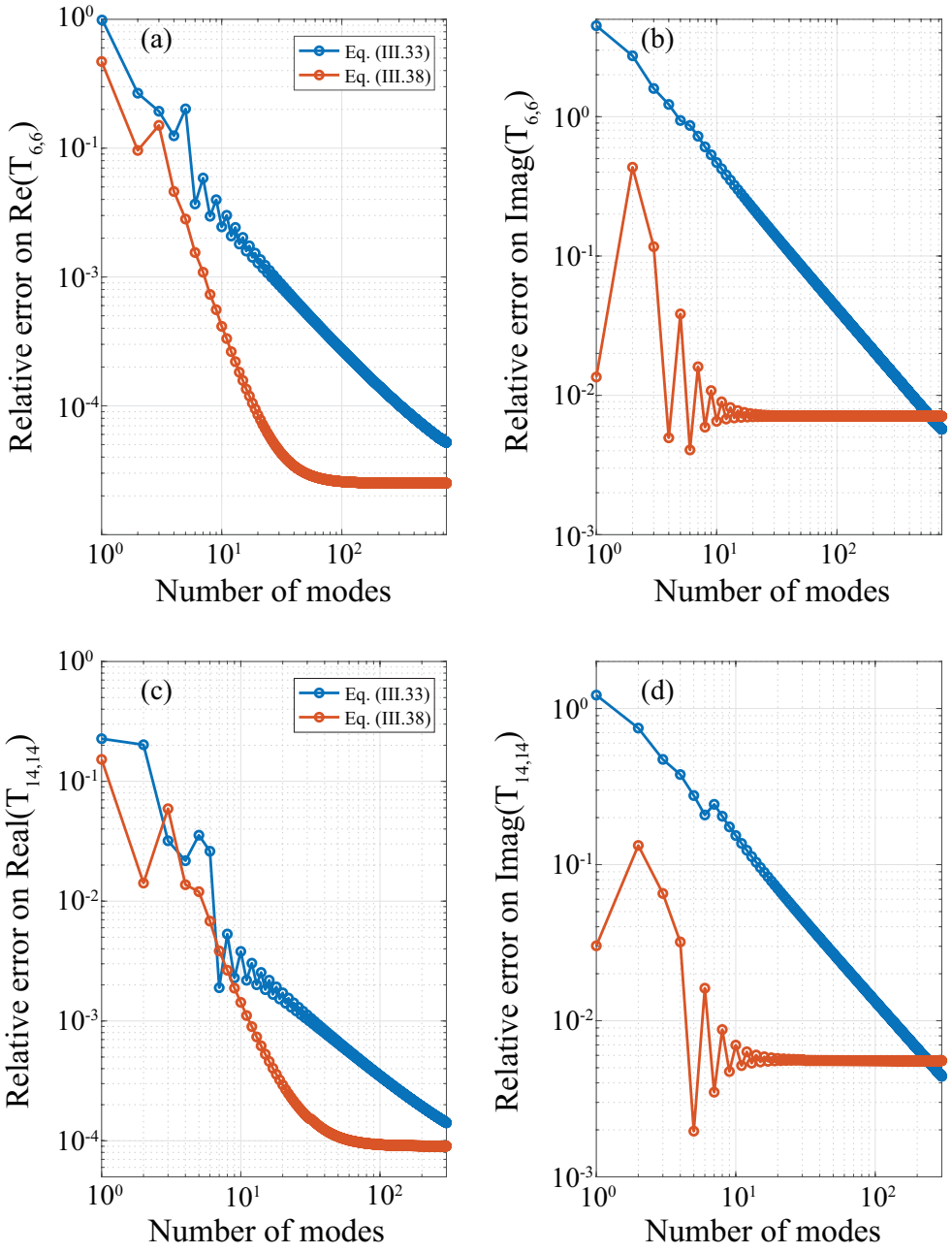

Figure III.7.: Relative error on the real [(a) and (c)] and imaginary [(b) and (d)] parts of the diagonal T-matrix elements with $L = 6$ [(a) and (b)] and $L = 14$ [(c) and (d)] versus the number of QNMs taken into account. The sphere radius is $R = 100$ nm and its permittivity is given by the Drude model specified in the introduction to this section. Index of the surrounding medium $n_b = 1$. The frequency is chosen close to the resonance of the T-matrix elements (see black dashed lines in Fig. III.6), $k_0 = 9\mu m^{-1}$ for (a) and (b) and $k_0 = 16\mu m^{-1}$ for (c) and (d).

4 Conclusion

In this chapter we have introduced a QNM expansion of the T-matrix of 3D resonant scatterers. We have derived and tested two different formulations. The first one, referred to as the field-based formulation, is based on a the expression of the T-matrix as a function of the total field and the total permittivity difference resulting from the presence of the scatterer. The second formulation, referred to as the current-based formation, is based on the expression of the T-matrix as a function of an auxiliary field that represents the current induced inside the scatterer due to the excitation of free charges. Both formulations provide closed-form expressions for the T-matrix elements that depend only on overlap integrals between VSHs and the electric field of the scatterer eigenmodes, which makes them readily usable with any QNM solver.

As a demonstrative example, we have considered a metallic sphere and looked at the accuracy of the QNM expansion with respect to the number of modes taken into account. Mie theory provides an exact reference for the T-matrix, which is not available for an object of arbitrary shape (or even for a finite-length cylinder). In addition, the QNMs of a sphere are the VSHs at a complex frequency, and thus can be calculated analytically. This allows us to look at the contribution of the very high-frequency modes, for which $\varepsilon \to \varepsilon_\infty$. We observe a few common trends: (i) real part of $\mathbf{T}$ converges more quickly than the imaginary part; (ii) current-based formulation provides a quicker convergence than the field-based one; (iii) current-based formulation seems to converge toward a slightly incorrect value. This last point is probably due to the non-resonant term in the QNM expansion, which is different in both formulations. This issue clearly requires further investigations.

Chapter IV

Quasi-normal modes based calculation of nonspherical nanoantennas

In this chapter we apply the modal decomposition of the T-matrix outlined in Chapter III to the calculation of light scattering by ensembles of nonspherical nanoresonators. We start by looking at a single metallic nanorod (cylinder of finite length). Such plasmonic scatterers, rod or disk-shaped, are interesting by themselves, thanks to the electric dipole mode they sustain, or as a building block for clusters, metasurfaces, etc. [27, 86, 202–209]. We focus on the T-matrix of a single nanorod because one can then calculate the response of any ensemble of nanorods inside a homogeneous environment or a layered medium from the knowledge of the T-matrices of each individual scatterer. The theory behind this calculation, the multipolar multiple-scattering theory, was thoroughly developed over the years. A comprehensive list of links is available in Ref. [169], as well as in later updates to the database from Mishchenko and colleagues.

We use a multipolar multiple-scattering code that was already implemented at Laboratoire Charles Fabry for calculating the multiple scattering by ensembles of spheres. We have extended it by using as an input a T-matrix calculated semi-analytically with a QNM expansion. We would like to stress that this approach is particularly well-suited for structures that consist of several instances of identical scatterers (dimer, trimer, clusters, Yagi-Uda antennas, periodic arrays, gradient metasurfaces) [1, 73, 210–213].

This chapter is divided into five sections. Firstly, in Section IV.1 we calculate the QNMs and reconstruct the T-matrix of an individual metallic nanorod with a few tenth of modes. It will be the basis for further calculations. Using this T-matrix, we calculate in Sec. IV.2 the scattering and absorption cross-sections of a dimer comprised of two identical nanorods. In Sec. IV.3 we further test the QNM expansion by calculating the emission of a dipole source inside a Yagi-Uda antenna made of six metallic nanorods. Section IV.4 is devoted to the calculation of the absorption inside a periodic array of nanorods. In each case (dimer, Yagi-Uda antenna, periodic array),

the semi-analytical results obtained with the modal decomposition of the T-matrix are compared with rigorous numerical calculations performed with an in-house FEM code. Finally, in Sec. IV.5 we discuss the different steps of the T-matrix calculation with the QNM theory, focusing on the computation times and comparing them to the FEM calculation.

1 Metallic cylindrical nanorod

As an illustrative example of a 3D cylindrical scatterer, we take a 30 nm wide, 100 nm long nanorod studied in Refs. [156, 190], with the same permittivity as the sphere in Sec. III.3 (see Fig. IV.1). This time, however, we consider a non-unitary refractive index for the outside space, $n_b = 1.5$. In this environment, such a nanorod has its electric dipole (ED) resonance in the near infrared around $\lambda = 920$ nm and can be accurately represented by a single mode over quite a broad spectral range. Such condition is most favourable for the QNM approach.

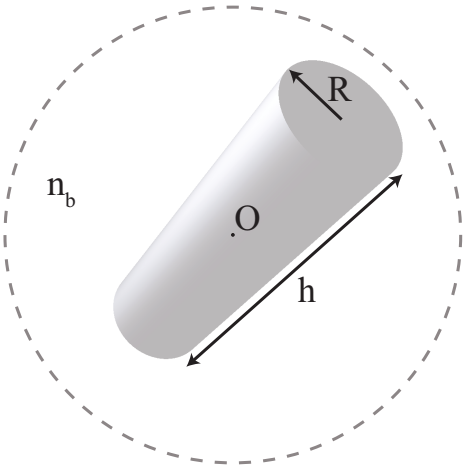

Figure IV.1.: Schematic of the metallic nanorod. The major geometrical parameters are its length, h, and radius, R, which are 100 and 15 nm, respectively, for the nanorod studied in this section. The constant index of the surrounding space is labelled with n_b. Gray dashed circle traces the boundary of the imaginary sphere with the centre in O inside which the T-matrix method does not permit to obtain the scattered field.

1.1 Quasi-normal modes

As mentioned in Subsec. III.1.2, in general, QNM frequencies can be numerically found by iteratively computing a response (S-matrix, field, etc.) of the resonator to a closely located source with a complex emission frequency, and converging to a point in the complex frequency space where this response diverges.[1] This is the first step in this method. In order not to look blindly in the complex plane, we first calculate a map of the resonator response as a function of the real and imaginary parts of the frequency. Then, we use the local extrema as starting points for the iterative root-search algorithm, as done in Sec. III.3. The frequency step is a crucial parameter that determines the time-efficiency and the accuracy of the method, as some QNMs, especially for larger wavenumbers, can be located close together and, as a result, fail to be distinguished. In addition, a smaller step will provide a starting point closer to the real value. However, in practice, this is not necessarily useful, as the time increase required to calculate the response on a finer grid outweighs (often by more than one order of magnitude) the time needed for one or two additional iterations of the root-search algorithm. Therefore, the optimal step size is not grounded in some simple physical or numerical considerations, rather it requires developing intuition or a rule of thumb for a given set of conditions. Further discussion of this crucial step is provided in Sec. IV.5.

In order to obtain the normalised field of a QNM, various solvers and options are available [157]. For instance, the same solver as the one used to calculate iteratively the QNM frequency can be used. The source will be driven at a complex frequency close to the one of the mode, $\omega \approx \omega_m$ and the normalised QNM field can be deduced from the scattered field, see Eq. (8) in Ref. [156] and the discussion in Subsec. 1.2.c.

Because of the rotational symmetry, the QNMs of a nanorod are degenerate with respect to the sign of the azimuthal number m. This fact reduces the number of unknown T-matrix elements almost in half, as the ones which differ only by the sign of m are identical to each other. Due to this degeneracy, the QNM fields and complex frequencies have to be calculated only for each non-negative value of m. The frequency for $-m$ is identical and the field for $-m$ can be obtained by changing the sign of the y-component of the electric field $\tilde{\mathbf{E}}$ and the $x-$ and z-components of the magnetic field $\tilde{\mathbf{H}}$. Depending on the type of solver used, symmetry conditions or positions of the excitation source can prevent some modes from being found. Unlike the case of a sphere discussed in the previous chapter, QNMs of a cylinder cannot be

[1] In practice, it is numerically preferable to look for the zeros of the inverse value.

sorted beforehand by the value of the degree n. To distinguish the modes, we have to either look at their field profile, or at which T-matrix element it contributes the most.

Figure IV.2(a) marks the locations in the complex frequency plane of several modes with m values ranging from zero to three. The principal ED resonance is the one with the smallest real part of $\tilde{k}_m = \tilde{\omega}_m/c$ (c is the speed of light in vacuum) for $m = 0$ (pointed at with an orange arrow). Its field profile is plotted in Fig. IV.2(b). This mode can be excited with a plane wave incident perpendicularly to the rod axis and with its electric field polarised along it. All other modes are relatively distant in terms of the real part, which is a manifestation of the fact that a single QNM accurately describes the behaviour of the nanorod over a relatively broad spectral range. In addition, there is no mode with the same value of m and a large imaginary part, which would result in a spectrally broad contribution due to a large resonance width.

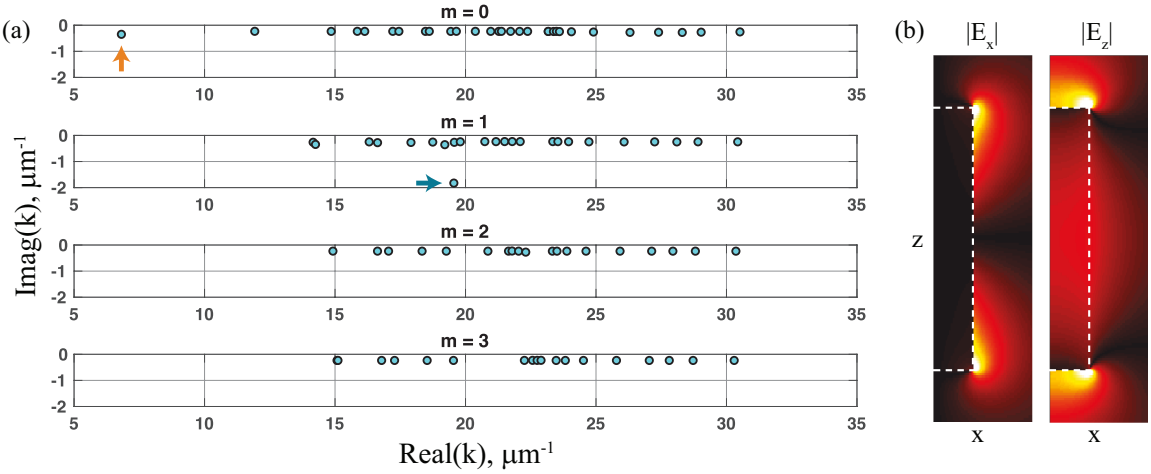

Figure IV.2.: (a) QNM frequencies of the metallic nanorod in the complex plane (blue circles) for different values of the azimuthal number m, $m = 0$, 1, 2, and 3 from top to bottom. The mode closest to the imaginary axis is the electric dipole mode (indicated with an orange arrow), whose field profile is displayed in (b). The blue arrow points at a mode with a large imaginary part, which has a broad (albeit relatively weak in our band) contribution to the spectrum.

In the case of a sphere, a mode of a particular L number (set of n, m, and polarisation, see Table III.1 for the definition) contributes only to the L^{th} diagonal element of the T-matrix, and $T_{LP} = 0$ for $L \neq P$. This property is due to the orthogonality of the VSHs. For a nonspherical body of revolution (e.g., a nanorod or a disk), however, the modes are only characterised by their azimuthal number m. As a consequence,

the T-matrix is not diagonal and some off-diagonal elements are not equal to zero.[2] The relation $T_{LP} = 0$ only holds for L and P values such that their azimuthal numbers m are unequal.

We use an aperiodic Fourier modal method dedicated to body-of-revolution objects and developed at the Laboratoire Charles Fabry [214] to calculate the QNMs up to $m = 10$. Normalisation is done according to Eq. (8) of Ref. [156]. In addition, throughout this chapter we are using Eq. (III.29) for calculating the excitation coefficients $\alpha(\omega)$ of the modes and the current-based formulation for the modal decomposition of the T-matrix, see Eq. (III.38). We have chosen to use the current-based formulation because, even if it seems to converge towards a slightly incorrect value, it provides a smaller error than the field-based formulation for a small number of modes, which will be our case here. In addition, when we say we consider a mode $\tilde{k}_m$, we automatically include the contribution of the mode with $-\tilde{k}_m^*$.

1.2 Reconstruction of the T-matrix

Figure IV.3 shows the results for the T-matrix calculation in the spectral range around the nanorod fundamental resonance. We have calculated the modal expansion of the T-matrix and we compare the modal expansion with the values labelled with circles. We call these values "exact", even if, strictly speaking, they are not. They were obtained as follows. The nanorod is illuminated by M point sources. The radiation of each is expanded in a set of L regular VSHs, according to the degree n that we chose for the T-matrix. This gives M vectors of length L, which we combine in a rectangular matrix $\mathbf{A}$ of size $L \times M$. The scattered fields generated by each source individually are expanded in a set of outgoing VSHs and brought together as a second rectangular matrix $\mathbf{B}$ of size $L \times M$. The T-matrix $\mathbf{T}$ is defined through $\mathbf{B} = \mathbf{T} \cdot \mathbf{A}$ and can be obtained with the pseudo-inverse of $\mathbf{A}$, as $\mathbf{T} = \mathbf{B} \cdot \mathbf{A}^{-1}$. We have checked the validity of this approach with FEM calculations (not shown here). However, even though they proved useful as a general reference, these results cannot be as accurate as Mie theory in the case of a sphere and should be taken with a grain of scepticism, as small discrepancies are to be expected, especially for higher-order elements, due to numerical and methodological reasons. Indeed, the sources used to

[2] See VSH orthogonality condition [Eq. (III.10)]. This fact also becomes readily evident if we consider an overlap integral used for T_{LP} matrix element calculation, e.g., Eq. (III.38). The total field depends on φ as $\exp(im_P\varphi)$, while the $\breve{\xi}_L$ harmonics as $\exp(-im_L\varphi)$, where m_P and m_L are the azimuthal numbers corresponding to L and P, respectively. Unless $m_L = m_P$, this exponential term with make the integral equal to zero.

generate the incident fields have to mimic VSHs with a high degree in order to fully explore the T-matrix. This is all the more difficult as the degree increases.

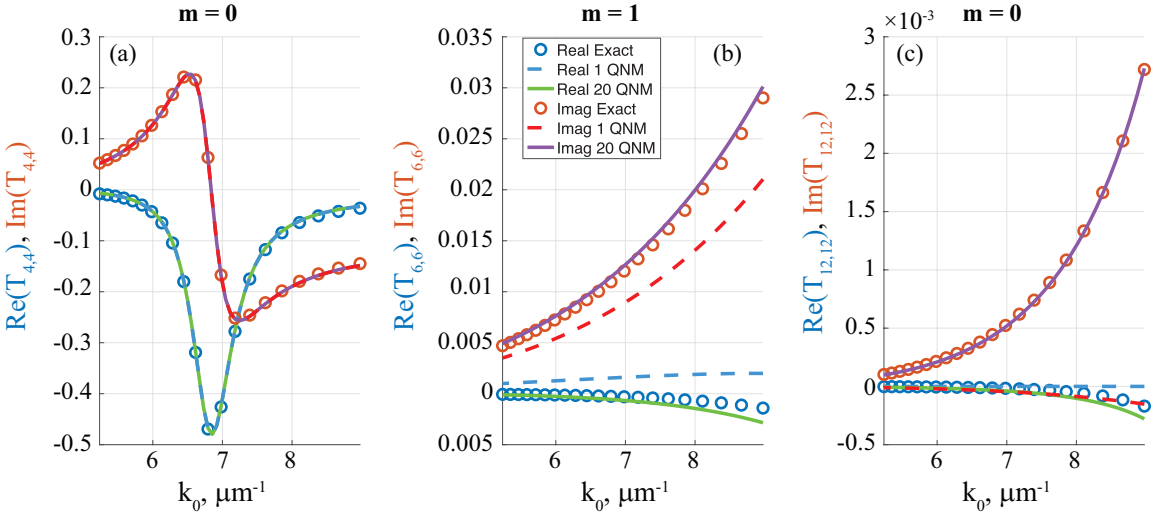

Figure IV.3.: Diagonal T-matrix elements versus $k_0 = 2\pi/\lambda = \omega/c$ for $L = 4$, 6, and 12 for (a), (b), and (c), respectively. The legend is valid for all three subfigures. Circles are used to indicate the reference T-matrix calculation, solid lines – a single QNM contribution, dashed – 20 first QNMs.

The three subfigures differ from each other only by the value of the L index of a diagonal element that they depict. Figure IV.3(a) shows $T_{4,4}$ as a function of the wavenumber $k_0 = 2\pi/\lambda = \omega/c$, which corresponds to $n = 1, m = 0$, electrical polarisation. The resonant behaviour is accurately described with a single mode [the one indicated with an orange arrow in Fig. IV.2(a)] [190]. Adding additional modes with the same azimuthal number m does not significantly influence the result, as the convergence is rather slow. Figure IV.3(b) and (c) display $T_{6,6}$ and $T_{12,12}$, respectively, which correspond to ($n = 1$, $m = 1$, electric) and ($n = 2$, $m = 0$, electric). In this spectral range the magnitude of these T-matrix elements is much smaller (one and two orders of magnitude smaller, respectively) than the one of $T_{4,4}$, because the object is small compared to the wavelength and we are far away on the spectral axis from their resonances. As a result, a single mode often is not sufficient to accurately represent these higher-order elements of the T-matrix. In Fig. IV.3(b) for demonstration purposes we single out the mode with the largest imaginary part of all those corresponding to $m = 1$ [blue arrow in Fig. IV.2(a)], which causes it to have a broad and significant contribution. Naturally, the modes used in Fig. IV.3(c) are the same as the ones for Fig. IV.3(a) since $m = 0$ in both cases. For the two cases in

Fig. IV.3(b,c) adding more QNMs (at least 20 in total) results in a good agreement with the "exact" calculation.

Now, without additional numerical computations, we can use this T-matrix to calculate the scattering properties of more complex structures composed of several nanorods with the help of the multipolar multiple-scattering theory [112–115, 169, 215]. All semi-analytical calculations obtained with a QNM expansion are the results of a two-steps procedure: first, the calculation of the T-matrix with a QNM expansion as shown in this section and secondly the multiple scattering calculation with the multipole method and the T-matrix of a single nanorod as an input parameter. For this second step, I have used a multipole method that was available at Laboratoire Charles Fabry.

2 Metallic nanorod dimer

As a first simple example let us consider scattering by a dimer that consists of two nanorods positioned on the same axis (see insets of Fig. IV.4). The nanorod dimensions, dispersion, and the surrounding medium index are the same as in the previous section, i.e., we use the same T-matrix here. The gap between the two faces of the nanorods is fixed to 25 nm. Figure IV.4 shows the scattering and absorption cross-sections of the dimer under plane wave illumination for normal and 45° incidence.

We compare the results obtained with the modal expansion of the T-matrix (degree $n = 5$, i.e., a 70×70 matrix) with those obtained with our in-house FEM code. The latter calculates directly the scattering by the dimer without using the T-matrix. We observe a good agreement with the FEM calculation for all cases. The discrepancy is higher for longer illumination wavelengths, as expected, since larger wavelength-to-gap ratios increase the high-order multipolar interaction between the nanorods, which requires more modes (or denser mesh for finite-difference methods) to accurately simulate. The closeness of the two results depend rather weakly on the number of QNMs, even though, as anticipated, additional modes provide better agreement.

We would like to emphasise that the T-matrix calculated semi-analytically with a single QNM of an isolated nanorod is sufficient for an accurate reconstruction of the two peaks in the dimer spectra for the oblique incidence. They correspond to the excitation of the symmetric and anti-symmetric modes of the dimer, which eigenfrequencies are different from the ones of a single nanorod. To illustrate this point, in Fig. IV.5 we plot the extinction cross-section calculated with two QNMs of

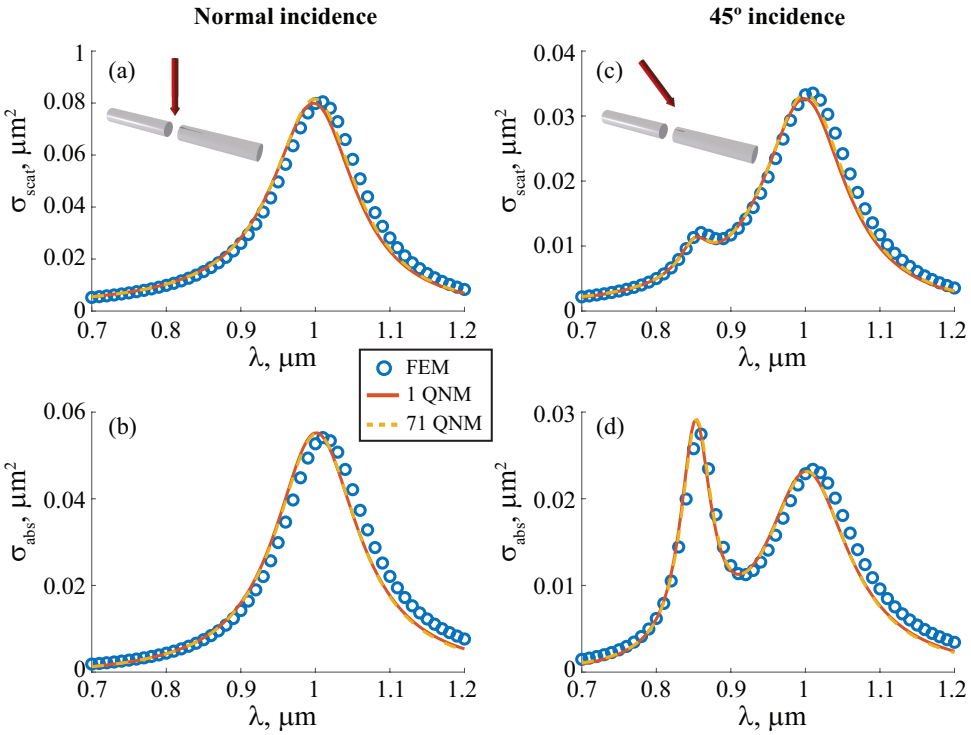

Figure IV.4.: (a-b) Scattering and absorption cross-sections of the dimer under normal plane wave illumination of wavelength λ. Blue circles indicate the FEM results; solid and dashed lines show the multipole multiple-scattering calculation using only the resonant and 71 QNMs of a single nanorod, respectively. (c-d) Same for the 45° incidence. The insets schematically depict the object and incident plane wave propagation vector. The T-matrix degree n is set to 5.

the dimer. The FEM and multiple-scattering theory (T-matrix reconstruction with the modes of a single nanorod) calculations are the same as in Fig. IV.4.

In the case of the normal incident plane wave, only one mode (symmetric) is excited. When the symmetry is broken by an oblique incidence, both modes are excited [see dashed curve in Fig. IV.5(b)], their sum providing the correct overall extinction.

Even though one individual rod mode provides a good agreement for this geometry, it is important to keep the rank of the T-matrix (and thus the multipolar degree in the multiple-scattering theory) high enough to correctly account for the interaction between the rods and the field enhancement in the gap. As mentioned above, the ED mode can have a non-zero contribution to high-order T-matrix elements T_{LP} such that L and P both correspond to $m = 0$. For instance, for this nanorod the main contribution of the principal mode is to $T_{4,4}$ as shown in Fig. IV.3. But the ED mode

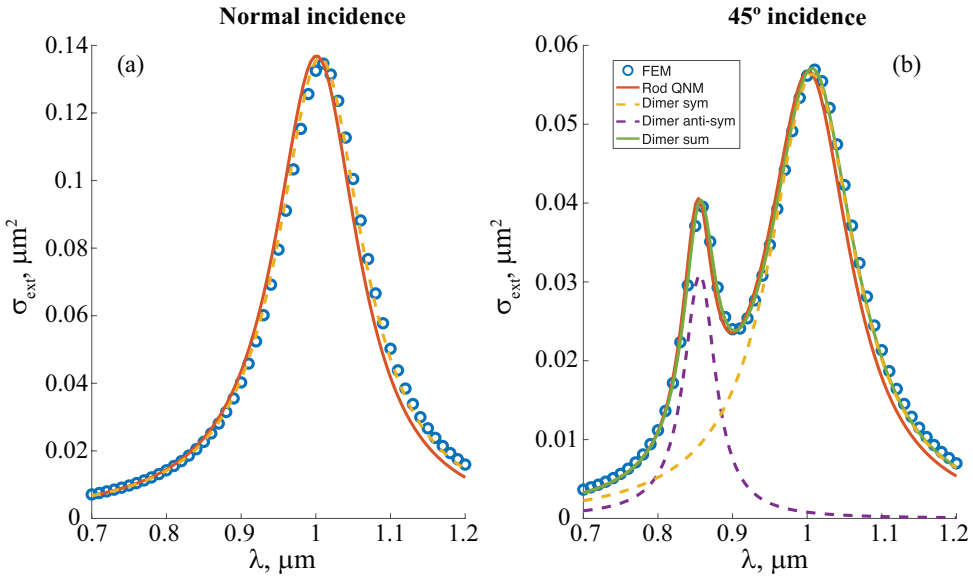

Figure IV.5.: Extinction cross-section of the same dimer as in Fig. IV.4 under normal and oblique (45°) plane wave (of wavelength λ) illumination for (a) and (b), respectively. Same line styles are kept across the two subfigues: blue circles indicate the FEM calculation results, solid red lines show the results of the T-matrix approach with the QNMs of the single nanorod, dashed lines show the contributions to the cross-section of the dimer QNMs, in contrast to the individual nanorod QNMs, solid green line is given by their sum.

has also a non-zero contribution to $T_{4,24} = T_{24,4}$ and $T_{24,24}$,[3] which are two and four orders of magnitude smaller, respectively.

It is worth being stressed that for the above figures the full (especially when the oblique incidence breaks symmetry of the system) FEM calculation had to be redone from scratch, when the incidence angle was changed. Whereas for the T-matrix-based calculations only the incidence parameter in the multipole multiple-scattering theory software had to be adjusted, which results in much faster calculations, as discussed in Sec. IV.5.

Our next step would be to add more nanorods to this dimer creating a Yagi-Uda inspired nanoantenna to further test the practical accuracy of the QNM T-matrix expansion.

[3] $L = 24$ stands for $n = 3$, $m = 0$, electric.

3 Yagi-Uda nanoantenna

In this section, we consider a very practical device – the Yagi-Uda antenna, which was relatively recently brought to the visible/infra-red world from the radio frequency domain [213]. The typical design is depicted in Fig. IV.6. The antenna can be divided into three sections: feed, reflector, director.

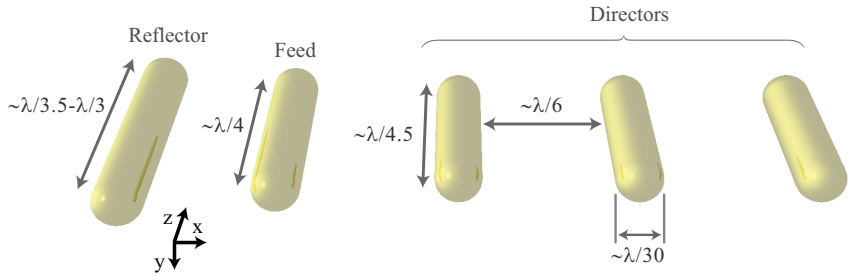

Figure IV.6.: Schematic of a typical Yagi-Uda nanoantenna design with metallic nanorods acting as the feed, reflector, and directors. Typical dimensions deduced from a rule of thumb are indicated.

In the heart of a typical Yagi-Uda antenna lies the feed component. In the original configuration it is electrically driven. In the visible and telecommunication ranges, it can be powered with a localised source (quantum emitter) [216, 217], polarisation selective incidence [218], focused beam [219], etc. In the simplest case, a physical feed element could be missing. Instead, a dipole or similar source would be present [113, 220, 221]. To the one side, at some distance d_{ref} from the feed, a reflective element is located. The reflector usually has a larger size than the feed, which enables its functionality. Its role is to reroute feed emission to the semi-space opposite from it, where a set of director elements is placed in order to channel the electromagnetic energy forward by constructive interference. The characteristic size of the individual director is typically smaller than the one of the feed and reflector. An important parameter is the distance d_{dir} between each neighbouring director. In some previous works, the distance between the feed and the first director was optimised individually while, in other works, it is taken equal to the distance d_{dir} between the directors. In the radio frequency domain $d_{\mathrm{ref}} < d_{\mathrm{dir}}$, which is not necessarily the optimal choice in nano-optics. The number of the director elements can go from one to more than ten, but usually the designs are optimised with three, being faithful to the original Yagi-Uda configuration [213]. The director elements can be identical to each other [113, 220–222], or gradually vary in size [223–225]. The latter kind is often referred to

as tapered nanoantenna [213]. The additional directors focus light increasingly more narrowly in the forward direction of the antenna, which can be undeniably helpful when it is pointed straight at the transmitter, but its performance will greatly decline for the signals coming from other directions.

The T-matrix approach combined with the multipolar multiple-scattering theory has a potential to provide significant gains to the Yagi-Uda antenna optimisation. Since most of the designs involve individual scatterers of two or three kinds, the time spent for the T-matrix calculation will be quickly made up when optimising for the distances between the elements. Potentially more so for tapered designs. In general, computing T-matrices with common rigorous methods (e.g., FEM) for a large number of non-spherical scatterers would require a CPU time too great to be compensated by the efficiency of the multipole theory. In the case of a tapered (gradient) antenna, the QNM approach has an additional advantage. For each new subantenna the complex QNM frequency can be found by an iterative search starting from a known value of a slightly bigger or smaller object, saving us the time needed for the search in the complex plane, which often takes the longest of all the steps, especially when we are clueless of the approximate values of the poles.

As for the restrictions that are imposed, there is a major one to consider when we deal with non-spherical building blocks. This has to do with the T-matrix method itself. As already discussed in Subsec. 1.1.a, the technique provides the scattered field outside an imaginary sphere that circumscribes the scattering elements. Because of that, we are limited in terms of how close we can bring them to each other or to a substrate, which might prohibit us from exploring some interesting options [226]. For instance, imagine we deal with two elongated rods with their axes parallel to each other. The minimal axis-to-axis distance between them would be slightly bigger than the average of their heights. Nevertheless, we are still left with a vast practical design range to explore.

3.1 Nanoantenna geometry

Since we are not faced with an objective to find the best performing Yagi-Uda design we can, we are going to simply build from what we have already introduced. The design studied in this section is schematically depicted in Fig. IV.7. The Yagi-Uda is known to provide a good directivity of the emission. However, it does not provide a strong enhancement (acceleration) of the spontaneous emission, except if we use as a feed a combined system: a dipole source plus a plasmonic nanoresonator

that emits like a dipole source [227]. Therefore, we use the dimer from the previous section as a feed. It is well-known that a point source in the middle of a dimer gap experiences a strong spontaneous emission enhancement [190, 228]. The triplet of the same nanorods positioned in parallel would make the director component. Finally, we choose a longer nanorod with $h = 175$ nm and the same radius $R = 15$ nm to act as a reflector. A similar design has been previously explored for surface enhanced Raman scattering applications [229]. In order to use the same QNMs and T-matrix as in Sec. IV.1, the index of the outside space $n_b = 1.5$.

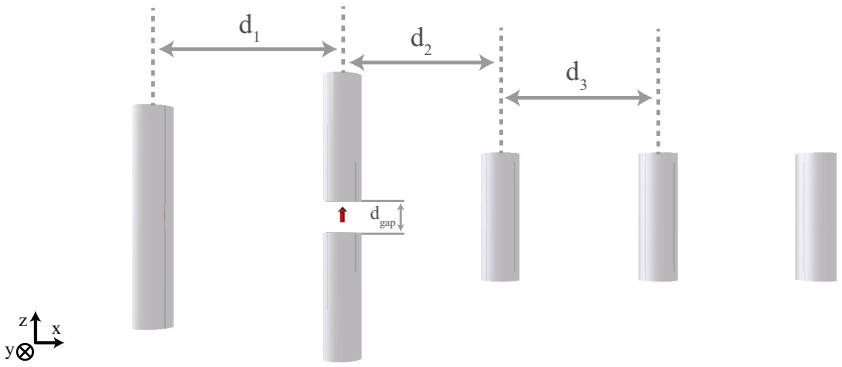

Figure IV.7.: Schematic of the considered Yagi-Uda nanoantenna. Feed dimer, along with the director component consist of the nanorods from Sec. IV.1. Refractive index of the surrounding space $n_b = 1.5$. The reflector element differs only in its length, which is chosen to be 175 nm. Labels used for distances are marked. Lengths in the horizontal direction are taken axis-to-axis.

In the following sections we are going to look at how different distances between the nanoantenna elements influence its performance as a directional emitter.

3.2 Purcell factor of a point source coupled to a dimer antenna

The Purcell effect is the modification of a quantum system's spontaneous emission rate by its environment, the magnitude of which is given by the Purcell factor [230]. As is often done in nano-optics, we define the Purcell factor as a ratio of the total power emitted by a dipole source in the presence of a scattering element to the one radiated in free space by the same source. In the case of a dimer antenna, Purcell factor generally increases as the gap width is decreased for a dipole source oriented along the axis, since the field enhancement is increased. The frequency of the peak enhancement will be the central operational frequency of the Yagi-Uda antenna. In

Fig. IV.8 we plot the Purcell factors versus the wavelength of the source for two values of the gap width, 25 and 50 nm, calculated using either QNM-derived T-matrix of a single rod or FEM. We also show the non-radiative power, i.e., the power absorbed in the nanorods. This in itself also serves as an illustrative test of the QNM calculation.

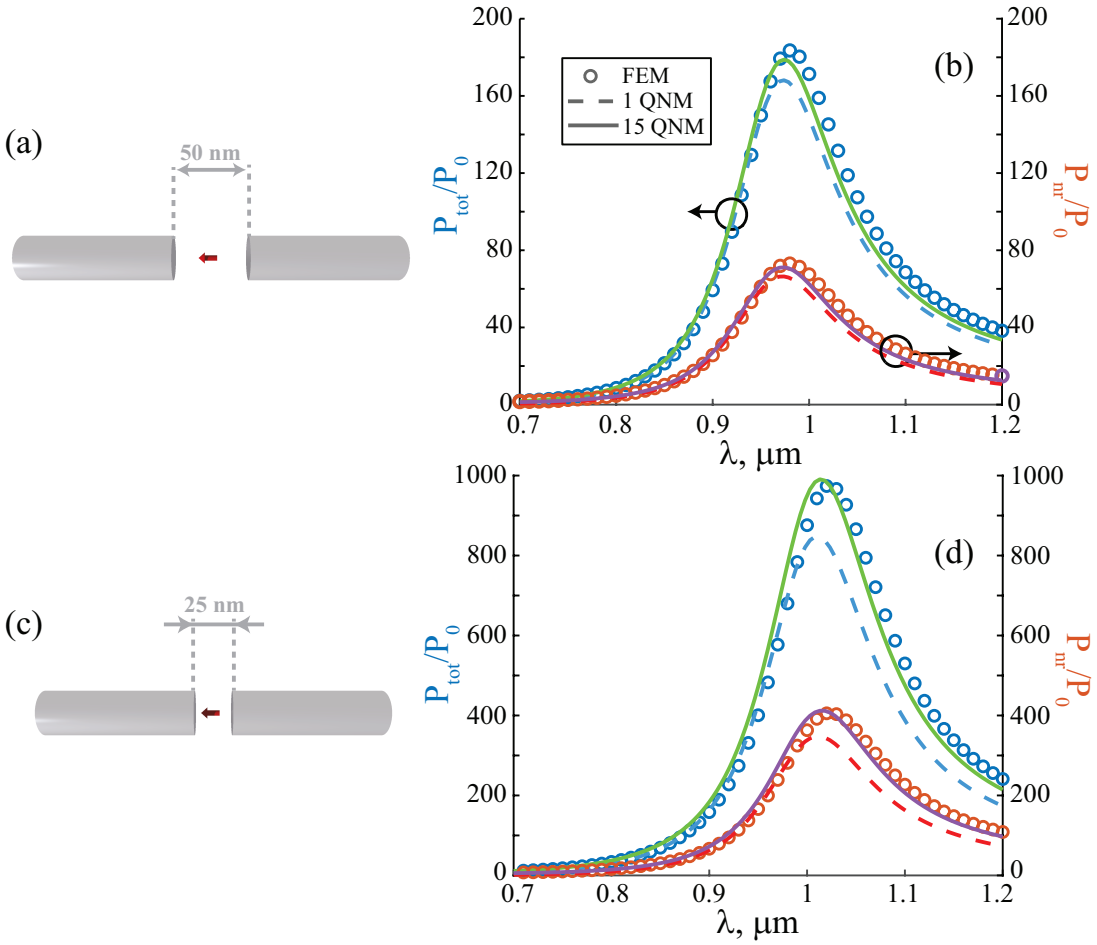

Figure IV.8.: (a) and (b) – Schematic of the dimer structure and its Purcell factor P_{tot}/P_0 for a gap value of 50 mn. P_{tot} is the total power emitted by the dipole source in the presence of the dimer and P_0 is the power emitted by the same source in a homogeneous medium of refractive index $n_b = 1.5$. (c) and (d) – similarly for the gap size of 25 mn. The dimer consists of two nanorods introduced in Sec. IV.1. In (b) and (d) circles mark the FEM calculation results, solid line – calculation with the nanorod T-matrix obtained with a single QNM mode (ED, indicated with the orange arrow in Fig. IV.2), dashed lines – with 15 QNMs, all of which correspond to $m = 0$. T-matrix degree $n = 10$.

Figure IV.8 tells us that the ED nanorod mode could be sufficient for an approximate value of the wavelengths corresponding to the highest Purcell factor, which is

given by the real part of the eigenfrequency of the ED mode. However, it proves inadequate to obtain the correct value of the maximum emission enhancement. What is more, as with the cross-section, the agreement is worse for longer wavelengths. Adding 14 additional QNMs helps to improve the agreement. More could potentially decrease the error even further, though it is more numerically challenging to calculate high-frequency QNMs. For this nanorod we have searched the space where $\mathrm{Re}(\tilde{k}) < 23\ \mu m^{-1}$.

For Fig. IV.8 it is worthwhile to include only QNMs with $m = 0$, as other are not excited with such a source. For a complete Yagi-Uda design, however, this is no longer the case due to multipolar interaction. Unlike in Sec. IV.2, here we use a higher degree for the T-matrix (principally it matters for the multipolar multi-scattering theory, as high-order T-matrix entries are very weak for our geometry) – $n = 10$, instead of $n = 5$. This improves the accuracy of the Purcell factor calculation. We will use the same degree for the Yagi-Uda calculations as well.

Even though the minimum gap size due to the aforementioned T-matrix constraints is $d_{\mathrm{gap}} \approx 4.5$ nm, we do not expect the calculations to be easy for the gap sizes of several nanometres. Two closely positioned nanorods pose a more complex problem for the QNM expansion based on the T-matrix of a single rod. Indeed, the interaction between two objects at a deep-subwavelength distance involves high-order multipoles, i.e., high-order T-matrix elements. The latter are, in most cases, non-resonant in the spectral range of interest and it is difficult to represent them accurately with a finite sum of modes. In such cases, it might be a better idea to use the QNMs of the dimer itself. Instead of using the multiple scatterer theory with two rods and a point source, we would use the analytic expression of the point source field as $\mathbf{E}_{\mathrm{inc}}(\mathbf{r}, \omega)$ for the integrals evaluation. However, it would not be possible to obtain the field inside or around the gap, as it would be in the centre of the circumscribing imaginary sphere. Also, the minimal d_1 and d_2 distances for our Yagi-Uda nanoantenna design would be larger if we were to use dimer T-matrix, instead of two T-matrices of individual nanorods. The discussion of these distances will be the subject of the ensuing subsection.

3.3 Optimisation of the geometry

This subsection is dedicated to the choice of some geometrical parameters for the Yagi-Uda design in Fig. IV.7.

The analytical nature of our combined approach QNM expansion + multipolar

multiple-scattering theory is extremely valuable to perform a fast parameter sweep to find the best directivity of the Yagi-Uda nanoantenna. The latter can be quantified with the front-to-back ratio, defined as the ratio between the power emitted forward in the positive x-direction to the power emitted backward (negative x-direction). Figure IV.9(a) displays the predicted values of the front-to-back ratio as a function of the distances d_1 and d_2 defined in Fig. IV.7. We have taken $d_2 = d_3$. The wavelength is chosen equal to 975 nm, where the spontaneous emission enhancement provided by the dimer is the highest. The optimum values for our configuration seem to be $d_1 \in [130, 150]$ nm and $d_2 \in [115, 130]$ nm. In contrast to a typical radio frequency Yagi-Uda antenna, our calculations show that $d_1 > d_2$ for an optimum Yagi-Uda antenna in the near infrared. The lower limits for d_1 and d_2 in Fig. IV.9(a) are fixed by the limitations of the T-matrix method.

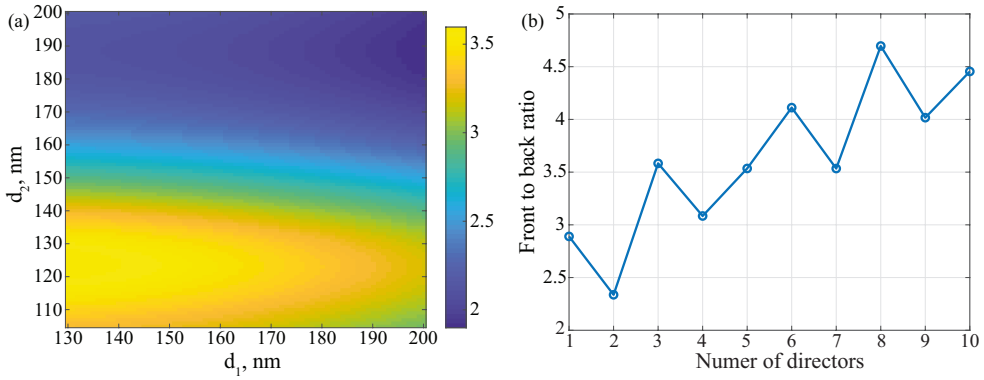

Figure IV.9.: (a) Front-to-back ratio as a function of d_1 and $d_2 = d_3$. (b) Front-to-back ratio as a function of the number of nanorods that act as directors. In (a) we use three director nanorods. In (b) d_1 and $d_2 = d_3$ are chosen according to the maximum in (a) – 130 and 125 nm, respectively. Dimer gap $d_{\text{gap}} = 50$ nm and point source wavelength $\lambda = 975$ nm for both subfigures.

Figure IV.9(b) shows the variation of the front-to-back ratio with the number of director nanorods. As expected, the general trend is such that the more of them there are, the better the directivity. This relation, however, is not monotonous, which is a manifestation of the interference nature of this effect.

The figure was computed with two different T-matrices, one for each kind of a nanorod: the 100 and 175 nm one. For the smaller one we have identified 71 QNMs (with $\text{Re}(\tilde{k}_m) < 23\ \mu m^{-1}$, plus their sister-modes with $-\tilde{k}_m^*$, as always), and for the bigger one – 53 (with $\text{Re}(\tilde{k}_m) < 30\ \mu m^{-1}$), for m up to 10. [4]

[4] As already mentioned, the modes cannot be automatically sorted by their degree n. Performing

Ultimately, we have chosen $d_1 = 150$ nm, $d_2 = d_3 = 125$ nm, and three director nanorods. It is possible that a better performance could be achieved with $d_2 \neq d_3$. Calculated radiation patterns of this configuration are presented in the ensuing subsection, along with direct FEM calculations.

3.4 Computation of the radiation pattern

The main characteristic of a Yagi-Uda nanoantenna is its directivity, i.e. a degree to which a radiation is concentrated in a preferred direction. In this section we look at how accurately our QNM-derived T-matrix can reconstruct the radiation pattern of the antenna sketched in Fig. IV.7. The radiation pattern shows the power radiated in the far field in an elementary solid angle $d\Omega$ around a direction fixed by the angles (θ, φ) of the spherical coordinates, normalised by the point source emission in free space. We show in Fig. IV.10 two cross-sections of the 3D radiation pattern. We compare the results obtained with the QNM expansion of the T-matrix and the multipole method with direct FEM calculations. In both cases, we calculate the near field around the antenna and use a near-to-far field transformation described in [231] to calculate the radiation pattern.

Figure IV.10 compares obtained radiation patterns. The reference rigorous calculation is, as before, provided with our in-house FEM code. For the T-matrix approach, we first use only seven principal QNMs (dashed curves): two for the smaller nanorod – the principal ED mode for $m = 0$ and the broad mode (also ED) for $m = 1$; five for the bigger nanorod – three modes for $m = 0$ (two that contribute principally to the T-matrix elements with $n = 1$, one to $n = 2$), and two for $m = 1$ (both $n = 1$) (see red-circled poles in Fig. IV.11). The threshold to include a given QNM was that its contribution is at least 1% of the dominant one. We would like to point out that, since the object is not a sphere, a QNM can have hybrid nature and contribute to different T elements, and vice-versa, distinct modes can contribute to the same resonance.

The solid curve in Fig. IV.10 shows the T-matrix-based results using 71 and 53 QNMs (up to $m = 10$) for the smaller and larger nanorod. Intriguingly, they are not so unambiguous. Clearly, for $d_{\text{gap}} = 50$ nm, adding additional modes leads to improved agreement, as anticipated. However, the situation seems to be flipped backwards for $d_{\text{gap}} = 25$ nm, where the calculation with more QNMs shows a larger error, when

QNM calculations for a given azimuthal number m means finding modes that will be excited y a VSH with $n \geq |m|$ of any of the two polarisations.

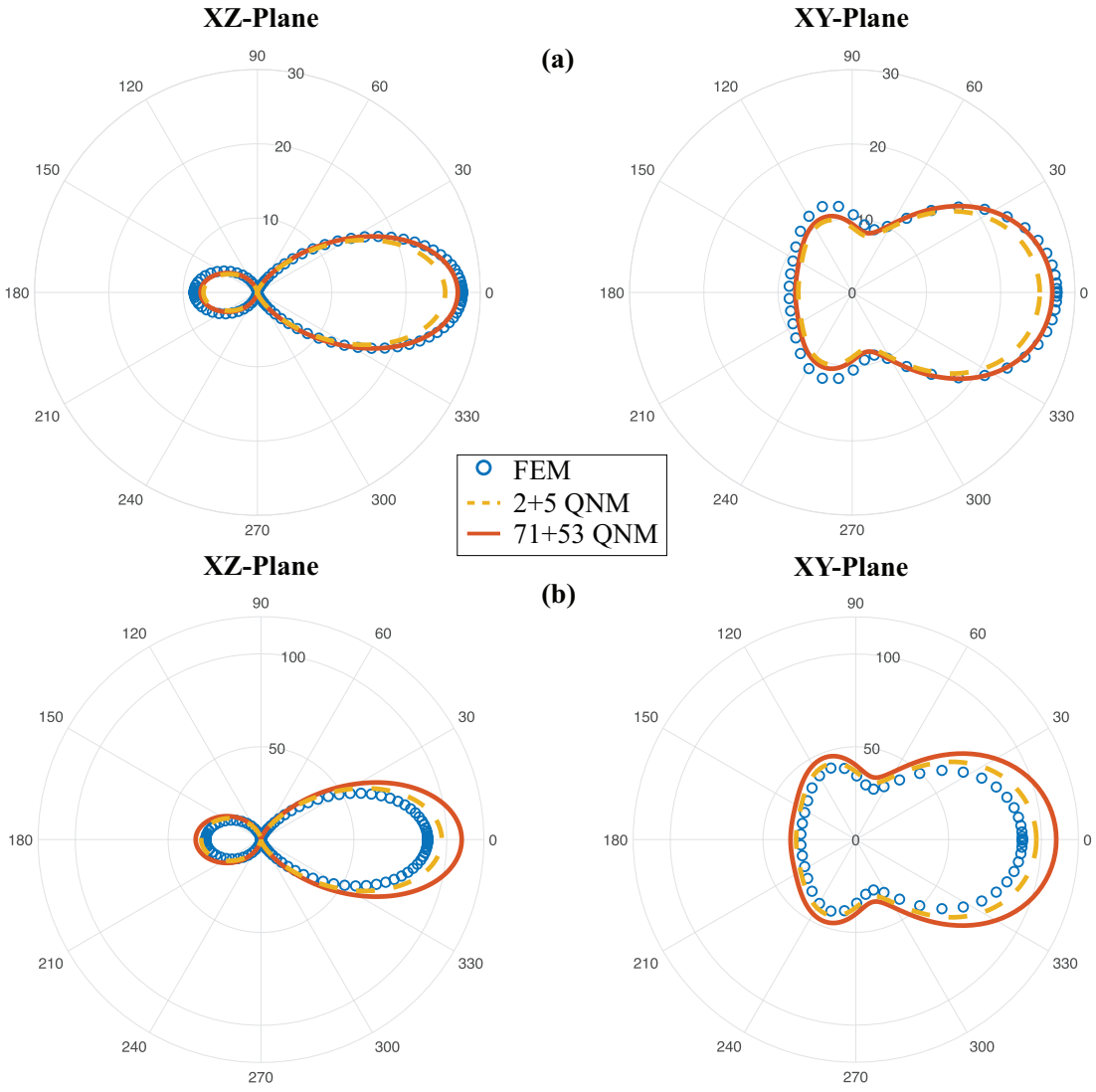

Figure IV.10.: Radiation pattern of the Yagi-Uda antenna with $d_{\text{gap}} = 25$ and 50 nm for (a) and (b), respectively. We plot two cross-sections of the 3D radiation pattern in polar coordinates in XZ (left) and XY (right) planes. Blue circles are obtained with a direct FEM calculation. The yellow dashed line is calculated with two T-matrices that describe both types of nanorods. They were approximated with only two QNMs for the smaller nanorod, five QNMs for the longer nanorod. Similarly, the red solid line is calculated with 71 and 53 QNMs for the smaller and longer nanorod, respectively. $n = 10$.

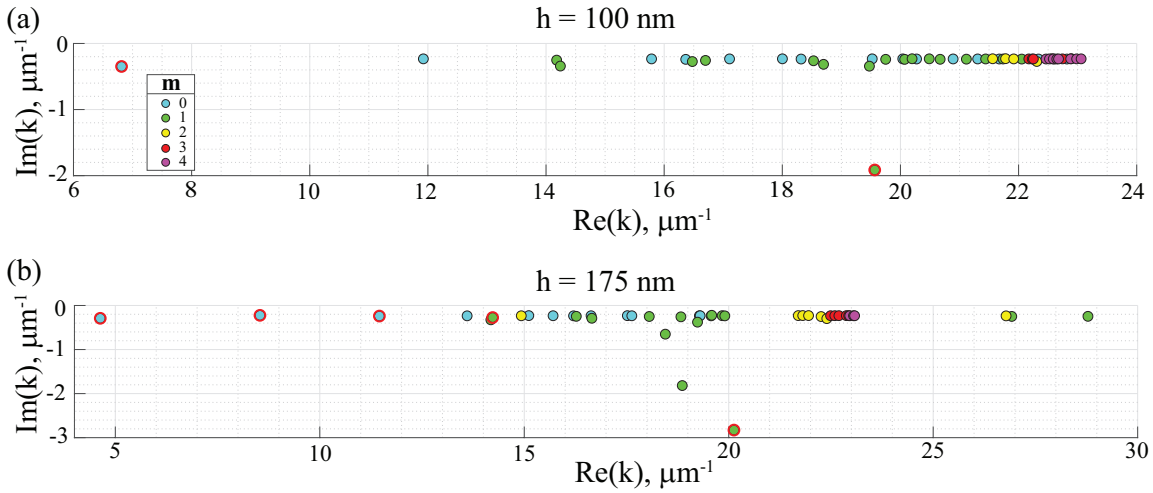

Figure IV.11.: Complex $\tilde{k}_m$ of found modes for the two nanorods of $h = 100$ nm and 175 nm, (a) and (b), respectively. Colour marks the m value in the pole search calculation. Red circles indicate the modes that have been used to calculate the yellow dashed line in Fig. IV.10.

compared to FEM. We suspect that this discrepancy is due to poor convergence for the high-frequency QNM fields calculation. This issue merits further studies.

Similar conclusions can be drawn from Fig. IV.10, as for Fig. IV.8: (i) the agreement is better for smaller sizes and (ii) a few QNMs that correspond to the principal nanorod resonances are adequate for an approximate radiation pattern reconstruction.

4 Periodic array

Finally, we look at the periodic array of nanorods, as an example metasurface. With only the nanorod T-matrix we are able to simulate the reflection, transmission, absorption, scattered fields, etc. of a periodic array. The structure is schematically depicted in Fig. IV.12. We have chosen $d_x = 150$, $d_y = 200$ to define the unit cell, with no prior parameter optimisation. These values give a typical unit cell to meta-atom characteristic size ratio.

Calculating a spectrum of such a metasurface is an easier task for our approximated T-matrix, as nanorods are quite distanced from each other, with no abrupt or localised features, like gaps, so the higher order multipole interaction is rather weak, or even negligible. For our chosen parameters, the gap between two neighbours in x-direction is 50 nm, same as in the studied dimer. Figure IV.13 shows the final results for

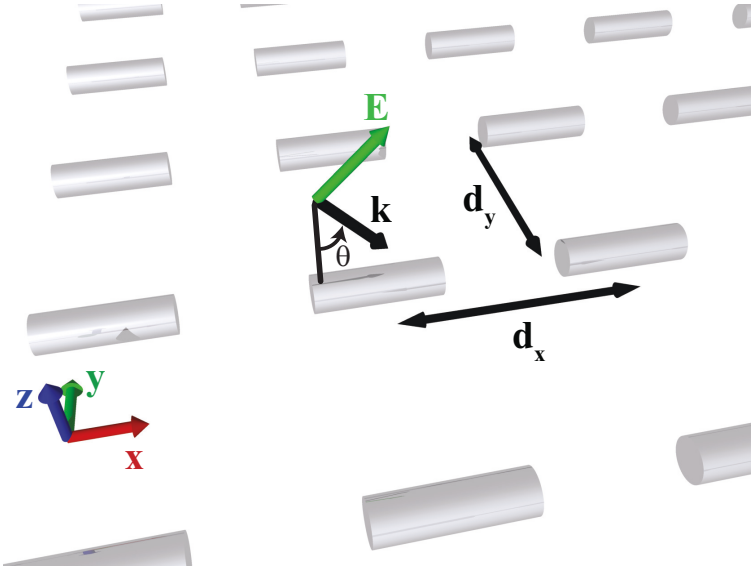

Figure IV.12.: Schematic of the periodic nanorod array. Dimensions of an individual nanorod are identical to the ones used in Sec. IV.1, $n_b = 1.5$. For normal incidence, the electric field **E** is aligned with the nanorod axis. The incidence angle θ is the angle between the vectors **k** and $\mathbf{u}_z$ in the (x, z) plane.

absorption of a metasurface from Fig. IV.12 under the normal and oblique (60°) incidence. T-matrix based calculations show an excellent agreement with the FEM. We can clearly see that the agreement is great and a single QNM T-matrix provides almost as good of a result, as the one with 51 QNMs (of different m up to 5, as the degree was fixed $n = 5$).

Figure IV.14 shows absorption in the same array as a function of θ for a fixed illumination plane wave wavelength $\lambda = 950$ nm. We can clearly see that the importance of additional QNMs increases with the angle.

5 Computational times

In this closing section let us discuss and compare computational times required by FEM and by the QNM expansion approach. This discussion, along with the time measurements, should only be used as an approximate order-of-value estimation, since they are highly sensitive to the QNM solver used and the parameter set for achieving converged results. This benchmark was performed on a desktop workstation with a 3.6 GHz Intel® Xeon® Gold 5122 CPU.

In the case of a point source or normal incidence, the FEM code leverages on the

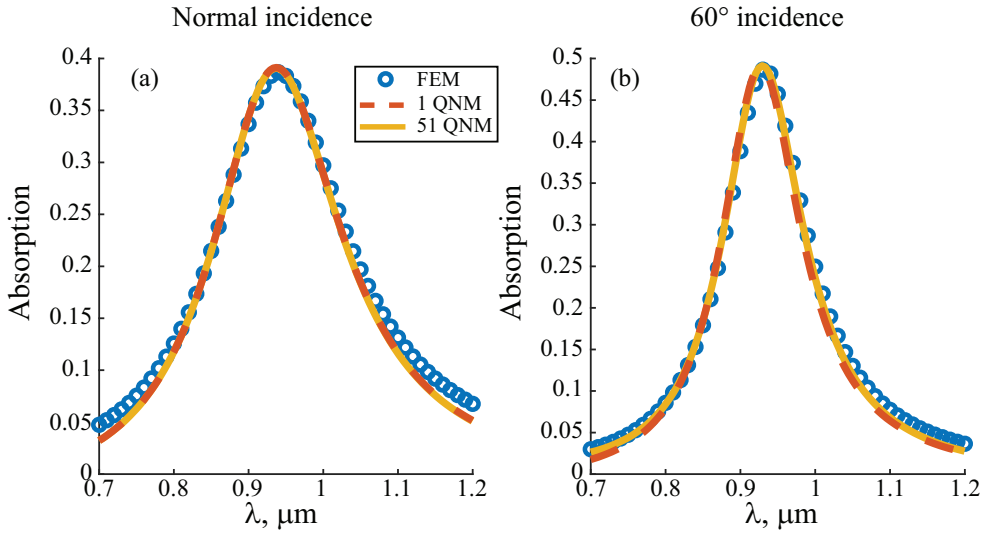

Figure IV.13.: Absorption of a 2D periodic array of metallic nanorods under the normal and oblique (60°) plane wave incidence, for (a) and (b), respectively. Circles are used to mark the FEM results, lines – multiple multi-scattering theory with the T-matrix calculated with one (dashed) or 51 (solid) QNMs. Degree $n = 5$, $d_x = 150$, $d_y = 200$.

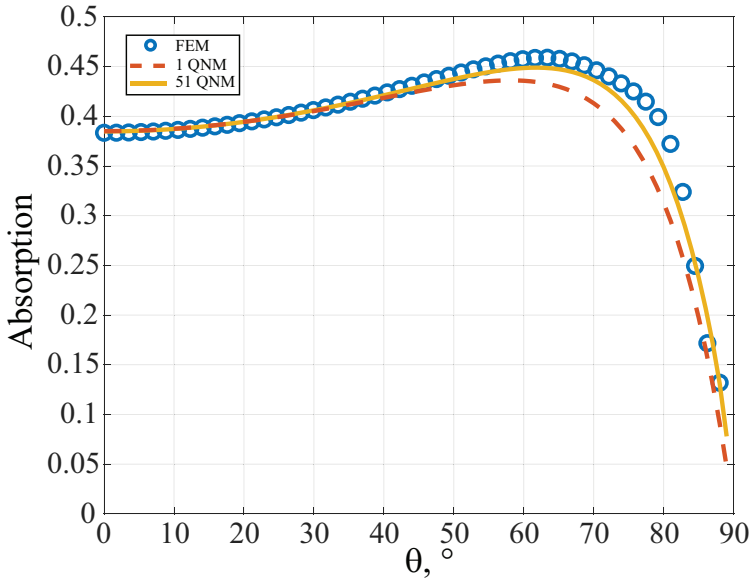

Figure IV.14.: Absorption of the 2D periodic array as a function of incidence angle θ for a fixed illumination plane wave wavelength $\lambda = 950$ nm. The notations and parameters are the same as Fig. IV.13.

symmetry of the structure with respect to y and z-planes, resulting in the need to mesh only one fourth of the structure. Taking symmetries into account provides a factor of 16 reduction in calculation time and memory requirements. For the oblique incidence the symmetry with respect to z-plane is broken, and we have to stimulate a half structure (factor of four gain). Typically, mesh calculations are not carried out on laptops due to high memory requirements. Indeed, the provided results for the Yagi-Uda antenna of Fig. IV.7 required up to 47 Gb of RAM accommodating $\sim$ 450 000 degrees of freedom[5] for the 25 nm gap configuration and $\sim$ 480 000 for the 50 nm gap. The increase is due to a larger overall structure size. This number will grow further, if more director nanorods are desired for a better directivity. For the periodic array of nanorods, the peak RAM usage was over 30 Gb (for half of the structure with almost 400 000 degrees of freedom). The QNM-based approach, on the other hand, has significantly lower memory requirements. Even if the modes are calculated with a FEM solver [157], the simulation domain is much smaller, as we have to consider only a single nanorod at a time. In addition, for cylindrical structures, numerical methods that take advantage of the rotational symmetry exist and can be used to decrease the CPU time and the memory requirements. This is the case of the aperiodic Fourier modal method that we are using [214].

Let us revisit the QNM-based routine steps, focusing on the time they take. Since we have used an iterative pole-search approach to calculate the QNM fields and frequencies, we need, at first, to find starting points (guess values) for the iterative calculation. Other QNM solvers that solve the non-linear eigenvalue problem exist [157]. In those cases, the mode calculation is done in a single step and can be faster when a large number of modes needs to be calculated.

1. Search in the complex plane for the approximate $\tilde{k}_m$ values. As already mentioned before, the step in real and imaginary k is a crucial value that can either help distinguish neighbouring modes, or add time with no additional benefits. In Fig. IV.15 we show two colour maps of the response (one S-matrix element, which is proportional to the field at the point of the exciting source) of the nanorod introduced in Sec. IV.1. In Fig. IV.15(a) using a relatively large step we are able to get five starting points, which later gave us four modes (second

[5]Degrees of freedom in the FEM context indicate points in the middle of a hexagon edge (in 3D). This way, one hexagon has 6 degrees of freedom. For the so-called elements of the second order, which better approximate the finite sums, this number goes up to 20 (each edge has two points that divide it into three equal segments, plus two degrees in for the each size in the centre of each hexagon face). Most of these degrees of freedom are shared between the neighbours. The rule of thumb is that their number grows by a factor slightly larger than 6 with the number of hexagonal elements.

one from the left appears to be a numerical artefact), in a bit over two minutes. When we decreased the step by a factor of four along the real axis, increasing the time requirement by the same factor, two faint peaks became more apparent. Just one of them later appeared to represent a real mode. Even though this step does not take a prohibitive amount of time, another option besides decreasing the step, would be to add more starting points manually in the vicinity of observed mode conglomeration. This is more useful for the higher m-values, when all the modes are gathered close together and the full complex plane sweep is not necessarily merited (see Fig. IV.2). Depending on the method used such a calculation might be needed to be conducted twice – once with an electric and once with magnetic source, in order to excite all the modes.

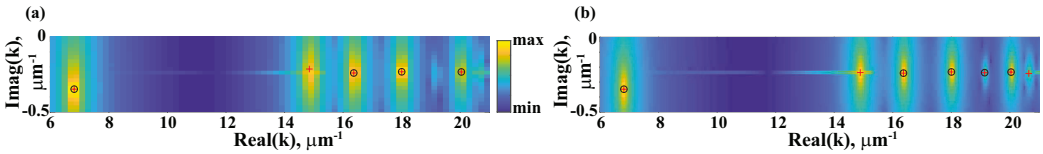

Figure IV.15.: Colour maps of the field response due to a closely located point source for 1596 and 6321 complex k's for (a) and (b), respectively. Starting points obtained taking advantage of the Cauchy integral theorem are marked with red plus signs, converged modes – with black circles.

2. Iterative calculation of the exact $\tilde{k}_m$ value, along with the fields take just a couple of seconds for each mode. The fields are obtained with the aperiodic-Fourier modal method [214].

3. With the studied nanorod example, along as with potentially many other, we verified that fixing $n = 5$ is enough for a good numerical accuracy. This leads to T-matrix size of 70×70. It takes a bit over a second to calculate the T-matrix of this size for one value of k_0 with one mode, and the time increases quite slowly with the number of modes. However, for some cases (Figs.IV.8 and IV.10) it was proven helpful increasing the degree to 10 of the multipole multiple-scattering theory. This is why for our calculations we have taken $n = 10$, which meanT-matrix size of 240×240 and took 3-4 seconds for each k_0. Numerically, the values of T for $n > 5$ are so small, that they might as well be zero.

4. Multipole multiple-scattering theory computation thanks to its analyticity takes just around 14 seconds for $n = 10$ (and only about 3 s for $n = 5$) regardless of the gap size for the Yagi-Uda geometry, and a bit over 6 seconds (4-5 s for $n = 5$) for the periodic array, for a single k_0 and incidence angle.

For completeness, we would like to mention that the numerical T-matrix calculation mentioned in Subsec. IV.1.2 takes around 100 s for a single k_0 to achieve results of comparable or better accuracy (notably for dimer cross-sections and periodic arrays) than the ones of the QNM-derived T-matrix. However, poor convergence, especially for the higher order elements, could lead to incorrect predictions for more complex and demanding setups (gap source excitation). A good convergence has to be ensured, which could blow up the time requirements by a factor of 10 or more.

We note that for some steps (complex plane search and any calculation for different k_0's) it is possible to distribute the for-loops computations using, for instance, built-in parallel tools of MatLab, thanks to the low memory requirements of the analytical steps and shared numerically pre-computed data. With four workers working in parallel the computational time decreases almost by a factor of four.[6]

To sum up, in practice, when calculating several poles for multiple m's, this first step can take anywhere from several minutes to hours, depending on the implementation details and object spectral properties. However, this, along with the following step of getting the $\tilde{\mathbf{E}}_m$'s needs to be done only once for a single geometry to be used with any excitation field type, angle, or frequency.

For comparison, a scattering problem for a given oblique incidence and a single wavelength is solved with FEM in our realisation in ~ 700 and ~ 850 seconds for the Yagi-Uda antenna with a 25 and 50 nm dimer gap, respectively, and ~ 900 seconds for the periodic arrangement of nanorods. For normal incidence, the simulation domain can be reduced by a factor 2 because of symmetry reasons (from a half structure to a quarter) and the time of the computation decreases by a factor of 4.

6 Conclusion

To sum up this chapter, we have demonstrated that QNM expansion of an individual scatterer T-matrix combined with the multipolar multiple-scattering theory is a viable solution for accurate and efficient modelling of complex ensembles of optical nanoresonators. The gains in CPU time are especially favourable for optimisation problems where a large number (often into several thousands) of simulations has to be performed.

We have shown that for a typical periodic reflector/absorber array configuration,

[6] The workstation used for the measurements in this section has two CPUs. When the distributed for-loop (parfor in Matlab) was used on a laptop with a single CPU, the gain was half that – a bit under a factor of two.

a minimal number of QNMs is sufficient due to a period size comparable to the meta-atom characteristic length. For more closely packed localised nanostructures, additional modes, especially those contributing to the T-matrix elements with a large degree n, gradually improve the accuracy.

The multipolar multiple-scattering theory is a powerful analytical tool for the modelling of multi-element nanoantennas, ensembles, and clusters of nanoparticles, or metalattices. The main difficulty is calculation of an individual element, nanoparticle, or meta-atom T-matrix. Analytical solutions exist only for a homogeneous (or a layered core-shell) spheres and infinite rods. A rigorous T-matrix calculation for an arbitrary shaped object would take a significant amount of time, even though it has to be done only once for a single excitation wavelength to be later used with any field. Performing the QNM expansion of the T-matrix aims to render this calculation semi-analytical with respect to the wavelength, meaning that only the QNM calculation (which has to be performed only once for a given geometry in a given spectrum band) is numerical, subsequent T-matrix computations are analytical.

Rigorous methods, like FEM, require new full computation for any new modification of the geometry or excitation parameters. Even though for a single fixed set of parameters the calculation of a complex structure spectrum could be done in a reasonable amount of time, the hybrid approach described in this and previous chapters provides significant computational gains for multiple illumination and geometry optimisation (distances between scatterers, rather than their size) problems.

Conclusion

In conclusion, this thesis explored the use of semi-analytical approaches for solving the scattering problem in resonant nanophotonics. Three different cases were considered: (i) infinite periodic 1D photonic crystal slabs, whose period is of the order of the wavelength, and which can support resonances with high quality factors; (ii) ensembles composed of several plasmonic nanoresonators, which exhibit resonances with low quality factors; (iii) infinite periodic arrays of such subwavelength nanoresonators.

We have first presented a multimode Fabry-Perot model for the calculation of the leaky modes supported by a PhC slab (their dispersion and quality factors). We have used this semi-analytical model to study bound states in the continuum. Since these peculiar states are created by an interference mechanism inside the slab, the thickness of a PhC slab is an important parameter that determines the existence of BICs. It is also the parameter that the model is analytical with respect to. As a result, one is able, with no additional numerical calculations, to change its value and re-calculate the dispersion and quality factors of the PhC modes, showing the Q-factor variation with h. This, in particular allows us to quickly determine for which values of h a symmetry-protected BIC will become resonance-trapped, when we move away from the Γ-point in the dispersion diagram. We can also find regions in the parameter space, where Q-factors are very high. This might be useful for practical applications. In addition, the modal nature of the approach gives some additional physical insight into the composition of a PhC mode and determine a frequency cut-off beyond which no BICs can exist, regardless of the slab thickness.

We have also developed a modal theory to solve light scattering problems by complex structures composed of small ensembles or periodic arrays (metasurfaces) of plasmonic nanoresonators. The described approach allows us to model light scattering by metasurfaces from the sole knowledge of the eigenmodes of their individual constituents. We have combined a quasi-normal mode (QNM) formalism with the multipole multiple-scattering theory based on the T-matrix of a single scatterer. We have shown that often one or a few QNMs are sufficient to achieve a good accuracy for the reconstruction of the T-matrix itself, and thus for the reconstruction of important physical quantities, like cross-sections, absorption, radiation pattern, etc. This approach provides significant computational gains, when compared to fully numerical

rigorous methods such as a Maxwell's equation solver on a discrete mesh (FEM).

Though both the field-based and the current-based formulations of the T-matrix modal expansion provide accurate results, they do not converge with the same speed. The current-based formulation provides a smaller error for a small number of modes. However, its predictions seem to converge towards an incorrect value. This issue, which is probably related to the choice of the non-resonant term in the modal expansion, deserves further studies.

Finally, we would like to put in words a link between the two parts of the thesis: the study of BICs in PhC slabs and the use of quasi-normal modes. In the second part, we have calculated rigorously the eigenmodes of a resonant object and used them to calculate its optical properties. On the other hand, in the first part, we have developed an approximate model to calculate the eigenmodes of a resonant object. Clearly, the leaky modes of a PhC slab that we have studied in the first part are the quasi-normal modes of the PhC slab. With this in mind, it could be interesting to revisit the theory of BICs with the QNM formalism. Since a BIC is a true guided mode, it is a QNM with a purely real eigenfrequency. Moreover, since a BIC cannot couple to an incident plane wave, the coupling coefficient $\alpha(\omega)$ of the QNM should vanish at the BIC position. The cancellation of the excitation coefficient is probably due to particular symmetries of the mode profile. The study of BICs with the QNM formalism could then provide useful insight into the field profile of a BIC.

Appendix A

Derivations of the effective reflection coefficients

1 Effective coefficients for $N = 2$ waves

This Appendix section provides the steps to derive the effective reflectivity coefficient that takes into account the interference of two Bloch waves (BWs), when the two sets of BW reflection coefficients are different for the two interfaces (e.g. substrate or a stratum preset). The procedure follows Ref. [159]. A mode propagating upward (positive z-direction) is reflected at the top interface (indicated with superscript T) into the same mode with reflection coefficients either r_{11} or r_{22}, or cross-reflected as the other one, with r_{12} or r_{21}, accordingly:

$$\begin{aligned} u_1^+ &= r_{11}^T u_1^- \exp(i\beta_1 h) + r_{21}^T u_2^- \exp(i\beta_2 h), \\ u_2^+ &= r_{12}^T u_1^- \exp(i\beta_1 h) + r_{22}^T u_2^- \exp(i\beta_2 h), \end{aligned} \tag{A.1}$$

where $u_i^{+(-)}$ is the amplitude of the upward (downward) propagating i^{th} BW, β_i – its propagation constant. An almost identical pair of equations is to be written down additionally, exchanging plus and minus signs for the amplitudes and substituting the superscript T with B to mark a coefficient for the bottom interface. The values of β_i's and r_{ij}'s are calculated using rigorous coupled wave analysis (RCWA) [123, 215] individually for each interface to get the sets of r^T's and r^B's. BWs propagation constants do not depend on the outside space index, only on the periodicity conditions.

In matrix terms, Eqs. (A.1) can be rewritten in the form

$$\mathbf{R}(k_x, \lambda)\mathbf{U} = 0, \tag{A.2}$$

where $\mathbf{U} = [u_1^+, u_1^-, u_2^+, u_2^-]^T$, and the matrix $\mathbf{R}(k_x, \lambda)$ contains all reflections and cross-reflection coefficients. The mathematical challenge is now bring the matrix $\mathbf{R}$

to the following form:

$$\begin{pmatrix} 1 & 0 & & \\ 0 & 1 & \multicolumn{2}{c}{\mathbf{M}} \\ 0 & 0 & r_{\text{eff}}^{(12),B}\exp(i\beta_2 h) & -1 \\ 0 & 0 & -1 & r_{\text{eff}}^{(12),T}\exp(i\beta_2 h) \end{pmatrix}, \tag{A.3}$$

so that its determinant yields the Fabry-Perot resonance condition:

$$1 - r_{\text{eff}}^{(12),B} r_{\text{eff}}^{(12),T}\exp(2i\beta_2 h) = 0, \tag{A.4}$$

where we have introduce an effective reflectivity that takes into account all the interferences in the system:

$$\begin{aligned} u_2^- &= r_{\text{eff}}^{(12),B} u_2^+ \exp(i\beta_2 h), \\ u_2^+ &= r_{\text{eff}}^{(12),T} u_2^- \exp(i\beta_2 h), \end{aligned} \tag{A.5}$$

with

$$r_{\text{eff}}^{(12),T} = \frac{r_{22}^T + \alpha r_{11}^B r_{21}^T r_{12}^T \exp(2i\beta_1 h)}{1 - \alpha r_{21}^T r_{12}^B \exp\left[i(\beta_1+\beta_2)h\right]}, \tag{A.6}$$

$\alpha = \left[1 - r_{11}^T r_{11}^B \exp(2i\beta_1 h)\right]^{-1}$. $\mathbf{M}$ in Eq. (A.3) is some 2×2 matrix that does not impact the determinant. The expression for $r_{\text{eff}}^{(12),B}$ is trivially obtained by interchanging subscripts T and B.

2 Effective coefficients for $N = 3$ waves

In a perfectly similar fashion, the task of deriving closed-form expressions for $r_{\text{eff}}^{(123)}$ (for simplicity we assume equal refractive indices from both sides; derivation can be straightforwardly modified if it is not the case) boils down to transforming a 6×6 $\mathbf{R}$ matrix from

$$\mathbf{R} = \begin{pmatrix} r_{11}\exp(i\beta_1 h) & -1 & r_{21}\exp(i\beta_2 h) & 0 & r_{31}\exp(i\beta_3 h) & 0 \\ -1 & r_{11}\exp(i\beta_1 h) & 0 & r_{21}\exp(i\beta_2 h) & 0 & r_{31}\exp(i\beta_3 h) \\ r_{12}\exp(i\beta_1 h) & 0 & r_{22}\exp(i\beta_2 h) & -1 & r_{32}\exp(i\beta_3 h) & 0 \\ 0 & r_{12}\exp(i\beta_1 h) & -1 & r_{22}\exp(i\beta_2 h) & 0 & r_{32}\exp(i\beta_3 h) \\ r_{13}\exp(i\beta_1 h) & 0 & r_{23}\exp(i\beta_2 h) & 0 & r_{33}\exp(i\beta_3 h) & -1 \\ 0 & r_{13}\exp(i\beta_1 h) & 0 & r_{23}\exp(i\beta_2 h) & -1 & r_{31}\exp(i\beta_3 h) \end{pmatrix} \tag{A.7}$$

to

$$\mathbf{R} = \left[\begin{array}{cc|cc|cc} 1 & 0 & \multicolumn{2}{c|}{\multirow{2}{*}{$\mathbf{M}$}} & \multicolumn{2}{c}{\multirow{2}{*}{$\mathbf{N}$}} \\ 0 & 1 & & & & \\ \hline 0 & 0 & 1 & 0 & \multicolumn{2}{c}{\multirow{2}{*}{$\mathbf{P}$}} \\ 0 & 0 & 0 & 1 & & \\ \hline 0 & 0 & 0 & 0 & $r_{\text{eff}}^{(123)} \exp(i\beta_3 h)$ & -1 \\ 0 & 0 & 0 & 0 & -1 & $r_{\text{eff}}^{(123)} \exp(i\beta_3 h)$ \end{array}\right], \tag{A.8}$$

where $\mathbf{M}, \mathbf{N}, \mathbf{P}$ are some 2×2 matrices that do not impact the determinant. After the required algebraic transformations, we arrive at Eq. (II.18).

Here we have derived $r_{\text{eff}}^{(123)}$ considering BW 3 as the dominant one. Similarly it can (and sometimes should, as discussed Section II.6) be done with the second BW as the dominant one. In order to update the equations, indices 2 and 3 have to simply be interchanged.

Appendix B

Definition of the vectorial spherical harmonics

This appendix section gives the explicit form of the vectorial spherical harmonics (VSH) as implemented in the Reticolo software package [215] used for this thesis. The main parameters are

- ϵ, μ – media permittivity and permeability, respectively
- $n_0 = \sqrt{\epsilon\mu}$ – refractive index
- $Z_0 = \sqrt{\frac{\mu_0}{\varepsilon_0}}$ – free-space impedance, μ_0 and ε_0 are free-space permeability and permittivity, respectively
- k – wavenumber
- n, m – degree and azimuthal number
- r, θ, φ – radial distance, polar, and azimuthal angles, respectively, as commonly defined in the spherical coordinate system

Define:

$$\mathrm{Fac} = k\,(\sqrt{n_0})^p\,\sqrt{(-1)^m}\sqrt{\frac{2}{n(n+1)}}\mathrm{e}^{im\varphi}, \tag{B.1}$$

where $p = 1$ for electric and -1 for magnetic. Then, the VSH are as follows:

$$\mathbf{M}^{\pm}_{n,m} = \begin{bmatrix} \left(\mathbf{M}^{\pm}_{n,m}\right)_r \\ \left(\mathbf{M}^{\pm}_{n,m}\right)_\theta \\ \left(\mathbf{M}^{\pm}_{n,m}\right)_\varphi \end{bmatrix} = \frac{-i}{\sqrt{Z_0}}\,\mathrm{Fac}\cdot\begin{bmatrix} 0 \\ ih^{\pm}_n(kr)\hat{\pi}^m_n(\theta) \\ -h^{\pm}_n(kr)\hat{\tau}^m_n(\theta) \end{bmatrix}, \tag{B.2}$$

$$\mathbf{N}^{\pm}_{n,m} = \begin{bmatrix} \left(\mathbf{N}^{\pm}_{n,m}\right)_r \\ \left(\mathbf{N}^{\pm}_{n,m}\right)_\theta \\ \left(\mathbf{N}^{\pm}_{n,m}\right)_\varphi \end{bmatrix} = \sqrt{Z_0}\,\mathrm{Fac}\cdot\begin{bmatrix} n(n+1)\frac{h^{\pm}_n(kr)}{\epsilon r}\hat{P}^m_n(\cos\theta) \\ \frac{\sigma^{\pm}_n(kr)}{\epsilon r}\hat{\tau}^m_n(\theta) \\ i\frac{\sigma^{\pm}_n(kr)}{\epsilon r}\hat{\pi}^m_n(\theta) \end{bmatrix}, \tag{B.3}$$

where the normalised Legendre functions are

$$\begin{cases} \hat{P}_n^m(\theta) &= \gamma_{nm} P_n^m(\cos\theta), & \hat{P}_n^{-m}(\theta) &= (-1)^m \hat{P}_n^m(\theta), \\ \hat{\tau}_n^m(\theta) &= \gamma_{nm} \tau_n^m(\theta), & \hat{\tau}_n^{-m}(\theta) &= (-1)^m \hat{\tau}_n^m(\theta), \\ \hat{\pi}_n^m(\theta) &= \gamma_{nm} \pi_n^m(\theta), & \hat{\pi}_n^{-m}(\theta) &= (-1)^{m+1} \hat{\pi}_n^m(\theta), \end{cases} \tag{B.4}$$

with the normalisation factor $\gamma_{nm} = \sqrt{\frac{(2n+1)(n-m)!}{4\pi(n+m)!}}$,

$$P_n^m(x) = \frac{(-1)^m}{2^n n!} \left(1-x^2\right)^{\frac{m}{2}} \frac{\mathrm{d}^{m+n}}{\mathrm{d}x^{m+n}} \left(x^2-1\right)^n \tag{B.5}$$

being the associated Legendre polynomial,

$$\tau_n^m(\theta) = \frac{\mathrm{d}P_n^m(\cos\theta)}{\mathrm{d}\theta}, \tag{B.6}$$

$$\pi_n^m(\theta) = m\frac{P_n^m(\cos\theta)}{\sin\theta}, \tag{B.7}$$

$h_n^{\pm}(r) = \sqrt{\frac{\pi}{2r}} H_{n+\frac{1}{2}}^{\pm}(r)$ – spherical Hankel functions, $\sigma_n^{\pm}(r) = \frac{\mathrm{d}}{\mathrm{d}r}(r h_n^{\pm})$.

Appendix C

Lorentz reciprocity formula

This Appendix comments on the derivation steps of the Lorentz reciprocity formula. It lies in the foundation of the T-matrix calculations in this thesis. It relates two pairs of fields, both solutions to the time-harmonic Maxwell's equations, $\{\mathbf{E}_1, \mathbf{H}_1\}$ and $\{\mathbf{E}_2, \mathbf{H}_2\}$, taken with their respective frequencies, (ω_1, ω_2), and driving currents, $(\mathbf{J}_1, \mathbf{J}_2)$:

$$\nabla \times \mathbf{E}_i = i\omega_i \mu(\mathbf{r}, \omega_i)\mathbf{H}_i, \tag{C.1}$$

$$\nabla \times \mathbf{H}_i = -i\omega_i \epsilon(\mathbf{r}, \omega_i)\mathbf{E}_i + \mathbf{J}_i(\mathbf{r}, \omega_i), \tag{C.2}$$

where $i = 1, 2$, $\epsilon(\mathbf{r}, \omega)$ gives the permittivity distribution in the whole space, namely, it is equal to the material dispersion inside a scatterer, and to the background permittivity (usually constant) outside. The time convention $\exp(-i\omega t)$ is used.

Let us define 'Lorentz product' the following way

$$\mathbf{\Psi}_1 \otimes \mathbf{\Psi}_2 \equiv \iint (\mathbf{E}_2 \times \mathbf{H}_1 - \mathbf{E}_1 \times \mathbf{H}_2)\, \mathrm{d}\mathbf{S}, \tag{C.3}$$

where $\mathbf{\Psi}_i = \{\mathbf{E}_i, \mathbf{H}_i\}$, vector $\mathbf{S}$ defines a closed surface. According to the divergence theorem, this integral is equivalent to

$$\mathbf{\Psi}_1 \otimes \mathbf{\Psi}_2 = \iiint \nabla \cdot (\mathbf{E}_2 \times \mathbf{H}_1 - \mathbf{E}_1 \times \mathbf{H}_2)\, \mathrm{d}V, \tag{C.4}$$

where the integration volume V is the one enclosed by S. The integrand can be expanded using the vector identity $\nabla \cdot (\mathbf{E} \times \mathbf{H}) = \mathbf{H} \cdot (\nabla \times \mathbf{E}) - \mathbf{E} \cdot (\nabla \times \mathbf{H})$, giving

$$\mathbf{\Psi}_1 \otimes \mathbf{\Psi}_2 = \iiint \mathbf{H}_1 \cdot (\nabla \times \mathbf{E}_2) - \mathbf{H}_2 \cdot (\nabla \times \mathbf{E}_1) - \mathbf{E}_2 \cdot (\nabla \times \mathbf{H}_1) + \mathbf{E}_1 \cdot (\nabla \times \mathbf{H}_2)\, \mathrm{d}V. \tag{C.5}$$

Finally, upon substituting the curls of the fields according to the Maxwell's equations

and grouping the terms, we arrive at the Lorentz reciprocity formula

$$\begin{aligned}\boldsymbol{\Psi}_1 \otimes \boldsymbol{\Psi}_2 = &\iiint [\mathbf{J}_2 \cdot \mathbf{E}_1 - \mathbf{J}_1 \cdot \mathbf{E}_2] \, \mathrm{d}V \\ &+ i \iiint \{\mathbf{E}_1 \cdot [\omega_1 \epsilon(\omega_1) - \omega_2 \epsilon(\omega_2)] \cdot \mathbf{E}_2 - \mathbf{H}_1 \cdot [\omega_1 \mu \omega_1) - \omega_2 \mu(\omega_2)] \cdot \mathbf{H}_2\} \, \mathrm{d}V. \quad \text{(C.6)}\end{aligned}$$

Appendix D

Scattered field formulation

This Appendix section introduces the scattered field Maxwell's equations used in Chapter III.

At the absence of a scattering object, the Maxwell's equations simply describe a propagation of the wave, generated by the source, which is the incident wave in the problem:

$$\nabla \times \mathbf{E}_b = i\omega\mu(\mathbf{r},\omega)\mathbf{H}_b, \tag{D.1}$$

$$\nabla \times \mathbf{H}_b = -i\omega\epsilon_b(\mathbf{r},\omega)\mathbf{E}_b + \mathbf{J}(\mathbf{r},\omega), \tag{D.2}$$

where $\mathbf{E}_b$ and $\mathbf{H}_b$ are the electric and magnetic 'background' fields, meaning in the surrounding medium only, and $\mathbf{J}$ is the source term. Taking a point source, located far away from a point $\mathbf{r}$, is a common way of generating a plane wave in the region around said point. In the presence of a scattering media characterised by permittivity $\epsilon(\mathbf{r},\omega)$ and permeability $\mu(\mathbf{r},\omega)$, Maxwell's equations are satisfied with the total fields $(\mathbf{E},\mathbf{H})$ and the same source term $\mathbf{J}(\mathbf{r},\omega)$:

$$\nabla \times \mathbf{E} = i\omega\mu(\mathbf{r},\omega)\mathbf{H}, \tag{D.3}$$

$$\nabla \times \mathbf{H} = -i\omega\epsilon(\mathbf{r},\omega)\mathbf{E} + \mathbf{J}(\mathbf{r},\omega). \tag{D.4}$$

The scattered field simply defined as the difference $(\mathbf{E}_s,\mathbf{H}_s) = (\mathbf{E},\mathbf{H}) - (\mathbf{E}_b,\mathbf{H}_b)$ has to satisfy

$$\nabla \times \mathbf{E}_s = i\omega\mu(\mathbf{r},\omega)\mathbf{H}_s, \tag{D.5}$$

$$\nabla \times \mathbf{H}_s = -i\omega\epsilon(\mathbf{r},\omega)\mathbf{E}_s - i\omega\Delta\epsilon(\mathbf{r},\omega)\mathbf{E}_b(\mathbf{r}), \tag{D.6}$$

with $\Delta\epsilon(\mathbf{r},\omega) = \epsilon(\mathbf{r},\omega) - \epsilon_b(\mathbf{r},\omega)$. These equations give us the scattered field in the region, generated by a current distribution $-i\omega\Delta\epsilon(\mathbf{r},\omega)\mathbf{E}_b(\mathbf{r})$, which depends on the incident field and background material.

By substituting $\epsilon(\mathbf{r},\omega)$ in Eq. (D.6) with the identical $\Delta\epsilon(\mathbf{r},\omega) + \epsilon_b(\mathbf{r},\omega)$, we arrive

at

$$\nabla \times \mathbf{H}_s = -i\omega\epsilon_b(\mathbf{r},\omega)\mathbf{E}_s - i\omega\Delta\epsilon(\mathbf{r},\omega)\mathbf{E}(\mathbf{r}), \tag{D.7}$$

which is mathematically identical, but carries a slightly different physical meaning. What we have is the scattering object represented as a current distribution $-i\omega\Delta\epsilon(\mathbf{r},\omega)\mathbf{E}(\mathbf{r})$, which acts as a source for the scattered fields $(\mathbf{E}_s, \mathbf{H}_s)$ propagating in the surrounding medium given by $\epsilon_b(\mathbf{r},\omega)$. Now, the source depends on the $\mathbf{E}_s$, which could pose additional difficulty when solving the equations numerically. However, if we have the field inside the object, the solution becomes simpler, as the scattered fields are to be defined in the background permittivity, which is in the overwhelming number of cases dispersionless and lossless.

References

[1] A. F. Koenderink, A. Alù, and A. Polman, "Nanophotonics: Shrinking light-based technology", Science 348, 516 LP –521 (2015) (cit. on pp. 9, 87).

[2] J. N. Joannopoulos, J. D. and Johnson, S. G. and Winn and M. R. D., Photonic Crystals: Molding the Flow of light, Second (Princeton University Press, 2008) (cit. on pp. 9, 11).

[3] E. Yablonovitch, "Inhibited Spontaneous Emission in Solid-State Physics and Electronics", Physical Review Letters 58, 2059–2062 (1987) (cit. on pp. 9, 11).

[4] S. John, "Strong localization of photons in certain disordered dielectric superlattices", Physical Review Letters 58, 2486–2489 (1987) (cit. on pp. 9, 11).

[5] D. Sievenpiper, L. Zhang, R. F. Jimenez Broas, N. G. Alexöpolous, and E. Yablonovitch, "High-impedance electromagnetic surfaces with a forbidden frequency band", IEEE Transactions on Microwave Theory and Techniques (1999) (cit. on p. 9).

[6] E Yablonovitch, T. J. Gmitter, and K. M. Leung, "Photonic band structure: The face-centered-cubic case employing nonspherical atoms", Physical Review Letters 67, 2295–2298 (1991) (cit. on p. 9).

[7] E Yablonovitch, "Photonic band-gap structures", Journal of the Optical Society of America B 10, 283–295 (1993) (cit. on pp. 9, 11).

[8] S. F. Joannopoulos J.D, Pierre R. Villeneuve, "Photonic crystals:putting a new twist on light", Nature 386, 7 (1997) (cit. on p. 9).

[9] H. Raether, "Surface plasmons on smooth surfaces", in Surface plasmons on smooth and rough surfaces and on gratings (Springer, 1988), pp. 4–39 (cit. on p. 9).

[10] T. Ebbesen, H. J. Lezec, H. F. Ghaemi, T. Thio, and P. A. Wolff, "Extraordinary optical transmission through sub-wavelength hole arrays", Nature 86, 1114–7 (1998) (cit. on p. 9).

[11] D. R. Smith, W. J. Padilla, D. C. Vier, S. C. Nemat-Nasser, and S Schultz, "Composite Medium with Simultaneously Negative Permeability and Permittivity", Physical Review Letters 84, 4184–4187 (2000) (cit. on pp. 9, 12).

[12] R. A. Shelby, D. R. Smith, and S Schultz, "Experimental Verification of a Negative Index of Refraction", Science 292, 77–79 (2001) (cit. on pp. 9, 12, 13).

[13] J. B. Pendry, "Negative Refraction Makes a Perfect Lens", Physical Review Letters 85, 3966–3969 (2000) (cit. on p. 9).

[14] M. Notomi, "Manipulating light with strongly modulated photonic crystals", Reports on Progress in Physics 73, 96501 (2010) (cit. on p. 12).

[15] E. Kuramochi, "Manipulating and trapping light with photonic crystals from fundamental studies to practical applications", J. Mater. Chem. C 4, 11032–11049 (2016) (cit. on p. 12).

[16] R. Baets, B. Demeulenaere, B. Dhoedt, and S. Goeman, Optical system with a dielectric subwavelength structure having high reflectivity and polarization selectivity, US Patent 6,191,890, 2001 (cit. on p. 12).

[17] X Letartre, J Mouette, J. L. Leclercq, P. R. Romeo, C Seassal, and P Viktorovitch, "Switching devices with spatial and spectral resolution combining photonic crystal and MOEMS structures", Journal of Lightwave Technology 21, 1691–1699 (2003) (cit. on p. 12).

[18] C. F. R. Mateus, M. C. Y. Huang, L. Chen, C. J. Chang-Hasnain, and Y Suzuki, "Broad-band mirror (1.12-1.62 μm) using a subwavelength grating", IEEE Photonics Technology Letters 16, 1676–1678 (2004) (cit. on p. 12).

[19] Y Ding and R Magnusson, "Resonant leaky-mode spectral-band engineering and device applications", Optics Express 12, 5661–5674 (2004) (cit. on p. 12).

[20] S Hernandez, O Gauthier-Lafaye, A.-L. Fehrembach, S Bonnefont, P Arguel, F Lozes-Dupuy, and A Sentenac, "High performance bi-dimensional resonant grating filter at 850nm under high oblique incidence of ˜60º", Applied Physics Letters 92, 131112 (2008) (cit. on p. 12).

[21] M. C. Y. Huang, Y Zhou, and C. J. Chang-Hasnain, "A surface-emitting laser incorporating a high-index-contrast subwavelength grating", Nature Photonics 1, 119–122 (2007) (cit. on p. 12).

[22] Y. Laaroussi, C. Chevallier, F. Genty, N. Fressengeas, L. Cerutti, T. Taliercio, O. Gauthier-Lafaye, P.-F. Calmon, B. Reig, J. Jacquet, and G. Almuneau, "Oxide confinement and high contrast grating mirrors for Mid-infrared VCSELs", Optical Materials Express 3, 1576–1585 (2013) (cit. on p. 12).

[23] C Sciancalepore, B. B. Bakir, S Menezo, X Letartre, D Bordel, and P Viktorovitch, "III-V-on-Si Photonic Crystal Vertical-Cavity Surface-Emitting Laser Arrays for Wavelength Division Multiplexing", IEEE Photonics Technology Letters 25, 1111–1113 (2013) (cit. on p. 12).

[24] Y. Park, E. Drouard, O. E. Daif, X. Letartre, P. Viktorovitch, A. Fave, A. Kaminski, M. Lemiti, and C. Seassal, "Absorption enhancement using photonic crystals for silicon thin film solar cells", Optics Express 17, 14312–14321 (2009) (cit. on p. 12).

[25] M. L. Brongersma, Y. Cui, and S. Fan, "Light management for photovoltaics using high-index nanostructures", Nature Materials 13, 451 (2014) (cit. on p. 12).

[26] T. Inoue, M. D. Zoysa, T. Asano, and S. Noda, "Realization of dynamic thermal emission control", Nature Materials 13, 928 (2014) (cit. on p. 12).

[27] Y. Shen, V. Rinnerbauer, I. Wang, V. Stelmakh, J. D. Joannopoulos, and M. Soljačić, "Structural Colors from Fano Resonances", ACS Photonics 2, 27–32 (2015) (cit. on pp. 12, 87).

[28] E Popov, L Mashev, and D Maystre, "Theoretical Study of the Anomalies of Coated Dielectric Gratings", Optica Acta: International Journal of Optics 33, 607–619 (1986) (cit. on pp. 12, 30).

[29] J. M. Pottage, E Silvestre, and P. S. J. Russell, "Vertical-cavity surface-emitting resonances in photonic crystal films", Journal of the Optical Society of America A 18, 442–447 (2001) (cit. on pp. 12, 30).

[30] S. Fan, W. Suh, and J. D. Joannopoulos, "Temporal coupled-mode theory for the Fano resonance in optical resonators", Journal of the Optical Society of America A 20, 569–572 (2003) (cit. on pp. 12, 30).

[31] A.-L. Fehrembach, D. Maystre, and A. Sentenac, "Phenomenological theory of filtering by resonant dielectric gratings", Journal of the Optical Society of America A 19, 1136–1144 (2002) (cit. on pp. 12, 30).

[32] A.-L. Fehrembach and A. Sentenac, "Study of waveguide grating eigenmodes for unpolarized filtering applications", Journal of the Optical Society of America A 20, 481–488 (2003) (cit. on pp. 12, 30).

[33] P. Lalanne, J. P. Hugonin, and P. Chavel, "Optical properties of deep lamellar gratings: A coupled bloch-mode insight", Journal of Lightwave Technology 24, 2442–2449 (2006) (cit. on pp. 12, 30, 31, 51).

[34] S Rytov, "Electromagnetic properties of a finely stratified medium", Soviet Physics JEPT 2, 466–475 (1956) (cit. on pp. 12, 19).

[35] A. Bensoussan, J.-L. Lions, and G. Papanicolaou, Asymptotic analysis for periodic structures, Vol. 374 (American Mathematical Soc., 2011) (cit. on p. 12).

[36] L. Solymar and E. Shamonina, Waves in metamaterials (Oxford University Press, 2009) (cit. on p. 12).

[37] M. Wegener and S. Linden, "Shaping optical space with metamaterials", Phys. Today 63, 32–36 (2010) (cit. on p. 12).

[38] M. Kadic, G. W. Milton, M. van Hecke, and M. Wegener, "3D metamaterials", Nature Reviews Physics 1, 198–210 (2019) (cit. on pp. 12, 13).

[39] V. G. Veselago, "Electrodinamics of materials both permittivity and permeability being negative", Uspekhi Fizicheskikh Nauk (in Russian) 92, 517–526 (1967) (cit. on p. 12).

[40] M. a. Dupertuis, M. Proctor, and B. Acklin, "Generalization of complex Snell-Descartes and Fresnel laws", Journal of the Optical Society of America A 11, 1159 (1994) (cit. on p. 12).

[41] N Katsarakis, G Konstantinidis, A Kostopoulos, R. S. Penciu, T. F. Gundogdu, M Kafesaki, E. N. Economou, T. Koschny, and C. M. Soukoulis, "Magnetic response of split-ring resonators in the far-infrared frequency regime", Optics Letters 30, 1348–1350 (2005) (cit. on pp. 13, 16).

[42] E. Plum, V. a. Fedotov, and N. I. Zheludev, "Planar metamaterial with transmission and reflection that depend on the direction of incidence", Applied Physics Letters 94, 2007–2010 (2009) (cit. on p. 13).

[43] C. M. Soukoulis and M. Wegener, "Past achievements and future challenges in the development of three-dimensional photonic metamaterials", Nature Photonics 5, 523–530 (2011) (cit. on pp. 12, 13).

[44] Y. Xu, Y. Fu, and H. Chen, "Planar gradient metamaterials", Nature Reviews Materials 1, 16067 (2016) (cit. on p. 12).

[45] A. Poddubny, I. Iorsh, P. Belov, and Y. Kivshar, "Hyperbolic metamaterials", Nature Photonics 7, 948–957 (2013) (cit. on p. 12).

[46] E. E. Narimanov, "Photonic Hypercrystals", Physical Review X 4, 041014 (2014) (cit. on p. 12).

[47] I. Staude and J. Schilling, "Metamaterial-inspired silicon nanophotonics", Nature Photonics 11, 274–284 (2017) (cit. on p. 13).

[48] J. S. Gomez-Diaz, M. Tymchenko, and A. Alù, "Hyperbolic metasurfaces: surface plasmons, light-matter interactions, and physical implementation using graphene strips", Optical Materials Express 5, 2313 (2015) (cit. on p. 13).

[49] O. Y. Yermakov, A. I. Ovcharenko, M Song, A. A. Bogdanov, I. V. Iorsh, and Y. S. Kivshar, "Hybrid waves localized at hyperbolic metasurfaces", Physical Review B 91, 235423 (2015) (cit. on p. 13).

[50] A. Nemilentsau, T. Low, and G. Hanson, "Anisotropic 2D materials for tunable hyperbolic plasmonics", Physical Review Letters 116, 066804 (2015) (cit. on p. 13).

[51] J. Gomis-Bresco, D. Artigas, and L. Torner, "Anisotropy-induced photonic bound states in the continuum", Nature Photonics 11, 232–236 (2017) (cit. on p. 13).

[52] T. Koschny, P Markoš, E. N. Economou, D. R. Smith, D. C. Vier, and C. M. Soukoulis, "Impact of inherent periodic structure on effective medium description of left-handed and related metamaterials", Physical Review B 71, 245105 (2005) (cit. on p. 13).

[53] D. Seetharamdoo, R. Sauleau, K. Mahdjoubi, and A.-C. Tarot, "Effective parameters of resonant negative refractive index metamaterials: Interpretation and validity", Journal of Applied Physics 98, 63505 (2005) (cit. on p. 13).

[54] C. Menzel, T. Paul, C. Rockstuhl, T. Pertsch, S. Tretyakov, and F. Lederer, "Validity of effective material parameters for optical fishnet metamaterials", Physical Review B 81, 35320 (2010) (cit. on p. 13).

[55] N. Yu and F. Capasso, "Flat optics with designer metasurfaces", Nat Mater 13, 139–150 (2014) (cit. on p. 14).

[56] A. V. Kildishev, A. Boltasseva, and V. M. Shalaev, "Planar Photonics with Metasurfaces", Science 339 (2013) (cit. on p. 14).

[57] S. Tretyakov, Analytical modeling in applied electromagnetics (Artech House, 2003) (cit. on p. 14).

[58] E. F. Kuester, M. A. Mohamed, M Piket-May, and C. L. Holloway, "Averaged transition conditions for electromagnetic fields at a metafilm", IEEE Transactions on Antennas and Propagation 51, 2641–2651 (2003) (cit. on p. 14).

[59] C. L. Holloway, A. Dienstfrey, E. F. Kuester, J. F. O'Hara, A. K. Azad, and A. J. Taylor, "A discussion on the interpretation and characterization of metafilms/metasurfaces: The two-dimensional equivalent of metamaterials", Metamaterials 3, 100–112 (2009) (cit. on p. 14).

[60] C. L. Holloway, E. F. Kuester, and D Novotny, "Waveguides Composed of Metafilms/Metasurfaces: The Two-Dimensional Equivalent of Metamaterials", IEEE Antennas and Wireless Propagation Letters 8, 525–529 (2009) (cit. on p. 14).

[61] C. L. Holloway, M. A. Mohamed, E. F. Kuester, and A Dienstfrey, "Reflection and transmission properties of a metafilm: with an application to a controllable surface composed of resonant particles", IEEE Transactions on Electromagnetic Compatibility 47, 853–865 (2005) (cit. on p. 14).

[62] C. L. Holloway, E. F. Kuester, and A Dienstfrey, "Characterizing Metasurfaces/Metafilms: The Connection Between Surface Susceptibilities and Effective Material Properties", IEEE Antennas and Wireless Propagation Letters 10, 1507–1511 (2011) (cit. on p. 14).

[63] X. Ni, S. Ishii, A. V. Kildishev, and V. M. Shalaev, "Ultra-thin, planar, Babinet-inverted plasmonic metalenses", Light: Science & Applications 2, e72 (2013) (cit. on p. 14).

[64] M. Khorasaninejad, W. T. Chen, R. C. Devlin, J. Oh, A. Y. Zhu, and F. Capasso, "Metalenses at visible wavelengths: Diffraction-limited focusing and subwavelength resolution imaging", Science 352, 1190–1194 (2016) (cit. on p. 14).

[65] H. Zuo, D.-Y. Choi, X. Gai, P. Ma, L. Xu, D. N. Neshev, B. Zhang, and B. Luther-Davies, "High-Efficiency All-Dielectric Metalenses for Mid-Infrared Imaging", Advanced Optical Materials 5, 1700585 (2017) (cit. on p. 14).

[66] M. Khorasaninejad, Z. Shi, A. Y. Zhu, W. T. Chen, V. Sanjeev, A. Zaidi, and F. Capasso, "Achromatic Metalens over 60 nm Bandwidth in the Visible and Metalens with Reverse Chromatic Dispersion", Nano Letters 17, 1819–1824 (2017) (cit. on p. 14).

[67] W. T. Chen, A. Y. Zhu, V. Sanjeev, M. Khorasaninejad, Z. Shi, E. Lee, and F. Capasso, "A broadband achromatic metalens for focusing and imaging in the visible", Nature nanotechnology 13, 220–226 (2018) (cit. on p. 14).

[68] A. She, S. Zhang, S. Shian, D. R. Clarke, and F. Capasso, "Adaptive metalenses with simultaneous electrical control of focal length, astigmatism, and shift", Science Advances 4, eaap9957 (2018) (cit. on p. 14).

[69] N. Yu, P. Genevet, M. A. Kats, F. Aieta, J. P. Tetienne, F. Capasso, and Z. Gaburro, "Light propagation with phase discontinuities: Generalized laws of reflection and refraction", Science 334, 333–337 (2011) (cit. on pp. 14, 15).

[70] D. Lin, P. Fan, E. Hasman, and M. L. Brongersma, "Dielectric gradient metasurface optical elements", Science 345, 298–302 (2014) (cit. on p. 14).

[71] M. Chen, M. Kim, A. M. Wong, and G. V. Eleftheriades, "Huygens' metasurfaces from microwaves to optics: a review", Nanophotonics 7, 1207–1231 (2018) (cit. on p. 14).

[72] A. Arbabi and A. Faraon, "Fundamental limits of ultrathin metasurfaces", Scientific Reports 7, 43722 (2017) (cit. on p. 14).

[73] A. I. Kuznetsov, A. E. Miroshnichenko, M. L. Brongersma, Y. S. Kivshar, and B. Luk'yanchuk, "Optically resonant dielectric nanostructures", Science 354 (2016) (cit. on pp. 14, 87).

[74] S. B. Glybovski, S. A. Tretyakov, P. A. Belov, Y. S. Kivshar, and C. R. Simovski, "Metasurfaces: From microwaves to visible", Physics Reports 634, 1–72 (2016) (cit. on p. 14).

[75] P. Lalanne and P. Chavel, "Metalenses at visible wavelengths: past, present, perspectives", Laser & Photonics Reviews 11, 1600295 (2017) (cit. on p. 14).

[76] A. Alù and N. Engheta, "Enabling a new degree of wave control with metamaterials: a personal perspective", Journal of Optics 19, 84008 (2017) (cit. on p. 14).

[77] F. Capasso, The future and promise of flat optics: a personal perspective, 2018 (cit. on p. 14).

[78] N. Meinzer, W. L. Barnes, and I. R. Hooper, "Plasmonic meta-atoms and metasurfaces", Nat Photon 8, 889–898 (2014) (cit. on p. 14).

[79] S. Jahani and Z. Jacob, "All-dielectric metamaterials", Nature Nanotechnology 11, 23–36 (2016) (cit. on p. 14).

[80] W. Liu and A. E. Miroshnichenko, "Beam Steering with Dielectric Metalattices", ACS Photonics 5, 1733–1741 (2018) (cit. on p. 14).

[81] D. Sell, J. Yang, E. W. Wang, T. Phan, S. Doshay, and J. A. Fan, "Ultra-High-Efficiency Anomalous Refraction with Dielectric Metasurfaces", ACS Photonics 5, 2402–2407 (2018) (cit. on p. 14).

[82] S. M. Kamali, E. Arbabi, A. Arbabi, Y. Horie, and A. Faraon, "Highly tunable elastic dielectric metasurface lenses", Laser & Photonics Reviews 10, 1002–1008 (2016) (cit. on p. 14).

[83] F. Yesilkoy, E. R. Arvelo, Y. Jahani, M. Liu, A. Tittl, V. Cevher, Y. Kivshar, and H. Altug, "Ultrasensitive hyperspectral imaging and biodetection enabled by dielectric metasurfaces", Nature Photonics 13 (2019) (cit. on pp. 14, 24).

[84] A. Krasnok, M. Caldarola, N. Bonod, and A. Alú, "Spectroscopy and Biosensing with Optically Resonant Dielectric Nanostructures", Advanced Optical Materials 6, 1701094 (2018) (cit. on pp. 14–16).

[85] B. Wang, F. Dong, Q.-T. Li, D. Yang, C. Sun, J. Chen, Z. Song, L. Xu, W. Chu, Y.-F. Xiao, Q. Gong, and Y. Li, "Visible-Frequency Dielectric Metasurfaces for Multiwavelength Achromatic and Highly Dispersive Holograms", Nano Letters 16, 5235–5240 (2016) (cit. on p. 14).

[86] Y. F. Yu, A. Y. Zhu, R. Paniagua-Domínguez, Y. H. Fu, B. Luk'yanchuk, and A. I. Kuznetsov, "High-transmission dielectric metasurface with 2π phase control at visible wavelengths", Laser & Photonics Reviews 9, 412–418 (2015) (cit. on pp. 15, 16, 87).

[87] L. C. Kennedy, L. R. Bickford, N. A. Lewinski, A. J. Coughlin, Y. Hu, E. S. Day, J. L. West, and R. A. Drezek, "A New Era for Cancer Treatment: Gold-Nanoparticle-Mediated Thermal Therapies", Small 7, 169–183 (2011) (cit. on p. 15).

[88] W. Li and J. G. Valentine, "Harvesting the loss: surface plasmon-based hot electron photodetection", Nanophotonics 6, 177 (2017) (cit. on p. 15).

[89] S. V. Boriskina, T. A. Cooper, L. Zeng, G. Ni, J. K. Tong, Y. Tsurimaki, Y. Huang, L. Meroueh, G. Mahan, and G. Chen, "Losses in plasmonics: from mitigating energy dissipation to embracing loss-enabled functionalities", Advances in Optics and Photonics 9, 775–827 (2017) (cit. on p. 15).

[90] Q. Zhao, J. Zhou, F. Zhang, and D. Lippens, "Mie resonance-based dielectric metamaterials", Materials Today 12, 60–69 (2009) (cit. on p. 16).

[91] A. I. Kuznetsov, A. E. Miroshnichenko, Y. H. Fu, J. Zhang, and B. Luk'yanchuk, "Magnetic light", Scientific reports 2, 492 (2012) (cit. on p. 16).

[92] W. T. Chen, C. J. Chen, P. C. Wu, S. Sun, L. Zhou, G.-Y. Guo, C. T. Hsiao, K.-Y. Yang, N. I. Zheludev, and D. P. Tsai, "Optical magnetic response in three-dimensional metamaterial of upright plasmonic meta-molecules", Optics Express 19, 12837–12842 (2011) (cit. on p. 16).

[93] G Dolling, C Enkrich, M Wegener, J. F. Zhou, C. M. Soukoulis, and S Linden, "Cut-wire pairs and plate pairs as magnetic atoms for optical metamaterials", Optics Letters 30, 3198–3200 (2005) (cit. on p. 16).

[94] V. M. Shalaev, W. Cai, U. K. Chettiar, H.-K. Yuan, A. K. Sarychev, V. P. Drachev, and A. V. Kildishev, "Negative index of refraction in optical metamaterials", Optics Letters 30, 3356–3358 (2005) (cit. on p. 16).

[95] A. Moreau, C. Ciracì, J. J. Mock, R. T. Hill, Q. Wang, B. J. Wiley, A. Chilkoti, and D. R. Smith, "Controlled-reflectance surfaces with film-coupled colloidal nanoantennas", Nature 492, 86 (2012) (cit. on p. 16).

[96] A. Devilez, X. Zambrana-Puyalto, B. Stout, and N. Bonod, "Mimicking localized surface plasmons with dielectric particles", Physical Review B - Condensed Matter and Materials Physics 92, 24–28 (2015) (cit. on p. 16).

[97] S. D. Isro, A. A. Iskandar, Y. S. Kivshar, and I. V. Shadrivov, "Engineering scattering patterns with asymmetric dielectric nanorods", Optics Express 26, 32624–32630 (2018) (cit. on p. 16).

[98] D. Vercruysse, Y. Sonnefraud, N. Verellen, F. B. Fuchs, G. Di Martino, L. Lagae, V. V. Moshchalkov, S. A. Maier, and P. Van Dorpe, "Unidirectional Side Scattering of Light by a Single-Element Nanoantenna", Nano Letters 13, 3843–3849 (2013) (cit. on p. 16).

[99] W. Liu, A. E. Miroshnichenko, D. N. Neshev, and Y. S. Kivshar, "Broadband Unidirectional Scattering by Magneto-Electric Core–Shell Nanoparticles", ACS Nano 6, 5489–5497 (2012) (cit. on p. 16).

[100] R. Paniagua-Dominguez, Y. F. Yu, A. E. Miroshnichenko, L. A. Krivitsky, Y. H. Fu, V. Valuckas, L. Gonzaga, Y. T. Toh, A. Y. S. Kay, B. Luk/'yanchuk, and A. I. Kuznetsov, "Generalized Brewster effect in dielectric metasurfaces", Nat Commun 7 (2016) (cit. on p. 16).

[101] Y. H. Fu, A. I. Kuznetsov, A. E. Miroshnichenko, Y. F. Yu, and B. Luk'yanchuk, "Directional visible light scattering by silicon nanoparticles", Nature Communications 4, 1527 (2013) (cit. on p. 16).

[102] A. E. Miroshnichenko, B. Luk'yanchuk, S. A. Maier, and Y. S. Kivshar, "Optically Induced Interaction of Magnetic Moments in Hybrid Metamaterials", ACS Nano 6, 837–842 (2012) (cit. on p. 16).

[103] K. Koshelev, G. Favraud, A. Bogdanov, Y. Kivshar, and A. Fratalocchi, Nonradiating photonics with resonant dielectric nanostructures, 2019 (cit. on pp. 16, 24).

[104] C. W. Hsu, B. Zhen, J. Lee, S.-L. Chua, S. G. Johnson, J. D. Joannopoulos, and M. Soljacic, "Observation of trapped light within the radiation continuum", Nature 499, 188–191 (2013) (cit. on pp. 16, 24, 25, 28).

[105] K. V. Baryshnikova, D. A. Smirnova, B. S. Luk'yanchuk, and Y. S. Kivshar, "Optical Anapoles: Concepts and Applications", Advanced Optical Materials, 1801350 (2019) (cit. on p. 16).

[106] F. Monticone, D. Sounas, A. Krasnok, and A. Alù, "Can a nonradiating mode be externally excited? Nonscattering states vs. embedded eigenstates", arXiv preprint arXiv:1908.00956 (2019) (cit. on p. 16).

[107] G. Mie, "Beiträge zur Optik trüber Medien, speziell kolloidaler Metallösungen", Annalen der Physik 330, 377–445 (1908) (cit. on pp. 17, 55).

[108] G. Gouesbet, "Generalized lorenz-mie theory and applications", Particle & Particle Systems Characterization 11, 22–34 (1994) (cit. on p. 17).

[109] G Gouesbet and L Mees, "Generalized Lorenz–Mie theory for infinitely long elliptical cylinders", JOSA A 16, 1333–1341 (1999) (cit. on p. 17).

[110] K. F. Ren, G Gréhan, and G Gouesbet, "Scattering of a Gaussian beam by an infinite cylinder in the framework of generalized Lorenz–Mie theory: formulation and numerical results", Journal of the Optical Society of America A 14, 3014–3025 (1997) (cit. on p. 17).

[111] F. Xu, K. Ren, G. Gouesbet, G. Gréhan, and X. Cai, "Generalized Lorenz-Mie theory for an arbitrarily oriented, located, and shaped beam scattered by a homogeneous spheroid", Journal of the Optical Society of America A 24, 119–131 (2007) (cit. on p. 17).

[112] J.-C. Auger and B. Stout, "A recursive centered T-matrix algorithm to solve the multiple scattering equation: numerical validation", Journal of Quantitative Spectroscopy and Radiative Transfer 79-80, 533–547 (2003) (cit. on pp. 18, 55, 93).

[113] B. Stout, A. Devilez, B. Rolly, and N. Bonod, "Multipole methods for nanoantennas design: applications to Yagi-Uda configurations", Journal of the Optical Society of America B 28, 1213 (2011) (cit. on pp. 18, 55, 93, 96).

[114] B. Stout, J.-C. Auger, and J. Lafait, "A transfer matrix approach to local field calculations in multiple-scattering problems", Journal of Modern Optics 49, 2129–2152 (2002) (cit. on pp. 18, 55, 93).

[115] A. Egel and U. Lemmer, "Dipole emission in stratified media with multiple spherical scatterers: Enhanced outcoupling from OLEDs", Journal of Quantitative Spectroscopy and Radiative Transfer 148, 165–176 (2014) (cit. on pp. 18, 55, 61, 93).

[116] J. Zhao, A. O. Pinchuk, J. M. McMahon, S. Li, L. K. Ausman, A. L. Atkinson, and G. C. Schatz, "Methods for describing the electromagnetic properties of silver and gold nanoparticles", Accounts of Chemical Research 41, 1710–1720 (2008) (cit. on pp. 18, 19).

[117] A. Taflove and S. C. Hagness, Computational electrodynamics: the finite-difference time-domain method (Artech house, 2005) (cit. on p. 18).

[118] K. Yee, "Numerical solution of initial boundary value problems involving maxwell's equations in isotropic media", IEEE Transactions on Antennas and Propagation 14, 302–307 (1966) (cit. on p. 18).

[119] J.-M. Jin, The finite element method in electromagnetics (John Wiley & Sons, 2015) (cit. on p. 18).

[120] M. Yurkin and A. Hoekstra, "The discrete dipole approximation: An overview and recent developments", Journal of Quantitative Spectroscopy and Radiative Transfer 106, 558–589 (2007) (cit. on p. 18).

[121] A. B. Evlyukhin, C. Reinhardt, and B. N. Chichkov, "Multipole light scattering by nonspherical nanoparticles in the discrete dipole approximation", Physical Review B 84, 235429 (2011) (cit. on p. 18).

[122] M. G. Moharam, D. A. Pommet, E. B. Grann, and T. K. Gaylord, "Stable implementation of the rigorous coupled-wave analysis for surface-relief gratings: enhanced transmittance matrix approach", Journal of the Optical Society of America A 12, 1077–1086 (1995) (cit. on p. 19).

[123] M. G. Moharam, E. B. Grann, D. a. Pommet, and T. K. Gaylord, "Formulation for stable and efficient implementation of the rigorous coupled-wave analysis of binary gratings", Journal of the Optical Society of America A 12, 1068 (1995) (cit. on pp. 19, 27, 31, 33, 113).

[124] P. Lalanne and G. M. Morris, "Highly improved convergence of the coupled-wave method for TM polarization", Journal of the Optical Society of America A 13, 779–784 (1996) (cit. on p. 19).

[125] S. Peng and G. M. Morris, "Efficient implementation of rigorous coupled-wave analysis for surface-relief gratings", Journal of the Optical Society of America A 12, 1087–1096 (1995) (cit. on p. 19).

[126] L. Li, "Formulation and comparison of two recursive matrix algorithms for modeling layered diffraction gratings", Journal of the Optical Society of America A 13, 1024 (1996) (cit. on p. 19).

[127] G Granet and B Guizal, "Efficient implementation of the coupled-wave method for metallic lamellar gratings in TM polarization", Journal of the Optical Society of America A 13, 1019–1023 (1996) (cit. on p. 19).

[128] E. Silberstein, P. Lalanne, J. P. Hugonin, and Q. Cao, "Use of grating theories in integrated optics", Journal of the Optical Society of America. A, Optics, image science, and vision 18, 2865–2875 (2001) (cit. on p. 19).

[129] J. P. Hugonin and P. Lalanne, "Perfectly matched layers as nonlinear coordinate transforms: a generalized formalization", Journal of the Optical Society of America A 22, 1844–1849 (2005) (cit. on p. 19).

[130] L. Novotny and B. Hecht, Principles of Nano-Optics (Cambridge University Press, Cambridge, 2012) (cit. on p. 19).

[131] R. Liu, T. J. Cui, D. Huang, B. Zhao, and D. R. Smith, "Description and explanation of electromagnetic behaviors in artificial metamaterials based on effective medium theory", Physical Review E 76, 1–8 (2007) (cit. on p. 19).

[132] C. Blanchard, P. Viktorovitch, and X. Letartre, "Perturbation approach for the control of the quality factor in photonic crystal membranes: Application to selective absorbers", Physical Review A 90, 33824 (2014) (cit. on pp. 24, 25).

[133] C. W. Hsu, B. Zhen, A. D. Stone, J. D. Joannopoulos, and M. Soljačić, "Bound states in the continuum", Nature Reviews Materials 1, 16048 (2016) (cit. on pp. 24, 28).

[134] F. Monticone and A. Alù, "Embedded Photonic Eigenvalues in 3D Nanostructures", Physical Review Letters 112, 213903 (2014) (cit. on p. 24).

[135] J Von Neuman and E. Wigner, "Uber merkwürdige diskrete Eigenwerte. Uber das Verhalten von Eigenwerten bei adiabatischen Prozessen", Physikalische Zeitschrift 30, 467–470 (1929) (cit. on p. 24).

[136] H. Friedrich and D. Wintgen, "Interfering resonances and bound states in the continuum", Physical Review A 32, 3231–3242 (1985) (cit. on pp. 24, 28).

[137] J. W. Yoon, S. H. Song, and R. Magnusson, "Critical field enhancement of asymptotic optical bound states in the continuum", Scientific Reports 5, 18301 (2015) (cit. on p. 24).

[138] C. Blanchard, J.-P. Hugonin, and C. Sauvan, "Fano resonances in photonic crystal slabs near optical bound states in the continuum", Physical Review B 94, 155303 (2016) (cit. on pp. 24, 26).

[139] Z. F. Sadrieva, I. S. Sinev, K. L. Koshelev, A. Samusev, I. V. Iorsh, O. Takayama, R. Malureanu, A. A. Bogdanov, and A. V. Lavrinenko, "Transition from Optical Bound States in the Continuum to Leaky Resonances: Role of Substrate and Roughness", ACS Photonics 4, 723–727 (2017) (cit. on pp. 24, 51).

[140] A. Kodigala, T. Lepetit, Q. Gu, B. Bahari, Y. Fainman, and B. Kanté, "Lasing action from photonic bound states in continuum", Nature 541, 196–199 (2017) (cit. on pp. 24, 25, 28).

[141] S. T. Ha, Y. H. Fu, N. K. Emani, Z. Pan, R. M. Bakker, R. Paniagua-Domínguez, and A. I. Kuznetsov, "Directional lasing in resonant semiconductor nanoantenna arrays", Nature Nanotechnology 13, 1042–1047 (2018) (cit. on p. 24).

[142] Y. Liu, W. Zhou, and Y. Sun, "Optical Refractive Index Sensing Based on High-Q Bound States in the Continuum in Free-Space Coupled Photonic Crystal Slabs", Sensors 17, 1861 (2017) (cit. on p. 24).

[143] S. Romano, G. Zito, S. Torino, G. Calafiore, E. Penzo, G. Coppola, S. Cabrini, I. Rendina, and V. Mocella, "Label-free sensing of ultralow-weight molecules with all-dielectric metasurfaces supporting bound states in the continuum", Photonics Research 6, 726–733 (2018) (cit. on p. 24).

[144] L. Li and H. Yin, "Bound States in the Continuum in double layer structures", Scientific Reports 6, 26988 (2016) (cit. on p. 25).

[145] Y. Wang, J. Song, L. Dong, and M. Lu, "Optical bound states in slotted high-contrast gratings", Journal of the Optical Society of America B 33, 2472–2479 (2016) (cit. on pp. 25, 49).

[146] X. Gao, C. W. Hsu, B. Zhen, X. Lin, J. D. Joannopoulos, M. Soljačić, and H. Chen, "Formation mechanism of guided resonances and bound states in the continuum in photonic crystal slabs", Scientific Reports 6, 31908 (2016) (cit. on pp. 25, 34, 48).

[147] S. I. Azzam, V. M. Shalaev, A. Boltasseva, and A. V. Kildishev, "Formation of Bound States in the Continuum in Hybrid Plasmonic-Photonic Systems", Physical Review Letters 121, 253901 (2018) (cit. on p. 25).

[148] E. N. Bulgakov, D. N. Maksimov, P. N. Semina, and S. A. Skorobogatov, "Propagating bound states in the continuum in dielectric gratings", Journal of the Optical Society of America B 35, 1218–1222 (2018) (cit. on pp. 25, 52, 53).

[149] Y. Yang, C. Peng, Y. Liang, Z. Li, and S. Noda, "Analytical Perspective for Bound States in the Continuum in Photonic Crystal Slabs", Physical Review Letters 113, 37401 (2014) (cit. on p. 25).

[150] Z. Wang, H. Zhang, L. Ni, W. Hu, and C. Peng, "Analytical Perspective of Interfering Resonances in High-Index-Contrast Periodic Photonic Structures", IEEE Journal of Quantum Electronics 52, 1–9 (2016) (cit. on p. 25).

[151] L. Ni, Z. Wang, C. Peng, and Z. Li, "Tunable optical bound states in the continuum beyond in-plane symmetry protection", Physical Review B 94, 245148 (2016) (cit. on p. 25).

[152] E. N. Bulgakov and D. N. Maksimov, "Avoided crossings and bound states in the continuum in low-contrast dielectric gratings", Physical Review A 98, 053840 (2018) (cit. on p. 25).

[153] V. Karagodsky, F. G. Sedgwick, and C. J. Chang-Hasnain, "Theoretical analysis of subwavelength high contrast grating reflectors", Optics Express 18, 16973–16988 (2010) (cit. on pp. 25, 31).

[154] V. Karagodsky, C. Chase, and C. J. Chang-Hasnain, "Matrix Fabry–Perot resonance mechanism in high-contrast gratings", Optics Letters 36, 1704–1706 (2011) (cit. on pp. 25, 31).

[155] V. Karagodsky and C. J. Chang-Hasnain, "Physics of near-wavelength high contrast gratings", Optics Express 20, 10888–10895 (2012) (cit. on pp. 25, 26, 31).

[156] Q. Bai, M. Perrin, C. Sauvan, J.-P. Hugonin, and P. Lalanne, "Efficient and intuitive method for the analysis of light scattering by a resonant nanostructure", Optics Express 21, 27371 (2013) (cit. on pp. 27, 34, 56, 66, 68, 70, 88, 89, 91).

[157] P Lalanne, W Yan, A Gras, C Sauvan, J.-P. Hugonin, M Besbes, G Demésy, M. D. Truong, B Gralak, F Zolla, A Nicolet, F Binkowski, L Zschiedrich, S Burger, J Zimmerling, R Remis, P Urbach, H. T. Liu, and T Weiss, "Quasinormal mode solvers for resonators with dispersive materials", Journal of the Optical Society of America A 36, 686–704 (2019) (cit. on pp. 27, 66, 68, 69, 75, 89, 107).

[158] P. Lalanne, S. Astilean, P. Chavel, E. Cambril, and H. Launois, "Design and fabrication of blazed binary diffractive elements with sampling periods smaller than the structural cutoff", Journal of the Optical Society of America A 16, 1143–1156 (1999) (cit. on p. 31).

[159] G. Lecamp, P. Lalanne, J. P. Hugonin, and J. M. Gérard, "Energy transfer through laterally confined Bragg mirrors and its impact on pillar microcavities", IEEE Journal of Quantum Electronics 41, 1323–1329 (2005) (cit. on pp. 34, 37, 113).

[160] H. A. Haus, Waves and fields in optoelectronics (Prentice-Hall International, London, 1984) (cit. on p. 35).

[161] P Lalanne, C Sauvan, and J. P. Hugonin, "Photon confinement in photonic crystal nanocavities", Laser & Photonics Reviews 2, 514–526 (2008) (cit. on p. 35).

[162] C Sauvan, P Lalanne, and J. P. Hugonin, "Slow-wave effect and mode-profile matching in photonic crystal microcavities", Physical Review B 71, 165118 (2005) (cit. on p. 35).

[163] A. Taghizadeh, J. Mørk, and I.-S. Chung, "Ultracompact resonator with high quality-factor based on a hybrid grating structure", Optics Express 23, 14913–14921 (2015) (cit. on p. 51).

[164] F. Dubois, "Etude des propriétés spectro-spatiales des cristaux photoniques membranaires à symétrie brisée", PhD thesis (Université de Lyon, 2018) (cit. on p. 52).

[165] P. C. Waterman, "Matrix formulation of electromagnetic scattering", Proceedings of the IEEE 53, 805–812 (1965) (cit. on pp. 55, 57, 61).

[166] L. Tsang, J. A. Kong, and K.-H. Ding, Scattering of Electromagnetic Waves: Theories and Applications (John Wiley and Sons, New Yprk, 2000) (cit. on pp. 55, 58, 59).

[167] B. Peterson and S. Ström, "T Matrix for Electromagnetic Scattering from an Arbitrary Number of Scatterers and Representations of E(3)", Physical Review D 8, 3661–3678 (1973) (cit. on pp. 55, 57).

[168] A. Doicu, T. Wriedt, and Y. A. Eremin, Light scattering by systems of particles: null-field method with discrete sources: theory and programs (Springer, Berlin, 2006) (cit. on pp. 55, 56, 61).

[169] M. I. Mishchenko, G. Videen, V. A. Babenko, N. G. Khlebtsov, and T. Wriedt, "T-matrix theory of electromagnetic scattering by particles and its applications: A comprehensive reference database", Journal of Quantitative Spectroscopy and Radiative Transfer (2004) (cit. on pp. 55, 57, 87, 93).

[170] A. Doicu and T. Wriedt, "Calculation of the T matrix in the null-field method with discrete sources", Journal of the Optical Society of America A 16, 2539–2544 (1999) (cit. on pp. 56, 61).

[171] G. Demésy, J.-C. Auger, and B. Stout, "Scattering matrix of arbitrarily shaped objects: combining finite elements and vector partial waves", Journal of the Optical Society of America A 35, 1401 (2018) (cit. on pp. 56, 61).

[172] X. G. Santiago, M. Hammerschmidt, S. Burger, C. Rockstuhl, I. Fernandez-Corbaton, and L. Zschiedrich, "Decomposition of scattered electromagnetic fields into vector spherical wave functions on surfaces with general shapes", Physical Review B 99, 1–7 (2019) (cit. on pp. 56, 61).

[173] P. Lalanne, W. Yan, K. Vynck, C. Sauvan, and J.-P. Hugonin, "Light Interaction with Photonic and Plasmonic Resonances", Laser & Photonics Reviews 12, 1700113 (2018) (cit. on pp. 56, 64, 66, 68, 70, 71).

[174] F. Alpeggiani, N. Parappurath, E. Verhagen, and L Kuipers, "Quasinormal-Mode Expansion of the Scattering Matrix", Physical Review X 7, 21035 (2017) (cit. on p. 56).

[175] W. Yan, R. Faggiani, and P. Lalanne, "Rigorous modal analysis of plasmonic nanoresonators", Physical Review B 97, 1–10 (2018) (cit. on pp. 56, 66, 68, 69, 71, 72, 74–76).

[176] T Weiss and E. A. Muljarov, "How to calculate the pole expansion of the optical scattering matrix from the resonant states", Physical Review B 98, 85433 (2018) (cit. on pp. 56, 76).

[177] R. Colom, R. McPhedran, B. Stout, and N. Bonod, "Modal expansion of the scattered field: Causality, nondivergence, and nonresonant contribution", Physical Review B 98, 85418 (2018) (cit. on pp. 56, 66, 76).

[178] P. C. Waterman, "Symmetry, Unitarity, and Geometry in Electromagnetic Scattering", Physical Review D 3, 825–839 (1971) (cit. on p. 57).

[179] P Barber and C Yeh, "Scattering of electromagnetic waves by arbitrarily shaped dielectric bodies", Applied Optics 14, 2864–2872 (1975) (cit. on pp. 57, 61).

[180] M. I. Mishchenko, "Light scattering by randomly oriented axially symmetric particles", Journal of the Optical Society of America A 8, 871–882 (1991) (cit. on pp. 57, 60).

[181] M. I. Mishchenko, L. D. Travis, and D. W. Mackowski, "T-matrix method and its applications to electromagnetic scattering by particles: A current perspective", Journal of Quantitative Spectroscopy and Radiative Transfer 111, 1700–1703 (2010) (cit. on p. 57).

[182] M. I. Mishchenko, L. D. Travis, and A. a. Lacis, Scattering, Absorption, and Emission of Light by Small Particles (Cambridge University Press, 2002) (cit. on pp. 58, 61).

[183] P. Grahn, A. Shevchenko, and M. Kaivola, "Electromagnetic multipole theory for optical nanomaterials", New Journal of Physics 14, 093033 (2012) (cit. on p. 63).

[184] R. Alaee, C. Rockstuhl, and I. Fernandez-Corbaton, "An electromagnetic multipole expansion beyond the long-wavelength approximation", Optics Communications 407, 17–21 (2018) (cit. on p. 63).

[185] P. T. Kristensen and S. Hughes, "Modes and Mode Volumes of Leaky Optical Cavities and Plasmonic Nanoresonators", ACS Photonics 1, 2–10 (2014) (cit. on p. 66).

[186] P. T. Leung, S. Y. Liu, and K Young, "Completeness and orthogonality of quasinormal modes in leaky optical cavities", Physical Review A 49, 3057–3067 (1994) (cit. on pp. 66, 70).

[187] R. K. Chang and A. J. Campillo, Optical processes in microcavities, Vol. 3 (World scientific, 1996) (cit. on p. 66).

[188] A. W. Snyder and J. D. Love, "Optical Waveguide Theory Chapman and Hall", New York (1983) (cit. on p. 66).

[189] R. M. More, "Theory of Decaying States", Physical Review A 4, 1782–1790 (1971) (cit. on p. 66).

[190] C. Sauvan, J. P. Hugonin, I. S. Maksymov, and P. Lalanne, "Theory of the spontaneous optical emission of nanosize photonic and plasmon resonators", Physical Review Letters 110, 1–5 (2013) (cit. on pp. 66, 70, 72, 77, 88, 92, 98).

[191] J. Zimmerling, L. Wei, P. Urbach, and R. Remis, "Efficient computation of the spontaneous decay rate of arbitrarily shaped 3D nanosized resonators: a Krylov model-order reduction approach", Applied Physics A 122, 158 (2016) (cit. on pp. 66, 68, 69).

[192] L. Zschiedrich, F. Binkowski, N. Nikolay, O. Benson, G. Kewes, and S. Burger, "Riesz-projection-based theory of light-matter interaction in dispersive nanoresonators", Physical Review A 98, 43806 (2018) (cit. on p. 66).

[193] F. Zolla, A. Nicolet, and G. Demésy, "Photonics in highly dispersive media: the exact modal expansion", Optics Letters 43, 5813–5816 (2018) (cit. on p. 66).

[194] S. Franke, S. Hughes, M. K. Dezfouli, P. T. Kristensen, K. Busch, A. Knorr, and M. Richter, "Quantization of Quasinormal Modes for Open Cavities and Plasmonic Cavity Quantum Electrodynamics", Physical Review Letters 122, 213901 (2019) (cit. on p. 66).

[195] M Garcia-Vergara, G Demésy, and F Zolla, "Extracting an accurate model for permittivity from experimental data: hunting complex poles from the real line", Optics Letters 42, 1145–1148 (2017) (cit. on p. 67).

[196] A. Raman and S. Fan, "Photonic band structure of dispersive metamaterials formulated as a Hermitian eigenvalue problem", Physical Review Letters 104, 87401 (2010) (cit. on pp. 68, 69).

[197] Y. Brûlé, B. Gralak, and G. Demésy, "Calculation and analysis of the complex band structure of dispersive and dissipative two-dimensional photonic crystals", Journal of the Optical Society of America B 33, 691–702 (2016) (cit. on p. 69).

[198] M. B. Doost, W. Langbein, and E. A. Muljarov, "Resonant-state expansion applied to three-dimensional open optical systems", Physical Review A 90, 1–14 (2014) (cit. on p. 70).

[199] C. Sauvan, J.-P. Hugonin, and P. Lalanne, "Photonic and plasmonic nanoresonators: a modal approach", in Active photonic materials vii, Vol. 9546, August 2015 (2015), p. 95461C (cit. on p. 70).

[200] B. Stout and R. McPhedran, "Egocentric physics: Just about Mie", EPL (Europhysics Letters) 119, 44002 (2017) (cit. on p. 76).

[201] C. F. Bohren and D. R. Huffman, Absorption and scattering of light by small particles (John Wiley & Sons, 2008) (cit. on pp. 78, 80).

[202] J. Bar-David, N. Mazurski, and U. Levy, "In-Situ planarization of Huygens metasurfaces by nanoscale local oxidation of silicon", ACS Photonics (2017) (cit. on p. 87).

[203] R. Verre, D. G. Baranov, B. Munkhbat, J. Cuadra, M. Käll, and T. Shegai, "Transition metal dichalcogenide nanodisks as high-index dielectric Mie nanoresonators", Nature Nanotechnology 14, 679–683 (2019) (cit. on p. 87).

[204] K. E. Chong, L. Wang, I. Staude, A. R. James, J. Dominguez, S. Liu, G. S. Subramania, M. Decker, D. N. Neshev, I. Brener, and Y. S. Kivshar, "Efficient Polarization-Insensitive Complex Wavefront Control Using Huygens' Metasurfaces Based on Dielectric Resonant Meta-atoms", ACS Photonics 3, 514–519 (2016) (cit. on p. 87).

[205] A. B. Evlyukhin, R. L. Eriksen, W. Cheng, J. Beermann, C. Reinhardt, A. Petrov, S. Prorok, M. Eich, B. N. Chichkov, and S. I. Bozhevolnyi, "Optical spectroscopy of single Si nanocylinders with magnetic and electric resonances.", Scientific Reports 4, 4126 (2014) (cit. on p. 87).

[206] V. Flauraud, M. Reyes, R. Paniagua-Domínguez, A. I. Kuznetsov, and J. Brugger, "Silicon Nanostructures for Bright Field Full Color Prints", ACS Photonics 4, 1913–1919 (2017) (cit. on p. 87).

[207] P. Moitra, B. A. Slovick, Z. Gang Yu, S. Krishnamurthy, and J. Valentine, "Experimental demonstration of a broadband all-dielectric metamaterial perfect reflector", Applied Physics Letters 104, 10–15 (2014) (cit. on p. 87).

[208] A. K. Ospanova, G. Labate, L. Matekovits, and A. A. Basharin, "Multipolar passive cloaking by nonradiating anapole excitation", Scientific Reports 8, 12514 (2018) (cit. on p. 87).

[209] H. Wang, X. Wang, C. Yan, H. Zhao, J. Zhang, C. Santschi, and O. J. F. Martin, "Full Color Generation Using Silver Tandem Nanodisks", ACS Nano 11, 4419–4427 (2017) (cit. on p. 87).

[210] I. Staude, T. Pertsch, and Y. S. Kivshar, "All-Dielectric Resonant Meta-Optics Lightens up", ACS Photonics 6, 802–814 (2019) (cit. on p. 87).

[211] S. Kruk and Y. Kivshar, "Functional Meta-Optics and Nanophotonics Govern by Mie Resonances", ACS Photonics 4, 2638–2649 (2017) (cit. on p. 87).

[212] L. Novotny and N. van Hulst, "Antennas for light", Nature Photonics 5, 83–90 (2011) (cit. on p. 87).

[213] I. S. Maksymov, I. Staude, A. E. Miroshnichenko, and Y. S. Kivshar, "Optical Yagi-Uda nanoantennas", Nanophotonics 1, 65–81 (2012) (cit. on pp. 87, 96, 97).

[214] F. Bigourdan, J.-P. Hugonin, and P. Lalanne, "Aperiodic-Fourier modal method for analysis of body-of-revolution photonic structures", Journal of the Optical Society of America A 31, 1303–1311 (2014) (cit. on pp. 91, 107, 108).

[215] J. P. Hugonin and P Lalanne, Reticolo software for grating analysis, 2005 (cit. on pp. 93, 113, 117).

[216] A. G. Curto, G. Volpe, T. H. Taminiau, M. P. Kreuzer, R. Quidant, and N. F. van Hulst, "Unidirectional Emission of a Quantum Dot Coupled to a Nanoantenna", Science 329, 930 LP –933 (2010) (cit. on p. 96).

[217] T. H. Taminiau, F. D. Stefani, and N. F. van Hulst, "Enhanced directional excitation and emission of single emitters by a nano-optical Yagi-Uda antenna", Optics Express 16, 10858–10866 (2008) (cit. on p. 96).

[218] T. Kosako, Y. Kadoya, and H. F. Hofmann, "Directional control of light by a nano-optical Yagi – Uda antenna", Nature Photonics 4, 312–315 (2010) (cit. on p. 96).

[219] J. Ho, Y. H. Fu, Z. Dong, R. Paniagua-Dominguez, E. H. H. Koay, Y. F. Yu, V. Valuckas, A. I. Kuznetsov, and J. K. W. Yang, "Highly Directive Hybrid Metal–Dielectric Yagi-Uda Nanoantennas", ACS Nano 12, 8616–8624 (2018) (cit. on p. 96).

[220] A. E. Krasnok, A. E. Miroshnichenko, P. A. Belov, and Y. S. Kivshar, "All-dielectric optical nanoantennas", Optics Express 20, 20599–20604 (2012) (cit. on p. 96).

[221] K. R. Mahmoud, M. Hussein, M. F. O. Hameed, and S. S. A. Obayya, "Super directive Yagi–Uda nanoantennas with an ellipsoid reflector for optimal radiation emission", Journal of the Optical Society of America B 34, 2041–2049 (2017) (cit. on p. 96).

[222] Y. G. Liu, W. C. H. Choy, W. E. I. Sha, and W. Cho Chew, "Unidirectional and wavelength-selective photonic sphere-array nanoantennas", Optics Letters 37, 2112–2114 (2012) (cit. on p. 96).

[223] A. E. Miroshnichenko, I. S. Maksymov, A. R. Davoyan, C. Simovski, P. Belov, and Y. S. Kivshar, "An arrayed nanoantenna for broadband light emission and detection", Physica Status Solidi RRL 5, 347–349 (2011) (cit. on p. 96).

[224] I. S. Maksymov, A. R. Davoyan, and Y. S. Kivshar, "Enhanced emission and light control with tapered plasmonic nanoantennas", Applied Physics Letters 99, 83304 (2011) (cit. on p. 96).

[225] I. S. Maksymov, A. R. Davoyan, A. E. Miroshnichenko, C. Simovski, P. Belov, and Y. S. Kivshar, "Multifrequency tapered plasmonic nanoantennas", Optics Communications 285, 821–824 (2012) (cit. on p. 96).

[226] T. Pakizeh and M. Käll, "Unidirectional Ultracompact Optical Nanoantennas", Nano Letters 9, 2343–2349 (2009) (cit. on p. 97).

[227] A. F. Koenderink, "Plasmon Nanoparticle Array Waveguides for Single Photon and Single Plasmon Sources", Nano Letters 9, 4228–4233 (2009) (cit. on p. 98).

[228] O. L. Muskens, V Giannini, J. A. Sánchez-Gil, and J Gómez Rivas, "Strong Enhancement of the Radiative Decay Rate of Emitters by Single Plasmonic Nanoantennas", Nano Letters 7, 2871–2875 (2007) (cit. on p. 98).

[229] K. B. Crozier, W Zhu, D Wang, S Lin, M. D. Best, and J. P. Camden, "Plasmonics for Surface Enhanced Raman Scattering: Nanoantennas for Single Molecules", IEEE Journal of Selected Topics in Quantum Electronics 20, 152–162 (2014) (cit. on p. 98).

[230] E. M. Purcell, "Spontaneous Emission Probabliities at Radio Frquencies", Physical Review 69, 681 (1946) (cit. on p. 98).

[231] J. Yang, J.-P. Hugonin, and P. Lalanne, "Near-to-Far Field Transformations for Radiative and Guided Waves", ACS Photonics 3, 395–402 (2016) (cit. on p. 102).

université PARIS-SACLAY
ÉCOLE DOCTORALE
Ondes et Matière (EDOM)

Titre : Modélisation de nanostructures optiques résonantes avec des méthodes semi-analytiques utilisant les modes propres de l'objet

Mots clés : Métasurfaces optiques, Nanoantennes optiques, Plaques de cristaux photoniques

Résumé : Cette thèse est consacrée au développement de modèles semi-analytiques précis pour le calcul numérique de dispositifs nanophotoniques résonants : les membranes à cristaux photoniques l'ensembles composés de plusieurs nano-antennes plasmoniques. La thèse est divisée en deux parties.

La première partie présente un modèle semi-analytique pour le calcul des modes supportés par des membranes à cristaux photoniques. Ce modèle est appliqué à l'étude des états liés dans le continuum (bound states in the continuum, ou BIC). Grâce à la semi-analyticité du modèle, nous étudions la dynamique des BICs avec l'épaisseur de la membrane pour des structures symétriques et asymétriques.

La deuxième partie est consacrée au développement d'une théorie modale originale pour modéliser la diffusion de la lumière par des structures complexes composées d'un ensemble de plusieurs nano-antennes. L'objectif est de pouvoir modéliser la diffusion de la lumière par des métasurfaces à partir de la seule connaissance des modes de leurs constituants individuels. Pour ce faire, nous combinons un formalisme modal basé sur l'utilisation des modes quasi-normaux (QNM) avec la théorie multipolaire de la diffusion multiple basée sur le calcul de la matrice de transition (matrice T) d'un diffuseur unique. L'utilisation d'une décomposition modale avec des QNMs nous permet d'une part de rendre une partie du calcul analytique et d'autre part d'apporter une meilleure compréhension physique.

Enfin, la décomposition modale de la matrice T est appliquée à des cas pratiques d'intérêt en nanophotonique. A partir de la seule connaissance de quelques modes d'un nanocylindre plasmonique unique, nous calculons analytiquement la diffusion multiple de la lumière par un dimère et par une antenne Yagi-Uda composés de ces nanocylindres.

Title : Modelling of resonant optical nanostructures with semi-analytical methods based on the object eigenmodes

Keywords : Optical Nanoantennas, Optical metasurfaces, Photonic crystal slabs

Abstract: The presented thesis is dedicated to the development of semi-analytical accurate models for the numerical calculation of resonant nanophotonic devices: photonic crystal slabs and ensembles composed of several plasmonic nanoantennas. The structure of the thesis is two-fold.

In the first part, a semi-analytical model for the calculation of the modes supported by photonic crystal slabs (their dispersion and quality factors) is presented. This model is applied to the study of bound states in the continuum (BICs). Thanks to the semi-analyticity of the model, we investigate the dynamics of BICs with the slab thickness in symmetric and asymmetric photonic crystal slab.

The second part of the thesis is dedicated to the development of an original modal theory to model light scattering by complex structures composed of a small ensemble of plasmonic nanoantennas. The objective is to be able to model light scattering by metasurfaces from the sole knowledge of the eigenmodes of their individual constituents. For that purpose, we combine a quasi-normal mode (QNM) formalism with the multipole multiple-scattering theory based on the calculation of the so-called transition matrix (T-matrix) of a single scatterer. Using a modal expansion of the scattered field with QNMs allows us to bring both analyticity and physical understanding into the calculation.

Finally, we apply the modal expansion of the T-matrix to practical cases of interest in nanophotonics. From the sole knowledge of a few modes of a single plasmonic nanorod, we calculate analytically multiple light scattering by a dimer and a Yagi-Uda antenna composed of these nanorods.

Université Paris-Saclay
Espace Technologique / Immeuble Discovery
Route de l'Orme aux Merisiers RD 128 / 91190 Saint-Aubin, France